MULTI-OBJECTIVE DESIGN OF SMALL TELESCOPES AND THEIR APPLICATION TO SPACE OBJECT CHARACTERIZATION

A Thesis
Presented to
The Academic Faculty

by

Ryan Daniel Coder

In Partial Fulfillment
of the Requirements for the Degree
Doctor of Philosophy in the
Guggenheim School of Aerospace Engineering

Georgia Institute of Technology
August 2016

MULTI-OBJECTIVE DESIGN OF SMALL TELESCOPES AND THEIR APPLICATION TO SPACE OBJECT CHARACTERIZATION

Approved by:

Dr. Marcus J. Holzinger, Advisor
Guggenheim School of Aerospace Engineering
Georgia Institute of Technology

Dr. Robert D. Braun
Guggenheim School of Aerospace Engineering
Georgia Institute of Technology

Dr. Brian C. Gunter
Guggenheim School of Aerospace Engineering
Georgia Institute of Technology

Dr. Moriba K. Jah
College of Engineering
University of Arizona

Dr. David M. Palmer
Space and Remote Sensing Sciences
Los Alamos National Laboratory

Dr. Chris A. Sabol
Directed Energy Directorate
Air Force Research Laboratory

Date Approved: April 26, 2016

ACKNOWLEDGEMENTS

This work was partially supported thanks to the Los Alamos Space Weather Summer School, funded by the Institute of Geophysics, Planetary Physics, and Signatures at Los Alamos National Laboratory (LANL). Additional funding continued while an Air Force Research Laboratory (AFRL) Directed Energy Scholar at the AFRL Air Force Maui Optical and Supercomputing (AMOS) site. The work was completed thanks to the support of the AFRL AMOS site and Integrity Applications Inc. - Pacific Defense Solutions (IAI-PDS) under contract FA6451-13-C-0281. IAI-PDS also provided all experimental data included in this work.

TABLE OF CONTENTS

LIST OF TABLES

LIST OF FIGURES

SUMMARY

Recognizing the increasingly congested and contested nature of space, this thesis contends that the fusion of small aperture, autonomous telescopes with Bayesian inference techniques can provide timely, actionable evidence of specific threats and hazards to space based assets. This evidence is required for a robust, persistent Space Domain Awareness capability that decision makers can employ to protect space services and capabilities. A multi-objective design framework for optical systems is defined empowering designers to identify families of designs which represent feasible solutions to user specific Space Domain Awareness mission requirements. Several trade studies are presented, the outputs of which directly inform the construction of the Georgia Tech Space Object Research Telescope. Novel techniques which ingest the unresolved imagery provided by small telescopes are developed, affording the estimation of attitude and angular velocity states of maneuvering space objects without prior knowledge of initial attitude, while maintaining computational tractability. Statistical inference techniques are applied to these posterior state distributions to rank the hypothesized subjects most likely under surveillance by the maneuvering space object in terms of their stochastic dominance. The totality of these contributions is validated on experimentally collected measurements of the Hubble Space Telescope.

CHAPTER I

INTRODUCTION

1.1 Motivation for Space Domain Awareness

The October 1957 launch of the Russian Sputnik I satellite set in motion the "space race," spurring a rush of innovative technologies which forever transformed our daily lives. The cell phones in our pockets and the nightly TV news are enabled by a fleet of satellites in geostationary orbit (GEO) approximately 36,000 km above Earth. Meanwhile, weather satellites in low earth orbit (LEO) warn of impending natural disasters and influence the harvest of the world's crops. The far reaching impact of these space assets has resulted in the space economy reaching its highest valuation ever, $314 Billion, in 2014 [1].

Despite the value and global importance of these space-based assets, current operational practices have resulted in an unsustainable use of space, with each launch adding new orbital debris around Earth's orbit. It is estimated that of all the objects currently in orbit around Earth, only 5% are active satellites [2]. This problem is exacerbated by events such as the often cited Chinese anti-satellite test in 2007 [3]. The first loss of a space based asset due to debris collision occured in 2009 when an Iridium and Cosmos satellite struck on orbit [4]. Both the ASAT test and Iridium/Cosmos collision increased the low-earth orbit (LEO) space object (SO) population by more than 60% [5]. More recent events include uncertainty of an alleged conjunction between the Russian Ball Lens In The Space satellite and debris from the Chinese anti-satellite test [6] and the explosion of a retired military weather satellite which produced more than 43 pieces of space debris [7].

In addition to economic concerns, space debris also poses a risk to human space flight safety and science missions. Three primary countermeasures have been used to date to ensure the safety of astronauts in orbit: passive shielding of spacecraft, collision avoidance, and prevention of new debris through spacecraft design and operational practices [8]. The ISS is protected by hundreds of custom made shields which protect important subsystems

from small articles of debris [9]. Larger debris objects require that active missions actively maneuver away from oncoming debris. In 2009, five different NASA robotic spacecraft, the Space Shuttle, and the ISS conducted collision avoidance maneuvers [8]. In 2014, the number of collision avoidance maneuvers undertaken by the ISS increased from 2 to 5 [10].

Finally, the exploitation and utilization of space remains a key component of the national security of the United States. One of the highest profile examples are the Global Position System (GPS) signals which are used for navigation of troops and guidance of munitions. The military has long relied on satellite communication to coordinate decision making, a function which only increases in importance as more unmanned aerial vehicles are acquired and deployed [11]. The military importance of such capabilities has led to a great deal of posturing among space faring nations. A Russian satellite maneuvered within 10km of 2 commercially operated Intelsat satellites, causing a great deal of concern among both government officials and commercial operators [12].

Recognizing all of these concerns, the response by US policy makers was made clear when, in 2001, the Rumsfeld Commission Report identified improvements in Space Domain Awareness (SDA) as a top priority to protect the US and its allies as well as maintain its economic and diplomatic objectives [13]. Joint Publication 3-14, "Space Operations," defines the high level activities of SDA as the detection, tracking, characterization, and analysis of space objects (SOs) [14]. The purpose of these SDA activities is to provide timely, actionable evidence of specific space threats and hazards to decision-making processes that protect space-based assets. Space objects are typically defined as active and inactive satellites, rocket bodies, and orbital debris [15]. The United States Strategic Command Joint Space Operations Center (JSpOC) operates the Space Surveillance Network (SSN) and currently tracks in excess of 21,000 objects with diameters greater than 10 cm [10]. Fig. 1 illustrates the 29 different sensors that constitute the current SSN. A key element of JSpOC responsibility is determining whether the orbits of SOs might bring them into close proximity, an event known as a "conjunction," and the conditional probability of SO collision. Other entities also provide data to the SSN, such as foreign governments

or other government agencies, such as the Missile Defense Agency [16]. Other SDA stakeholders include NASA Johnson Space Center's Orbital Debris Program Office, which has primary responsibility for characterizing members the orbital debris population below the SSN detection limit [17].

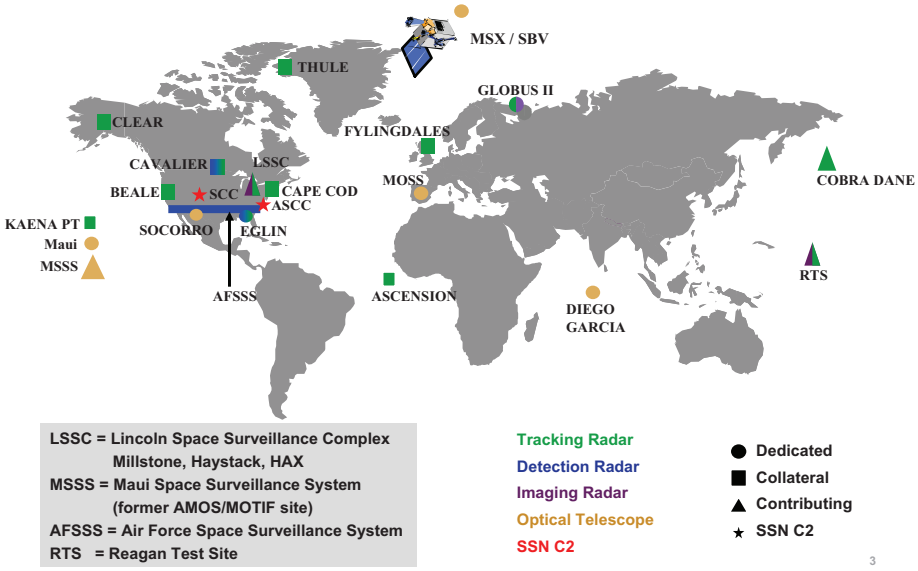

Figure 1: 29 Current SSN Sensors

1.2 Challenges to Space Domain Awareness

In order to establish a robust SDA capability, obtaining regular measurements is key [18]. Unfortunately, the Space Surveillance Network has historically been unable to collect enough raw measurements to fully characterize the SO population [19]. While many efforts are currently under way to augment the current SSN with additional sensors [17, 20], the price tag of acquiring new SSN assets makes existing SSN assets prime targets for deactivation in today's austere budgetary environment. One example of such a closure was the VHF Radar "Space Fence," occurring in 2013 to make way for a new radar system [21]. In response to this asset crisis, many have sought more affordable solutions SDA assets.

Even with few optical and radar assets available, scheduling limited sensor resources to collect observations of the large SO population is a complex scheduling and resource allocation problem. A great number of additional sensors with improved capability will increase

the complexity of this scheduling and planning problem. When budgeted future assets becomes operational, the number of tracked objects is expected to exceed 100,000 [16]. In addition, modifying established schedules under dynamically evolving scenarios, inclement weather conditions, and hardware faults is difficult [19]. The planning and scheduling is complicated by the fact that the current global network of SSN sensors is not exclusively controlled by the Air Force Space Command (AFSPC), but also by other entities that provide data to the command, such as foreign governments or other government agencies (OGA) such as the Missile Defense Agency [16].

Not only has the number of SOs tracked by the SSN greatly increased, but the data products and services provided by JSpOC have a record number of customers as well. Currently more than 100 countries as well as commercial satellite operators regularly request conjunctions assessments and launch screenings [16]. This has greatly increased the workload of JSpOC, as human analysts are needed to catalog orbital debris, recover lost satellites from uncorrelated tracks, and ensure computer calculated answers are intuitively correct [22]. Compounding this problem, the Air Force has faced several challenges concerning staffing a sufficient number of qualified analysts [16, 22].

Outside of these current operational challenges, there is also room for improved utility of the sensors themselves. As previously discussed, as sensor assets with greater capabilities are brought online, a greater number of SOs will be able to be added to the current SSN catalog. Thus, it will become increasingly likely that in the process of completing an assigned observation, a sensor asset will detect additional SOs previously unknown, such as orbital debris, in the vicinity of space around the initial target. Due to the centralized planning yet distributed nature of current SSN sensors [23] and the fast time scales involved in making SO observations, [24, 25] decisions concerning follow up observations are best made locally at the sensor location, and globally on time scales that are incompatible with human in-the-loop decision making.

The large number of SOs, complex scheduling constraints, high human workloads, and short time scales are persistent challenges that are well suited to using autonomy approaches [26]. The term ‘autonomy’ is often used to describe any system that can operate without

human intervention [27]. Autonomy can be described using the three levels of Intelligent Machine Design defined by NASA's Goddard Space Flight Center (GSFC) for use in spacecraft [27]. These three levels, Reaction, Routine, and Reflection, are defined by increasing levels of autonomy. The most basic of the three, the Reaction level, is primarily responsible for processing sensor information and commanding actuators over very short time scales. The Routine level is where routine evaluation and planning behaviors occur over medium time scales. Finally, the Reflective level is where high level planning, review, and learning occur over large time scales.

1.3 Avenues to Improved Space Domain Awareness

Of the many efforts to satiate the demand for automated, affordable SDA assets, one exceptional example is the Raven program. The Raven program began as an R&D effort at the AFRL Directed Energy Directorate's Air Force Maui Optical and Supercomputing (AMOS) site in 1995. Physically, a Raven system is a combination of several components: the telescope and dome, electro-optical (EO) sensor, computer, weather station, and a GPS receiver and timing system. However, a Raven-class telescope system is not rigidly defined by a specific combination of hardware. Rather, it is a design paradigm where commercial off-the-shelf (COTS) hardware and software are combined to fulfill designated mission requirements. The Raven system at AMOS is capable of acting at the "Routine" level of autonomy. Using the weather station sensors, it can detect nautical twilight to begin automated boot sequences and detect inclement weather to suspend operation. More impressively, given a set of tasks, it can determine an appropriate observation schedule to satisfy the human-provided objectives. In 2001, a Raven located at the Maui Space Surveillance Site (MSSS) became a contributing sensor to the SSN [19].

While the low cost of COTS hardware and automation of the Raven-class telescope make it an appealing SDA solution, it is not enough to deploy myriad sensors; these assets must be supported by algorithms which can glean actionable information from observations. In 2011, Air Force Space Command (AFSPC) asked the National Research Council to make recommendations specifically concerning how best to develop and incorporate better

algorithms into current JSpOC data pipelines [16]. Successful SDA requires many tasks to successfully identify and predict threats and hazard to space-based assets including, but not limited to: data tasking, collection, characterization, and exploitation. This thesis is concerned with algorithms for characterizing SO. Characterizing space objects entails identifying information about the physical and functional features of a SO including, but not limited to, those listed in Table 1 [28].

Table 1: SO Characteristics

Characteristic	**Example Methodologies**
Size Shape Material Composition Attitude	RADAR Unresolved Imagery Resolved Imagery
Operational Status Payload Capabilty Mission Purpose	Inference Subject Matter Expertise

It is common to group the size, shape, and material composition of the SO together and refer to them collectively as the SO "shape model" [28]. Alongside each characteristic is a methodology by which information about this characteristic could be gained. The characteristics in Table 1 have been grouped by methodologies purposefully. The attitude and shape model can be estimated directly from observations. However, knowledge about SO operational status, payload capability, or mission purpose must be inferred or otherwise derived from subject matter expertise.

For SO in low earth orbit, shape model and attitude estimation is performed extensively using radar-based methods. The first radars utilized for SDA were those belonging to the U.S. Navy's "Space Surveillance System," coming online in 1959 [29]. Unfortunately, Rayleigh scattering makes debris smaller than 10 cm in diameter very difficult to reliably track [30]. The shape and attitude of large SO can also be estimated from resolved imagery taken by ground based optical sensors. However, when SO are too distant to be imaged by radar facilities or too small to be adequately resolved by ground based optical sensors, the only data currently available is unresolved imagery [28].

Unfortunately, SO that are distant and small comprise increasingly important classes

of SO. The worlds communication satellites are most frequently located in GEO stationary orbit, too far away for ground-based resolved imagery. Additionally, on-orbit collisions produce large clouds of small debris. Current estimates place the number of objects larger than 1 cm at approximately 700,000 and the number of objects larger than 1 mm at approximately 200 million [31]. Additionally, the low cost, scalability, and potential for disaggregated constellation design, has led to the rapid proliferation of physically small "cube-sats" in LEO. These facts imply that the successful exploitation of unresolved imagery produced by Raven-class telescopes is essential to a persistent, robust SDA capability. Consequently, the contributions of this thesis conform to and support a single guiding philosophy.

Thesis Statement: The fusion of small aperture, autonomous telescopes with Bayesian inference techniques can provide the timely, actionable evidence of specific threats and hazards required for a persistent Space Domain Awareness capability that decision makers can employ to protect space services and capabilities.

CHAPTER II

SURVEY OF SMALL TELESCOPES AND SPACE OBJECT CHARACTERIZATION

This chapter outlines previous efforts to design small aperture telescopes and techniques for characterizing SO. This is done in recognition that the contributions presented here would not be possible without these previous breakthroughs and to provide context for the contributions of this thesis. §2.1 outlines several small aperture telescopes built which achieve a diverse set of scientific, educational, and defense related missions. §2.2.1 gives a brief history of various approaches to light curve inversion while §2.2.2 details the various approaches to SO characterization, specifically operational mode classification.

2.1 Raven-class Telescopes

The success of the Raven program has led many institutions to embrace small aperture telescopes as affordable, effective research and development test beds. In 2006, Japan Aerospace Exploration Agency (JAXA) placed 0.35m telescopes in its Mt. Nyukasa optical observational facility. The main objective of the facility is to develop detection technology for space debris less than 10 cm in size. It also aims to conduct GEO surveys as well as study light curves of GEO objects [32].

Around the same time, a joint team of researchers guided by the Center for Space Debris Information, Collection, Processing, and Analysis of the Russian Academy of Sciences collaborated with 15 observatories to construct and operate the International Scientific Optical Network (ISON). A series of dedicated 0.22 m telescopes was combined with charge-coupled device (CCD) cameras, Global Positioning System (GPS) receivers, and the requisite software to make more than 130,000 observations of GEO objects. This effort enabled the Keldysh Institute of Applied Mathematics (KIAM) to find 288 GEO objects that were absent from the public orbital databases [33].

The United States Air Force Academy has partnered with several institutions to build a

global network of small-aperture telescopes, named the Falcon Telescope Network (FTN). These 0.5m telescopes support several missions including satellite imaging, astronomical research, and STEM support. Operating at the Routine level of autonomy, the FTN is capable of executing nightly observation campaigns aggregating by network partners [34, 35].

Another example includes Los Alamos' Telescope ALert Operations Network (TALON), developed for detecting and observing gamma ray burst (GRB) events. The TALON network was comprised physically of RAPid Telescopes for Optical Response (RAPTOR) telescopes: arrays of COTS optics, including four 0.4m telescopes or sixteen 0.2m cameras. Operating at the Routine level of autonomy, each RAPTOR had a "client" agent which was responsible for transmitting data to a centralized server. This centralized server synthesized these individual data logs to produce follow-up observation alerts which were pushed back to all telescopes connected to the TALON [36].

Recently, detailed thought has been applied to moving telescope network autonomy to the Reflective level. The Thinking Telescope program at Los Alamos National Laboratories has taken lessons learned from TALON and has combined additional RAPTOR telescopes with unsupervised learning techniques. The architecture consists of a vast database of observational variations from persistent sources coupled with intelligent agents. These agents learn over time to distinguish between actual gamma ray burst (GRB) events and environment noise such as airplane lights and other non-celestial phenomena [37].

Academic and government institutions are not alone in embracing Raven-class telescopes. In 2006, Lockheed Martin began passively tracking LEO space objects using 0.36m telescopes. As a result of those successful efforts, Lockheed invested in what is now known as the Space Object Tracking (SPOT) Facility. Achieving first light in 2012, the SPOT facility is comprised of three 1m telescopes whose primary mission is to observe satellites and orbital debris [38].

Despite these successful implementations of Raven-class telescopes, key questions concerning their widespread adoption for SDA. A larger scale deployment necessarily implies that each will be operating in optically diverse environments. Therefore, it is important to determine which combination of COTS components yield the best performance given the

mission and local optical environment. Tacit in this statement is the reality that different SDA missions are best performed with fundamentally different hardware configurations. How does one balance these conflicting mission requirements to yield a successful SDA asset?

2.1.1 Multi-Objective Design

To best accomplish this mission, one desires a conceptual design framework that allows for the incorporation of multiple design objectives. However, the current literature reveals no conceptual design studies of optical systems that utilize COTS components to complete SDA missions. Some studies investigate the performance of a specific, custom optical designs [39, 40]. Other studies list the performance metrics of finalized optical systems individually, making it difficult for the decision maker to understand the impact of performance tradeoffs or why a particular design is selected. Additionally, those interested in constructing a Raven system might come from backgrounds other than optical design or physics. Thus, the tacit radiometric models and assumptions utilized in the literature to derive performance estimates of optical systems may not be readily apparent [41, 42]. Still, other studies that do detail a radiometric model utilize assumptions that are not applicable to the desired optical environment or mission [25]. These findings motivate the systems engineering trade study performed for this thesis.

Realizing that the background knowledge necessary to conduct such a study is currently scattered among the fields of astronomy, information theory, optics, statistics, and systems design, Chapter 3 outlines the collection of multi-disciplinary equations necessary to create a radiometric model of optical systems utilizing a consistent nomenclature. Further, the design metrics and approach outlined in Chapter 4 are intended to provide a high level methodology for quantifying performance tradeoffs among design parameters which are typically controllable when selecting COTS components. It is emphasized that the approach presented is not intended to replace traditional, detailed optical design. Rather, it is hoped that the contributions in this work are used during the conceptual design phase to help designers narrow the design space and to identify families of designs which represent feasible

solutions to user specific mission requirements.

2.1.2 Raven at Georgia Tech

Deploying numerous SDA assets is only one component of successful SDA. These assets must be used in tandem with algorithms which can successfully extract information from collected observations. Critically, any new algorithms offered by the research community must be able to perform successfully in an operational setting. Unfortunately, due to the defense related nature of SDA, there is a lack of experimental data available to the research community. This lack of operational data products, and the affordable nature of the Raven design paradigm, has led an increasing number of institutions to embrace Raven-class telescopes as cost effective research testbeds. Ravens around the world are used for the development of SO detection and characterization algorithms, and to investigate novel autonomy architectures [34, 32, 43].

Thus, an additional contribution of this thesis is to use the multi-objective design framework to select COTS components for the construction of a Raven-class telescope at Georgia Tech. The design, assembly, and calibration efforts of the author resulted in the Georgia Tech Space Object Research Telescope (GT-SORT). A summary of this effort is outlined in Appendix B. Georgia Tech, like the aforementioned organizations, have selected to construct this facility not only to provide a source of experimental data, but also to better inform their own research directions.

2.2 Space Object Characterization

Given sufficient observational data, SDA stakeholders must successfully exploit this data for information related to the physical and functional characteristics of SOs. Because unresolved imagery is the only avenue to obtain this information on several important classes of SO, such as GEO objects and cube-sats, Chapter 5 outlines several novel contributions that allow the attitude of an agile SO to be estimated from unresolved imagery using light curve inversion. Chapter 6 presents several statistical methods for inferring the active control mode of an agile SO using the posterior distributions of attitude and body angular rate states.

2.2.1 Space Object Attitude Estimation

A light curve is a temporally resolved sequence of power measured over a specified bandwidth. Each point in the light curve is the total amount of power reflected by the SO measured from an unresolved image. Because the total amount of power reflected by the SO is dependent on the SO shape and attitude, estimating either the attitude or shape of the SO is possible using the observed light curve under certain assumptions [44]. This process is referred to as light curve inversion, and was initially developed to characterize asteroids [45].

Past efforts to characterize asteroids have used batch estimation methods, where attitude, angular rates, moments of inertia and shape model are all simultaneously estimated. Batch estimation requires that available light curves represent the asteroid in a variety of solar phase angles and attitudes relative to the observer, often assuming a fixed spin axis [46, 47, 48, 49].

While the light curve inversion process is similar, there are several important differences between asteroids and man-made SOs. The first significant difference is that unlike asteroids, many SO have highly angular surfaces composed of several materials, each having different time-varying reflectance properties. This has led some researchers to separate the SO attitude from materials and shape properties, which are collectively referred to as the SO "shape model" [28]. Another difference is that satellites are typically actively controlled. Asteroids, like orbital debris, are generally not actively controlled and subject to many perturbative forces such as atmospheric drag, solar radiation pressure, and earth oblateness effects [50]. SOs that can actively maneuver, typically referred to as "agile" SOs, introduce new modeling complications. The author defines an agile SO as one that is maneuvering to produce rotational motion about its center of mass, not one that is maneuvering to change its orbit plane. Nonzero torques, introduced by SO actuators, are difficult to discern from the normalized mass properties of the SO [51].

The first work outlining the theoretical application of light curve inversion to SO characterization was given by Hall et al. in 2005 [44]. Sequential filtering techniques were first applied to simulated, non-maneuvering SOs in 2007. The approach uses Unscented Kalman

Filters (UKFs) to estimate either the SO attitude, shape model, or both simultaneously[52]. More sophisticated methods for estimating the SO shape model have been proposed using Multiple Model Adaptive Estimation (MMAE) techniques. A bank of UKFs, each with a different shape model, is implemented to estimate the position, attitude, attitude rates of a simulated non-maneuvering SO [53]. Recognizing that UKFs are inappropriate for substantially non-gaussian distributions, which can be caused by bidirectional reflectivity distribution function (BRDF) measurement models that are non-linear functions of attitude states, recent efforts utilize particle filters (PFs) to estimate the attitude states of agile SO. It is also shown how shape model bias can be included in the estimated states. To account for the unknown SO torques and inertia properties, SO angular rates are modeled as a white noise process [51].

Realizing that including bias states increases the state dimensionality, this thesis introduces an adaptation of the Singer dynamics model to represent the motion of agile SO. This enables the now linear body angular velocity states to be analytically marginalized out to reduce the computational burden of a traditional particle filter. This concept, often referred to as Rao-Blackwellization, enables the estimation of attitude and angular velocity states of maneuvering space objects without a priori knowledge of initial attitude while maintaining computational tractability. The simulated results of the Rao-Blackwellized Particle Filter (RBPF), presented in Chapter 5, show for the first time the full three degree of freedom estimation of an agile SO.

2.2.2 Space Object Operational Mode Classification

Determining the current attitude of SO is a critical aspect of characterization, and is increasingly useful the closer to real time the information is generated. However, attitude is not an immediately actionable piece of information; characteristics such as SO operational status, payload capability, and mission purpose can be more useful in decision making processes. To help inform the body of evidence for these important classes of SO, the contributions of this work focus on inferring an SO's current, active control mode using light curve inversion. This work defines the active control mode as "the classification of a time history of attitude

and angular rate states necessary for an SO to rate track a specific subject." While this encompasses traditional "operational modes" such as "sun-pointing," it also describes more specific behavior such as "rate tracking SO catalog number 16111," for example.

The earliest work in the public literature on SO operational mode classification, completed by MIT Lincoln Laboratory, utilizes light curves gathered using the Space-Based Visible sensor to classify geostationary orbit (GEO) SO in the following categories: nominal in-slot, anomalous in-slot, nominal moving, anomalous moving, drifting, and graveyard. These classifications were made using Bayesian networks, but little detail is provided due to the operational nature of the work [54].

Another approach outlined in the literature also utilizes Bayesian networks, where the possible classifications are: nominal and anomalous. This work focused on constellations of SO in the same GEO slot, utilizing the classifications to help ameliorate the problem of "cross-tagging." Cross-tagging occurs when a SO is erroneously identified as another, an occurrence much more likely to happen among a cluster of SO in GEO sharing the same slot [55]. This work has been extended to multi-satellite scenarios where hypothesis testing and sliding window techniques, among others, are proposed to classify SO using only nightly comparisons of light curves [56].

Despite the modicum of prior work on SO operational mode classification, many similar concepts have been developed in the fault detection and classification literature. Many of those techniques have already been applied to different SDA specific problems. Surveying the literature for fault detection as applied to adaptive control, fault control, and systems identification reveals that all change detection algorithms fall into one of three general categories [57].

The first category applies statistical tests to the residuals generated by a Kalman filter. Tests for whiteness, zero mean, and a specified variance all indicate that the system model is representative of the true, physical system. If the residuals fail these tests, and the model accurately reflects the true system, this indicates that the behavior of the physical system have changed [58]. The second category implements two filters in parallel, where statistical tests are applied to the distributions at two discrete time steps. Also referred to as "sliding

window" techniques, these tests are applied to certain parameters including: the generalized likelihood ratio (GLR), the divergence test, or changes in spectral distance [59]. The third and final category is the multiple model method, where all hypothesized change times are defined and compared to the filtered estimates. Similarly to "match filtering" techniques, the hypothesis which provides the smallest residuals is taken to be the correct hypothesis [60].

Perhaps the earliest application of a multiple hypothesis methodologies in the SDA field is the multiple-model adaptive estimation technique proposed to determine the most likely shape model of an SO. The core technique, where a bank of filters each operating under a different hypothesis to determine the most likely physical system, is similar to those ideas proposed in the fault detection literature. Indeed, the most likely physical shape is indicated by the hypothesis which produces the highest likelihood [53].

In a manner similar to multiple model methods, match filtering techniques have also been applied to SDA. First applied to increasing the signal-to-noise ratio (SNR) of radar returns, the core concept of a match filter is that multiple signal "templates" are hypothesized where the correct hypothesis yields the greatest SNR [61]. One corresponding SDA application utilizes multiple hypothesized templates to detect unresolved SO in low SNR imagery obtained with optical telescopes [62]. This is particularly useful when numerical propagation errors or sensor pointing uncertainties cause differences between SO orbit and telescope pointing.

The concept of "active control modes" is motivated by the following scenario: an agile SO under surveillance by an SDA stakeholder, termed the "target" SO, is hypothesized to be actively rate-tracking another SO, called "subject" SO, with its optical payload. This work emphasizes that an agile SO is one that is maneuvering to produce rotational motion about its center of mass, not one that is maneuvering to change its orbit plane. The overall goal of the methodologies presented is to identify, from a mutually exclusive but not exhaustive list of hypotheses, which subject is under observation by the agile SO. The methodologies utilize both estimated attitude states and estimated body angular velocities, such that any sensor that provides these estimates could exploit the contributions enumerated in

this work. However, the simulated results assume that a terrestrial telescope produces unresolved images of the target SO. To the authors knowledge, estimating both the attitude and velocity states of an agile target SO using unresolved imagery requires innovations in light curve inversion presented in Chapter 5.

In solving this scenario, the author embraces the philosophy of inductive reasoning and make the "open-world assumption" for representing knowledge [63]. Applied to SDA, the knowledge of stakeholders will always contain uncertainty, and new information should always be used to inductively update beliefs by eliminating incorrect hypotheses. Consistent with this philosophy, all sets of hypotheses presented in this thesis represent a mutually exclusive and open set of hypotheses. This stands in contrast to previous work that relies on framing problems with a closed set of hypotheses. This "closed-world assumption" artificially create information by comparing measured evidence to synthetic measurements based upon known assumptions, thereby forcing the new information to support a limited list of hypotheses that is not guaranteed to contain the truth.

The specific metrics presented in Chapter 6 include a measurement dissimilarity metric, which computes the time integral of the error between the estimated target space object bore-sight and the line-of-sight vector to each hypothesized target. To discriminate between two closely co-located targets, i.e. those with nearly parallel line-of-sight (LOS) vectors, a "pointing quality" metric is presented utilizing the estimates of body angular velocity. This metric computes the Mahalanobis distance using the error between the mean vector of the posterior body angular velocity distribution and each hypothesized body angular velocity triple. Since some knowledge of SO shape model is required for light curve inversion techniques, SO shape model information can be fused with the principles of radiometry to determine maximum body angular velocity errors that satisfy signal-to-noise ratio detection requirements. Finally, the estimated body angular velocities are utilized to compute mass specific rotational angular momentum and mass specific rotational kinetic energy analogs. These analogs are utilized in a statistical hypothesis testing framework to systematically eliminate those hypotheses which are not consistent with observational data.

2.3 Summary and Organization

The organization of this dissertation and highlights from each chapter are summarized here. Contributions from Chapter 3 and Chapter 4 are combined to define a conceptual design methodology for affordable SDA assets. The results of this study led to the selection of COTS components that constitute the GT-SORT, as outlined in Chapter B. Novel contributions in agile SO attitude estimation are presented in Chapter 5. Chapter 6 proposes new methods for estimation SO active control mode. Table 2 outlines how these contributions are supported by existing literature, denoted as checkmarks.

Table 2: Summary of Related Research

Reference	Telescope Design	SO Characterization	
		Attitude	Active Control Mode
Sabol [19]	✓		
Fabricant [39]	✓		
Ackermann [40]	✓		
Brown [64]	✓		
Ackermann [41]	✓		
Rios [42]	✓		
Shell [25]	✓		
Dunlap [45]		✓	
Magnusson [46]		✓	
Cellino [65]		✓	
Kaasalainen [47]		✓	
Torppa [49]		✓	
Kaasalainen [66]		✓	
Torppa [67]		✓	
Hall [68]		✓	
Hall [69]		✓	
Jah [70]		✓	
Wetterer [52]		✓	
Linares [53]		✓	
Holzinger [51]		✓	
Abbot [54]			✓
Chaudhary [55]			✓
Coder [71]	✓		
Coder [72]		✓	
Coder [73]			✓
Introduced Contributions	Chapter 2.1 Chapters 3 & 4	Chapter 2.2.1 Chapter 5	Chapter 2.2.2 Chapter 6 & 7

2.4 Contributions of Thesis

This thesis advances the state of the art in several areas of space domain awareness. The first area is the multi-objective design of electro-optical assets, specifically concerning small-aperture telescopes. Three analytic performance metrics rigorously define the performance of these assets, enabling the identification and ranking of major system performance drivers. It is shown how these metrics can be used to construct Pareto frontiers of non-dominated designs. From this set, stakeholders may select point designs which satisfy mission requirements in a variety of disparate operating environments.

The second set of contributions show how the unresolved imagery produced by small-aperture telescopes can be exploited; the sum of which constitute a new approach to the light curve inversion problem. A physics-based measurement model, exponentially correlated dynamics model, and the Rao-Blackwellized Particle Filter enable the estimation of attitude and angular velocity states of maneuvering space objects without a priori knowledge of initial attitude, while maintaining computational tractability. These methods assume that knowledge of the SO shape and material properties, referred to as the "shape model," is known.

The final set of contributions represent a set of mathematical techniques which transform the state estimates provided by the RBPF into a list of subjects most likely under observation by a SO - key component of SDA. This is accomplished by pruning hypotheses from a mutually exclusive but not exhaustive list of hypothesized subjects either in terms of their stochastic dominance relative to each other or in terms of rejecting hypotheses with multi-variate hypothesis testing. Critically, this activity is only possible because of the extra information, specifically the body angular velocity estimates, provided by the novel approach to the light curve inversion problem. While each chapter outlines a simulated test demonstrating the utility of these techniques, the totality of these contributions is tested on experimentally collected data of the Hubble Space Telescope.

2.5 List of Publications

The publications which constitute the basis of this thesis are listed below, with the most recent publications listed first.

Peer Reviewed Journal Articles

- Coder, R.D, Holzinger, M.J., and Jah, M.K.; "Inferring Space Object Active Control Mode using Light Curve Inversion," Journal of Guidance Dynamics and Controls (Submitted April 2016).

- Coder, R.D., Linares, R., and Holzinger, M.J.; "3DOF Estimation of Agile Space Objects using Marginalized Particle Filters," Journal of Guidance Dynamics and Controls (Submitted December 2015).

- Coder, R.D. and Holzinger, M.J.; "Multi-Objective Design of Optical Systems for Space Situational Awareness," Acta Astronautica (Accepted August 2015).

Peer Reviewed Technical Notes

- Coder, R.D., Wetterer, C.J., Hamada, C.M., and Holzinger, M.J.; "Inferring Active Control Mode of the Hubble Space Telescope using a Rao-Blackwellized Particle Filter," AIAA Journal of Guidance, Control, and Dynamics Technical Notes, (Submitted April 2016).

- Coder, R. D., Matthew, M. V., Jaunzemis, A. D., Worthy, J. L., and Holzinger, M. J.; "Georgia Tech Space Object Research Telescope (GT-SORT)," AIAA Journal of Guidance, Control, and Dynamics Technical Notes, (Submitted April 2016).

Invited Talks

- Coder, R.D, Holzinger, M.J., and Jah, M.K.; "Classifying Space Object Active Control Mode with Probabilistic Reasoning," Non-Resolvable SOI Working Group, Kihei, HI, April 2016.

Conference Presentations

- Coder, R.D, Holzinger, M.J., and Jah, M.K.; "Classifying Space Object Active Control Mode with Probabilistic Reasoning," Advanced Maui Optical and Space Surveillance Technologies Conference, Wailea, HI, (Submitted April 2016).

- Coder, R.D., Linares, R., and Holzinger, M.J.; "Improved Models for Attitude Estimation of Agile Space Objects," AAS-15-231, 25th AAS/AIAA Spaceflight Mechanics Meeting, Williamsburg, VA, January 2015.

- Coder, R.D. and Holzinger, M.J.; "Sizing of a Raven-class Telescope Using Performance Sensitivities," 2013 Advanced Maui Optical and Space Surveillance Technologies Conference, Wailea, HI, September 2013.

- Coder, R.D. and Holzinger, M.J.; "Autonomy Architecture for a Raven-Class Telescope with Space Situational Awareness Applications," AAS-13-359, 23rd AAS/AIAA Spaceflight Mechanics Meeting, Kauai, HI, February 2013.

CHAPTER III

RADIOMETRIC PRINCIPLES AND PHENOMENOLOGY

To complete an optical telescope design space exploration, it is necessary to first establish a complete source to sensor photometry model [74]. Of particular interest to the designer of SSA systems is the rate of photons emitted by the SO and the background sky. Together, these two quantities are the greatest contributors to the "signal-to-noise" ratio (SNR), which is frequently used to define the quality of an image captured with a digital sensor. This thesis uses the signal to noise ratio as the foundation for the limiting magnitude performance metric and also as the basis for the probability of un-cued SO detection in Chapter 4.

The radiometric model developed here is also used to define a physics based measurement model for the light curve inversion problem. By accurately accounting for the disturbance of the atmosphere in the forward modeling of satellite brightness, the simulations implemented for testing light curve inversion filters are more realistic. Finally, it is shown in Chapter 6 how this same model can be used to bound the norm of the tracking error of satellite.

3.1 Radiometric Model

By convention, SO brightness is quantified using the apparent visual magnitude system, first developed by early astronomers. The system is unitless, logarithmic, and references the brightness of Vega as the scale's zero point. The resulting SO signature represented in the apparent visual magnitude system, $m_{v,\mathrm{SO}}$, is found using Eq. (1) [74].

$$m_{v,\mathrm{SO}} = m_{v,\mathrm{Sun}} - 2.5\log_{10}\left[\frac{1}{R^2}\int_{\lambda_{\mathrm{LL}}}^{\lambda_{\mathrm{UL}}} M_{\mathrm{Earth}}\left(\lambda\right) F_r\left(\theta_I^B, \hat{s}, \hat{R}, \lambda\right) \mathrm{d}\lambda\right] \tag{1}$$

Please note that unless otherwise stated, this radiometric model uses standard SI units. In this equation, R is the distance from the SO to the observer, $M_{\mathrm{Earth}}\left(\lambda\right)$ is the spectral exitance of the Sun at the Earth integrated over wavelength λ, and F_r is the reflectance function from the SO towards the observer, from direction $\hat{\mathbf{s}}$, the unit vector from the Sun to the SO. The rotation from the inertial frame to the body frame of the SO necessary

to calculate these unit vectors is denoted by θ_I^B. Eq. (1) generally represents the highest fidelity models of SO signatures, which are functions of a multitude of variables including SO geometry, attitude, and the bidirectional reflectance distribution function (BRDF) of the SO materials [75]. In order to simplify this study, first order approximations are made that maintain a form representative of the majority of potential SOs to be examined, as detailed in the results section. A general facet shape model can be employed to simplify the reflected intensity density function, [52] or, in the case of basic geometrical shapes, closed form solutions are available [41]. In this case, the apparent visual magnitude of a SO can be calculated as shown in Eq. (2)[76].

$$m_{v,\mathrm{SO}} = m_{v,\mathrm{Sun}} - 2.5\log_{10}\left[\frac{A\alpha\left[\rho_{\mathrm{spec}}(\psi)+\rho_{\mathrm{diff}}(\psi)\right]}{R^2}\right] \tag{2}$$

Here, the visible, illuminated area of the SO is A, the albedo of the SO materials are $\alpha \in [0,1]$, and ρ defines the specular and diffuse components of reflectivity as a function of the solar phase angle, ψ. The resulting visual magnitude of the SO is now found in the unit-less and logarithmic apparent visual magnitude system. Conversion from this scale into radiometric units is necessary to complete a performance based assessment. This formulation is appropriate for CCD, complementary metaloxidesemiconductor (CMOS) sensors, and photon counters [24]. The visual magnitude of an SO is equivalent to a photon flux density above the Earth's atmosphere, Φ_{SO}, as described by Eq. (3)[25].

$$\Phi_{\mathrm{SO}} = \Phi_0 \times 10^{-0.4 m_{v,\mathrm{SO}}} \tag{3}$$

In Eq. (3), Φ_0 is the photon flux density of a magnitude 0 object, and the units for both Φ are photons/s/m^2. In order to find Φ_0, the first calculation to be made is the total spectral exitance of the Sun, $M_{\mathrm{Sun}}(\lambda)$, measured in W/m^2/nm. To obtain an accurate approximation of the total spectral exitance, the Sun is idealized as a black body whose radiated power at the Sun's photosphere as a function of wavelength has the form given by Eq. (4) [74].

$$M_{\mathrm{Sun}}(\lambda) \simeq \frac{2\pi h c^2}{\lambda^5\left[\exp\left(\frac{hc}{k\lambda T}\right)-1\right]} \tag{4}$$

The constants h, c, and κ are Planck's constant, the speed of light, and Boltzman's constant respectively. The wavelength, λ, of interest is user defined. For example, Fig. 1 shows the

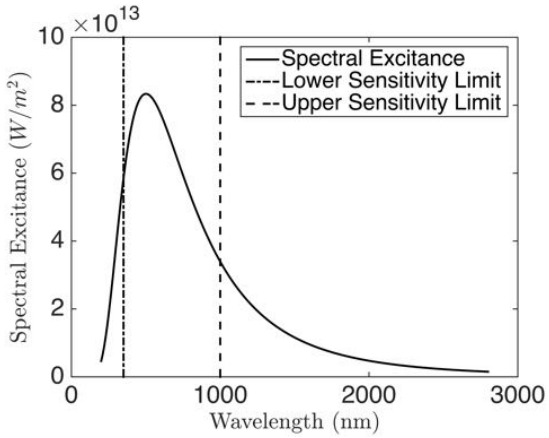

Figure 2: Black Body Approximation of Spectral Exitance of Sun

spectral exitance for light with a wavelength between 200 and 2800 nm. These photons then travel to the Earth such that the spectral exitance above the atmosphere, $M_{\text{Earth}}(\lambda)$, is given by Eq. (5), where 1 AU is the mean Earth-Sun distance [74].

$$M_{\text{Earth}}(\lambda) = \frac{r_{\text{Sun}}^2}{(1\ \text{AU})^2} M_{\text{Sun}}(\lambda) \tag{5}$$

The Sun's radius is denoted by r_{Sun}. Despite the Sun-SO distance varying from a mean value by its orbit size above Earth, the altitude of an SO is small compared to the mean Earth-Sun distance. Therefore, little accuracy is lost by using the value of 1 AU in Eq. (5). The spectral exitance can then be integrated over the sensitive wavelengths of the EO sensor to yield a total solar exitance emitted over the sensitivity spectrum of the EO sensor above the Earth's atmosphere. This solar exitance can then be used to find the exitance of a magnitude 0 object, M_0, using Eq. (6) [74].

$$M_0 = \left(\int_{\lambda_{\text{LL}}}^{\lambda_{\text{UL}}} M_{\text{Earth}}(\lambda)\ \ \mathrm{d}\lambda \right) 10^{-0.4 m_{\text{Sun}}} \tag{6}$$

It is important to recognize that filter selection impacts the wavelengths of light which pass onto the EO sensor. Using no filter, or a clear filter, a typical EO sensor is sensitive between 350 and 1000 nm. However, certain SSA missions will dictate the use of a filter which block all light outside a specific wavelength range, which will impact the overall sensitivity of the EO sensor. Eq. (7) is used to convert the magnitude 0 objects flux to a photon flux density, denoted Φ_0 [25].

$$\Phi_0 = \frac{M_0 \lambda}{hc} \tag{7}$$

In Eq. (7), a weighted average of $\lambda = 625$ nm is used, and the quantities h and c are Planck's constant and the speed of light respectively [74]. Having found the resulting SO photon flux density using Eq. (3), the next step is to model the light gathering capabilities of a proposed telescope system. For a ground-based sensing application, the photon flux captured by the optical system, q_{SO}, measured in e^-/s, is given by Eq. (8) [25].

$$q_{\text{SO}} = \Phi_{\text{SO}} \tau_{\text{atm}} \tau_{\text{opt}} \left(\frac{\pi D^2}{4} \right) \text{QE} \tag{8}$$

In Eq. (8), τ_{atm} and τ_{opt} are the transmittance of the atmosphere and optics assembly, which have possible values ranging from $\tau \in (0, 1]$. The aperture diameter of the telescope is given by D, and the quantum efficiency of the CCD is defined as $\text{QE} \in (0, 1]$. The atmospheric transmittance, optical transmittance, and quantum efficiency are included in Eq. (8) in lieu of more detailed modeling. If higher fidelity models of these values are desired, the convolution of any combination of these three values could be utilized. Additionally, this methodology can be extended for space-based optical systems by simply setting $\tau_{\text{atm}} = 1$.

Successful detection of an SO typically requires that the number of photons emitted by the SO be several times greater than the number of photons emitted by noise sources. One such noise source is the background radiant intensity, also referred to as the background sky brightness or light pollution. To accurately characterize this noise source, a sky sensor is utilized to measure the local background radiant intensity, I_{sky}, whose major sources are moonlight and local light pollution. Because I_{sky} is measured in units of m_v/arcsec^2, conversion to radiometric units is necessary. The total photon radiance at the telescope aperture due to background sky pollution, L_{sky}, in photons/s/m^2/sr, is given by Eq. (9) [25].

$$L_{\text{sky}} = \Phi_0 10^{-0.4 I_{\text{sky}}} \left(\frac{180}{\pi} \right)^2 3600^2 \tag{9}$$

The next step is to to calculate the total irradiance on the focal plane, E_{sky}. However, for clarity, a simple telescope diagram is presented in Fig. 3 to illustrate the major telescope variables. In Fig. 3, f denotes the effective focal length and D the aperture diameter of the telescope [77]. It is also common to refer to optics systems by their "f-number," N, as shown in Eq. (95) [78].

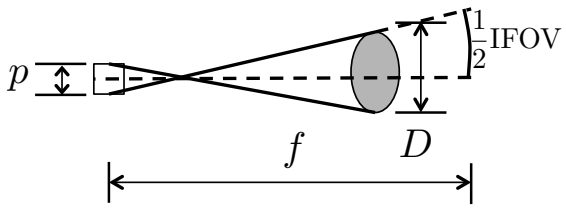

Figure 3: Common Telescope Parameters

$$N = \frac{f}{D} \tag{10}$$

In Eq. (95), f denotes the effective focal length and D the aperture diameter of the telescope. As a result, the f-number is also referred to as the focal ratio, focal number, or f-stop. Using these parameters, one can also define the instantaneous field of view (IFOV), sometimes referred to as the pixel field of view, of the optical system. The equation for IFOV is given by Eq. (11), where p is the length of the sensor pixel [78].

$$\text{IFOV} = 2\arctan\left(\frac{p}{2ND}\right) \tag{11}$$

Using Eq. (95), one can now calculate the total incidence on the focal plane from the radiance at the telescope aperture. The "camera equation" is used, as defined by Eq. (12) [74].

$$E_{\text{sky}} = \frac{L_{\text{sky}}}{g} \tag{12}$$

Here, g defines the capability of the system to convert radiance from the aperture to the sensor focal plane, and has been defined for a singlet lens, valid for all focal lengths, as shown in Eq. (13) [74].

$$g = \frac{1 + 4\,(ND)^2}{\tau_{\text{opt}}\pi} \tag{13}$$

It is very typical for SSA telescopes to utilize Cassegrainian-type optics. Thus, an additional term indicating the loss of photons due to the obstruction created by the secondary mirror and supporting structure, τ_s, is introduced [74].

$$\tau_{\text{opt,c}} = \tau_{\text{opt}}\tau_s \tag{14}$$

One way of estimating the transmission loss due to the secondary support structure is given by Eq. (15) [74].

$$\tau_s = 1 - \frac{D_s^2}{D^2} \tag{15}$$

Here, D_s is the diameter of the secondary mirror. It is difficult to precisely define the diameter of the secondary for every design point of interest. Using an existing .5 m design it is noted that the value of $\tau_s = 0.84$. Utilizing the previously defined relations, a final expression for the photon flux per pixel resulting from background radiant intensity, $q_{p,\text{sky}}$, is expressed in e^-/s/pixel as shown in Eq. (16).

$$q_{p,\text{sky}} = \frac{L_{\text{sky}} \tau_{\text{opt}} \tau_s \pi \left(\text{QE}\right) p^2}{1 + 4N^2} \tag{16}$$

In Eq. (16), the EO sensor is assumed to have square pixels. For non-square pixels, p^2 can be replaced by the appropriate unit of area. The radiometric model developed defines the photon flux of SOs, in Eq. (8), and the background sky brightness, in Eq. (16), as a function of various environmental variables and SSA asset design parameters. With these two quantities defined, it is now possible to discuss how these quantities relate to the ability of an SSA asset, such as a Raven-class telescope, to successfully detect and track SOs. The most commonly used measure to describe the quality of images captured by optical SSA assets is the signal-to-noise ratio.

3.2 Signal-to-Noise Ratio

Generally, the SNR of an image is the ratio of the total number of photons from the target to the number of photons generated by various noise sources, such as background sky pollution, CCD dark current, and CCD read noise. In the context of SSA, a higher SNR ratio is a result of a brighter SO in the image plane. This implies a greater probability of successful detection, and more accurate photometry results [79].

The arrival process of photons incident on the CCD plane can be accurately modeled by a Poisson process. Therefore, this model is bound by the three main assumptions made for a Poisson process: the arrival of photons at the detector plane occurs one-at-a-time at a mean rate of Λ per unit time, Λ is stationary, and the number of photons incident on the CCD in two disjoint time intervals are independent [80]. These assumptions hold over the wavelengths of interest, therefore the number of photons incident on the CCD is the random variable Γ having poisson distribution with parameter Λ. The probability that Γ is equal to k number of photons is defined by Eq. (17) [81]. Note the capital greek letter lambda has

been used in place of the customary lowercase lambda in order to prevent confusing this term with wavelength.

$$\Gamma \sim Pois(\Lambda) = \frac{e^{-\Lambda}\Lambda^k}{k!} \tag{17}$$

With the random variable for number of photons incident on the CCD defined, it is now necessary to define what constitutes a successful detection. The term signal-to-noise ratio is introduced, where the "signal" is the number of photons incident on the CCD reflected by the SO, and the "noise" is the number of photons incident on the CCD from both the SO and background. A successful detection occurs when the signal received by the CCD reaches a certain threshold greater than the noise received by the CCD. The SNR of a measurement made with a CCD is typically defined as the quotient of the mean number of photons from the SO, μ_{SO}, by the standard deviation of photons from all noise sources, σ_{n} [82].

$$\mathrm{SNR} = \frac{\mu_{\mathrm{SO}}}{\sigma_{\mathrm{n}}} \tag{18}$$

An excellent discussion on the variance of noise sources is provided by Merline and Howell, so only the salient steps in deriving the SNR will be presented here [83]. The total signal integrated over the CCD, S, is calculated from the total count, C_i, the number of pixels occupied by the SO, m, the average background level, $\bar{n}$, and digitization offset, $\bar{d}$, as shown in Eq. (19). This equation is written in terms of analog-to-digital units (ADU), which are commonly refereed to as "counts" [83].

$$S = \sum C_i - m\bar{n} - m\bar{d} \tag{19}$$

To find the variance of the total, integrated signal a Taylor Series expansion is taken about the mean integrated signal, $\bar{S}$, as shown in Eq. (20) [83].

$$\sigma_S^2 = \sum_{i=1}^{m} \left(\frac{\partial S}{\partial C_i}\right)^2 \sigma_{C_i}^2 + \left(\frac{\partial S}{\partial \bar{n}}\right)^2 \sigma_{\bar{n}}^2 + \left(\frac{\partial S}{\partial \bar{d}}\right)^2 \sigma_{\bar{d}}^2 \tag{20}$$

It is emphasized that beginning with Eq. (20), the following equations are written in units of electrons and not ADU. So, the variance of the source signal, $\sigma_{C_S}^2$, the variance of the total signal, $\sigma_{C_i}^2$, the variance of the background noise, $\sigma_{\bar{n}}^2$, and the variance of the digitization offset, $\sigma_{\bar{d}}^2$, are defined in units of electrons. Because all of the coefficients in Eq. (19) are

constant, no terms higher than first order appear in Eq. (20). Additionally, the variance of the total signal, background, and digitization offset are assumed to be uncorrelated and zero mean, therefore no covariance terms appear in Eq. (20). This Taylor series can also be equivalently rewritten as shown in Eq. (21) [83].

$$\sigma_S^2 = \sum_{i=1}^{m} \sigma_{C_i}^2 + m\sigma_{\bar{n}}^2 + m\sigma_{\bar{d}}^2 \tag{21}$$

In Eq. (19) through Eq. (21), the subscript i is used to denote a pixel which lies in the array of pixels containing the SO. In this study, the major contributors to background noise are assumed to be counts from the radiant intensity of the background sky, C_S, counts from the dark current of the CCD, C_D, and read noise of the CCD, σ_r^2. The variance in the total signal in each i pixel is defined as shown in Eq. (22) [83].

$$\sigma_{C_i}^2 = \sigma_r^2 + \left(C_{i,\mathrm{SO}} + C_{i,\mathrm{D}} + C_{i,\mathrm{S}}\right) G \tag{22}$$

For clarity, the read noise of the CCD is given in units of electrons, as is typically found in CCD specifications available from the manufacturer, while the remaining terms have been converted from ADU to electrons via the CCD gain, G. The CCD gain defines the efficiency of a CCD sensor in converting electrons to ADU. The variance in the noise is defined as shown in Eq. (23) [83].

$$\sigma_{\bar{n}}^2 = \frac{1}{z^2} \sum_{j=1}^{z} \left(\sigma_r^2 + \sigma_{C_{j,\mathrm{D}}}^2 + \sigma_{C_{j,\mathrm{S}}}^2 + \sigma_{C_{j,\circ}}^2\right) \tag{23}$$

To quantify the signal reflected by the SO, one must also determine the average background noise and subtract it from the total signal. Because it is not possible with traditional CCDs to determine the source of individual electrons, the background noise level must be estimated. The simplest method for determining the background is to find the mean background noise from a random sample of z, "SO-free" pixels [24]. The subscript "j" is used to denote that these z pixels are a separate array from the m pixels occupied by the SO. Finally, the variance of the digitization offset is defined by Eq. (24), where σ_f^2 is the standard deviation of fractional counts lost to digitization in a single pixel [83].

$$\sigma_{\bar{d}}^2 = \frac{G^2}{m}\left(1 + \frac{m}{z}\right)\sigma_f^2 \tag{24}$$

Determining a specific value for σ_f requires several assumptions, and contributes a minor amount of noise, on the order of a few percent of the total read noise [83]. This is insignificant for purpose of SO detection, but interested readers can find more detail in Newberry [84]. Substituting Eqs. (22 - 24) into Eq. (21) yields a final expression for the variance in the integrated signal, as shown in Eq. (25) [83].

$$\sigma_S^2 = m\left(1+\frac{m}{z}\right)\sigma_r^2 + \sum_{i=1}^{m}\left[\left(C_i - C_i^{\circ}\right)G\right] + \frac{m^2}{z^2}\sum_{j=1}^{z}\left[\left(C_j - C_j^{\circ}\right)G\right] + m\left(1+\frac{m}{z}\right)G\sigma_f^2 \quad (25)$$

The final new superscript, $\circ$, indicates that these counts are due to direct current (DC) bias. In Eq. (25), the first term is the effect of readout noise on the source and noise integration, the second term is the photon noise, sometimes referred to as shot noise, in the source integration, the third term is the photon noise in the noise determination, and the fourth term is the variance due to the conversion from analog to digital units. The second and third term of Eq. (25) can be simplified as shown in Eqs. (26 - 27) [83].

$$\sum_{i=1}^{m}\left[\left(C_i - C_i^{\circ}\right)G\right] \simeq q_{\mathrm{SO}}t + m\left(q_{p,\mathrm{sky}} + q_{p,\mathrm{dark}}\right) \quad (26)$$

$$\sum_{j=1}^{z}\left[\left(C_j - C_j^{\circ}\right)G\right] \simeq z\left(q_{p,\mathrm{sky}} + q_{p,\mathrm{dark}}\right) \quad (27)$$

In Eq. (26) and Eq. (27), q_{SO} is the photon flux reflected by the SO as given by Eq. (8), $q_{p,\mathrm{sky}}$ is the photon flux per pixel from the background sky irradiance as defined by Eq. (16), the dark current per pixel is $q_{p,\mathrm{dark}}$, and t is the integration time, also called the exposure time, of the observation. Since the mean and variance of a Poisson distribution are equal to the rate parameter Λ, the mean and variance of electrons generated in a CCD from a SO observation can be defined by Eq. (28) and Eq. (29)[80].

$$\mu_{\mathrm{SO}} = \sigma_{\mathrm{SO}}^2 = q_{\mathrm{SO}}t \quad (28)$$

$$\sigma_{\mathrm{n}}^2 \approx q_{SO}t + m\left(1+\frac{1}{z}\right)\left[\left(q_{p,\mathrm{sky}} + q_{p,\mathrm{dark}}\right)t + \frac{\sigma_r^2}{n^2}\right] \quad (29)$$

The derivation of Eq. (29) from Eq. (25) includes one simplification and one enhancement made by Schildknecht [24]. The value of σ_f is approximately equal to $\sigma_f \simeq 0.3$ ADU when using the uniformly distributed assumption presented by Merline and Howell [83]. This is

relatively small compared to other variances, and is only necessary for precise photometry and not for detection of SO. Therefore, the last term in Eq. (25) can be ignored. The enhancement is the inclusion of the pixel binning factor, n. If the EO sensor is operated in a "binned" mode the read noise can be reduced. Substituting these two expressions into Eq. (18) yields Eq. (125). Eq. (125) is commonly referred to as the "CCD Equation."

$$\mathrm{SNR} = \frac{q_{\mathrm{SO}} t}{\sqrt{q_{\mathrm{SO}} t + m\left(1 + \frac{m}{z}\right)\left[\left(q_{p,\mathrm{sky}} + q_{p,\mathrm{dark}}\right) t + \frac{\sigma_r^2}{n^2}\right]}} \tag{30}$$

Despite its name, the CCD equation applies to many forms of EO sensors, including CMOS sensors, CCD sensors, or photon counters [24]. Thus, the signal term could represent the entire signal from a SO, or the signal from a single pixel [83]. As a result, comparing SNR values is highly dependent on the imaging area considered, and also the specific detecting algorithm utilized. In this work, Eq. (8) expresses the total signal in the streak of the SO across the image plane. As developed, all noise sources are computed on a per pixel basis. Therefore, the total number of pixels occupied by the SO on the image plane has a great impact on the total SNR [83].

3.3 SO Image Area

In the SNR equation m is the number of pixels occupied by the SO. For the purposes of defining the limiting magnitude, the main concern is the number of pixels occupied by an unresolved SO, i.e. a "point source" of light. For a point source, the number of pixels initially occupied by the SO, m_i, is affected by the IFOV and the point spread function (PSF) of SO intensity formed on the focal plane. The PSF is due to the blurring effects of optics, the atmosphere, and focus [78]. Theoretically, the PSF includes an infinite area, but the image size of point source is typically represented using the variance or "full width at half maximum" (FWHM) of its intensity distribution. To illustrate, Fig. 4 shows how the FWHM is defined as Δx where $f(x)$ is equal to half the maximum value of $f(x)$.

In this work, it is assumed the image is well focused. Therefore, the size of m_i is determined by the IFOV and the FWHM of the PSF. As described by Eq. (11), the IFOV defines the angular field of view, in radians, of a single pixel. If the IFOV is larger than the

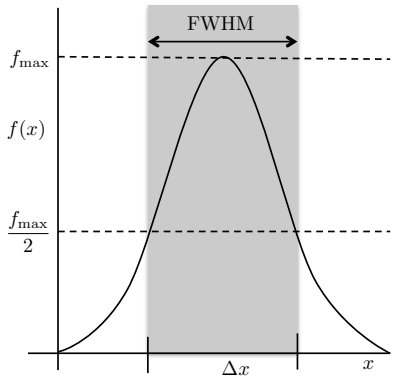

Figure 4: FWHM of Continuous Distribution

diameter of the PSF, as defined by the FWHM, then m_i is simply equal to a single pixel. The PSF is defined as the larger of two values: the PSF defined by the atmospheric seeing, or the PSF as a result of diffraction limiting.

The PSF due to atmospheric seeing can be theoretically evaluated, but PSF is temporally varying over fast time scales and accurate computation requires detailed knowledge of atmospheric composition which is typically unknown. Several COTS sensors also exist that are capable of measuring an average value of FWHM of atmospheric seeing. Thus, the FHWM of atmospheric seeing is considered a known variable in this analysis, and is defined to be θ_S.

The PSF due to diffraction limiting is the theoretical limit of an optical system's resolution due to the diffraction of light. For a perfectly circular aperture with no obscuration, the diameter of a point source is described by the "Airy disk." The angle in radians of the Airy disk is given by Eq. (127) [85].

$$\theta_A = \frac{2.44\,(\lambda)}{D} \tag{31}$$

It is important to note here that the diameter of the Airy disk is wavelength dependent, and therefore a weighted average for wavelength should be used in the same manner as Eq. (7). With the PSF diameters calculated for both diffraction and atmospheric seeing, the diameter is then chosen using the maximum function

$$\theta = \max\left(\theta_S, \theta_A, \text{IFOV}\right) \tag{32}$$

The initial number of pixels occupied by the SO in the image, is then defined by the

piecewise function described in Eq. (33).

$$m_i = \begin{cases} 1 & : \theta = \text{IFOV} \\ \frac{\pi(\theta N D)^2/4}{p^2} & : \theta \neq \text{IFOV} \end{cases} \tag{33}$$

When the optical system is perfectly tracking an SO, then the value of m_i is constant. However, when the relative velocity between the SO and telescope are different, such as the case when performing un-cued detection of SO, the captured image will contain SO streaks. For a SO streaking across the image plane, the number of pixels occupied by the incoming signal grows as defined by Eq. (126) where ω is in radians/s and IFOV is in radians [24]. It is important to note that ω is the relative velocity between the telescope motion and the SO.

$$m = m_i + \frac{\sqrt{m_i}\omega t}{\text{IFOV}} \tag{34}$$

A consideration is how fractional pixel values are handled in such a physics-based model. Eq. (33) assumes fractional values of pixels, whereas actual detectors are always comprised of discrete pixels. The piecewise function described in Eq. (33) prevents erroneous limiting magnitude estimates for the special case of observing small SO with wide FOV systems. Without establishing a lower bound on m_i, the continuous number of pixels occupied by the SO could be calculated as less than unity. This is problematic, as physically the light can never be incident on less than a single pixel. Even if the photons emitted by a SO are incident on a single pixel, it is challenging to distinguish between a "hot pixel" and a successful SO detection. While advanced detection techniques, such as multiple-hypothesis tracking, could be used to mitigate detection ambiguities, they are not considered here [86]. A final consideration is the accuracy of orbits estimated with extremely wide FOV optical systems. Chapter 4 outlines how the design methodology allows the system analyst to account for such issues.

CHAPTER IV

MULTI-OBJECTIVE DESIGN OF SDA ASSETS

This chapter outlines two different methodologies for designing optical systems tasked with SO detection and tracking. The first methodology, presented in §4.1 through §4.1.3, is intended for designing systems whose primary purpose is detecting previously undetected SOs to expand a SO catalog. The primary challenge in designing these systems is the lack of detailed knowledge about target SO parameters. Thus, the three novel performance metrics detailed in §4.1.1 through §4.1.3 enable the quantification of optical system performance with very few assumptions about the target SO population.

The second methodology, outlined in §4.1.4, is intended to design optical systems whose primary objective is SO catalog maintenance. Here, the challenge is not a lack of information about target SOs, but rather how quickly and efficiently sensor assets can be utilized to reacquire previously detected SOs. This additional data informs not only optimal SSA asset designs but also optimal operational schemes.

Both methodologies consider the actual optical design of the system as a "black box." There are many design variables, such as angles and sizes of mirrors or lenses, that constitute an optical system. However, the ones that are easily controlled in the COTS component Raven design paradigm are the aperture diameter, D, f-number, N, and pixel size of the CCD, p. These three variables will be treated as the design variables, $\mathbf{x}$, while all other parameters, $\mathbf{p}$, will be fixed at constant values.

$$\mathbf{x}^T = [D \ N \ p]^T \tag{35}$$

$$\mathbf{p}^T = [D_{\text{so}}, \ \text{FWHM}, \ I_B, \ QE, \ q_{p,\text{dark}}, \ R, \ \text{SNR}_{\text{alg}}, \ \omega, \ \Phi_0, \ \tau_{\text{atm}}, \ \tau_{\text{opt}}, \ \tau_{\text{s}}]^T \tag{36}$$

This optics-agnostic approach emphasizes the pixel level performance of a system and affords several advantages. While the motivation for the study is a ground-based Raven-class telescope, the developed methodology is not limited to a specific optical configuration

and enables a wide range of operating environments and optical designs to be considered. Consequently, the methodologies outlined here can be used to identify families of feasible designs which constitute candidates for further detailed design.

Since these methodologies are intended to be used during conceptual design phases, they do not consider geometric optical design. Therefore, neither methodology calculates items such as the total size of the flat field or optical aberrations [77]. If the analyst wants to verify that they are not considering a system that might encounter these issues, the easiest solution is to restrict the range of design variables under study. Using only higher f-numbers, smaller aperture diameters, or a combination of both can alleviate this problem. If the systems under consideration requires a large field of regard, then engineering solutions are available to mitigate these concerns during the detailed design phase [41]. Possible solutions include restricting the bandwidth of the system, ensuring short back focal lengths, or accepting larger spot sizes. Such considerations are outside the scope of this thesis and selecting COTS components ensures these issues will not be significant.

An additional concern not addressed in this thesis is that of system cost. While the primary motivation for small aperture, autonomous telescopes is their low cost, it is difficult for several reasons to predict the cost of conceptual designs generated using this methodology. While empirical curves could be fit to the aperture diameter, for example, technology generally decreases the cost of telescope components, especially electro-optical sensors, at a rapid pace. Consequently, any specific cost estimates presented in the thesis would be instantly outdated, and makes broad statements on drivers of total system cost difficult to predict. Another consideration is that budgets and costs are relative, and each stakeholder would identify affordability differently. Thus, this thesis presents a methodology which computes the performance of electro-optical systems only.

4.1 Multi-Objective Design Methodology

Optical systems tasked with detecting new SOs have three primary goals: to accurately generate initial orbit estimates, to detect the dimmest SOs possible, and to detect as many

SO as possibles. To quantify the performance of these optical systems, three novel performance metrics are developed. Attempting to optimize such as a system constitutes a multi-objective optimization (MOO) problem. Note that in this specific problem the maximization of all objectives is the desired solution, but the problem has been cast as a classical minimization problem by multiplying the utility functions by -1. Therefore, the following discussion will take place in terms of a minimization problem.

In multi-objective optimization, optimum design points are always compromise solutions; a decrease in the value of one objective can only be gained at the increase of another. The solutions desired are termed Pareto optimal solutions, and are often depicted as a Pareto frontier. A design point $\mathbf{x}$ in the feasible design space is called Pareto optimal if there is no other point $\mathbf{x}$ in the set that reduces at least one objective function without increasing another one. The ordering of these Pareto points is often referred to as "Pareto dominance." A point may be strongly or weakly dominant. A vector of objectives J strongly dominates another vector of objectives $\hat{J}$ if $J < \hat{J}$ and weakly dominates it if $J \leq \hat{J}$. A Pareto frontier is the set of strongly non-dominated points in objective space. The simple two objective case is depicted in Fig. 5, where the solid black line is the set of non-dominated Pareto points and the dominated points are represented by '+' signs. The "utopia point," J°, is defined as a physically unrealizable solution plotted in the objective space using a vector of each minimum. In Fig. 5, the utopia point is denoted by 'O," and each individual objective minimum is marked with squares. The utopia points are typically used as a benchmark to compare the relative merit of a selected design [87].

To ensure the resulting solutions are not skewed by the order of magnitude difference between the performance metrics, each is normalized as shown in Eq. (37). In this equation, the i^{th} objective is evaluated using the current vectors of design variables $\mathbf{x}$ and parameters $\mathbf{p}$. Conversely, ${J_i}^{\max}$ is the maximum value for J_i.

$$ {J_i}^{\text{norm}} = \frac{J_i(\mathbf{x}, \mathbf{p}) - {J_i}^{\circ}}{{J_i}^{\max} - {J_i}^{\circ}} \tag{37} $$

There are many well-known MOO strategies, and selection of one most appropriate depends on analyst preferences. If a priori preferences for certain performance criteria have

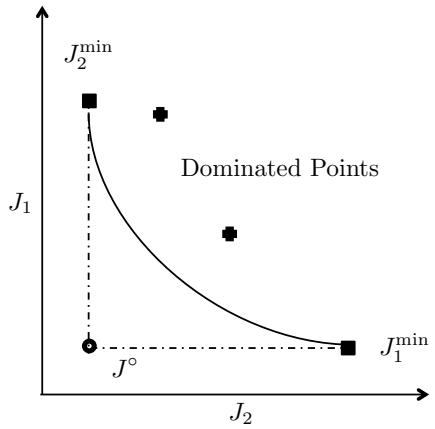

Figure 5: Sample Pareto Frontier

been established, a single Pareto optimal point is sought. Therefore, methods such as the Weighted Global Criterion Method or Bounded Objective Function Method may be appropriate. However, this work is concerned with design space exploration, and therefore seeks to generate the entire Pareto optimal frontier. Accordingly, methods such as Multi-Objective Genetic Algorithm or Weighted Min-Max Method are appropriate [87]. Because the objective functions derived in the following subsections are analytic, it is known that the objective space is continuous. Therefore, results presented are generated using grid search methods, where the Pareto frontier is selected using efficient subroutines detailed by Deb [88]. Grid search methods are used instead of evolutionary algorithms, as the ability to support selected designs is preferred. However, the MOO problem formulated here does not explicitly prevent their use and evolutionary algorithms can certainly be used as the analysts discretion.

4.1.1 Information Objective

When describing the resolution of an optical system, it is typical to quote the systems instantaneous field of view (IFOV). However, the actual quantity of interest in initial orbit estimation is not the resolution of the optical system, but rather the uncertainty in the initial orbit estimate. Calculating the accuracy of initial orbit estimates is not straightforward, as measurement uncertainties are passed through an estimation algorithm yielding a final converged orbit estimate [70, 89]. In a typical estimation algorithm, a measurement $\mathbf{z}$ is

made at time t_i of the true state $\mathbf{x}$ as given by Eq. (38). Here, $\mathbf{v_i}$ is the observation uncertainty which is often assumed to be zero mean Gaussian white noise with covariance $\mathbf{R}_i$, as described by Eq. (39) [90].

$$\mathbf{z}_i = \mathbf{h}\left(\mathbf{x}_i\right) + \mathbf{v}_i \tag{38}$$

$$\mathbf{v}_i \sim \mathcal{N}\left(\mathbf{0}, \mathbf{R}_i\right) \tag{39}$$

This approach advocates approximating initial orbit determination uncertainty using the Information Matrix (IM), as defined by Jazwinsky. The IM defines the amount of information, $\mathbf{F}$, contained about the state, $\mathbf{x}$, in the observations, $\mathbf{z}$, as shown in Eq. (40) [91].

$$\mathbf{F}(t_k, 1) \triangleq \sum_{t_i=1}^{t_k} \mathbf{\Phi}_{\mathrm{STM}}^T(t_i, t_k)\mathbf{H}^T(t_i)\mathbf{R}(t_i)^{-1}\mathbf{H}(t_i)\mathbf{\Phi}_{\mathrm{STM}}(t_i, t_k) \tag{40}$$

In Eq. (40), $\mathbf{\Phi}_{\mathrm{STM}}$ is the state transition matrix, $\mathbf{H}$ is the linearized measurement model matrix, and $\mathbf{R}$ the covariance of the observation uncertainty as defined above. The linearized measurement model is defined by

$$\mathbf{H}(t_i) = \left.\frac{\partial \mathbf{h}}{\partial \mathbf{x}}\right|_i \tag{41}$$

To determine the instantaneous amount of information obtained, $t_i = t_k = 1$ and consequently both the state transition matrix and model matrix are equal to identity. Substituting this result into Eq. (40) yields the Information Matrix contained in the observation of a single SO, as shown in Eq. (42).

$$\mathbf{F}(1, 1) = R^{-1} \tag{42}$$

From a decision-making perspective, the IM provided by captured images is not currently used directly to select optical designs; however, as shown in Eq. (42), the IM is known to be inversely proportional to the uncertainty in a measurement and therefore monotonic with the accuracy of initial orbit determinations [91]. In a Raven system, measurement uncertainties are a combination of the uncertainty of the SO location in the focal plane, uncertainties in optical system pointing, as well as uncertainties in the geometry and dynamics of the SO. Ideally, these uncertainties could be bound, thereby defining the best possible initial

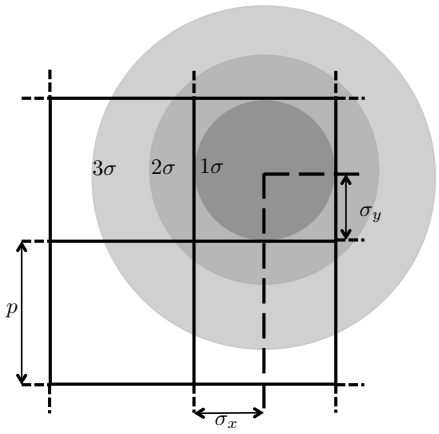

Figure 6: Measurement Uncertainty in Focal Plane Due to Pixel Resolution

orbit estimate possible from the collected observations. As this work is primarily concerned with optical system design, only the uncertainty in the SO location in the focal plane is considered.

In SSA missions, the measurement uncertainty of the mean pixel location of the SO is described by a multivariate normal distribution with parameters $\mathbf{a} = [\mu_x,\ \mu_y, \sigma_x^2,\ \sigma_y^2]$. As stated in Eq. (39), the observation noise is assumed to be zero mean. Additionally, most COTS CCD detectors utilize square pixels as shown in Fig. 6. Therefore, the measurement uncertainty in pixel location is equivalent in both directions and $\sigma^2 = \sigma_x^2 = \sigma_y^2$ and the IM can be written as given by Eq. (43).

$$\mathbf{F}(1,1) = \begin{bmatrix} \frac{1}{\sigma^2} & 0 \\ 0 & \frac{1}{\sigma^2} \end{bmatrix} \tag{43}$$

This vectorized result does not yield a single scalar information quantity, so the common practice is to take the trace of the IM, reducing Eq. (43) to Eq. (44) [92]. As a result, Eq. (44) defines the total amount of information contained in a single observation conduced by the SSA asset, such as a Raven system.

$$\mathrm{tr}(\mathbf{F}(1,1)) = \frac{2}{\sigma^2} \tag{44}$$

Uncertainty in SO location on the focal plane is a result of several factors including: signal-to-noise ratio, optical system resolution, sub-pixel centroiding, accuracy of reference stars' catalogued positions, orientation of the EO sensor, and systematic bias in sensors [24, 74, 78,

93]. Since the focus of this work is optical system design, only the optical system resolution is included in the uncertainty. The IFOV, as presented in Eq. (11), practically defines the resolution of images captures by a Raven system. By again examining Fig. 6, it is evident the conservative measure of maximum uncertainty in SO position, which is analogous to the observation noise covariance, is half the system's IFOV. Substituting the small angle approximation of Eq. (11) into Eq. (44) above yields the final expression for the information objective given by Eq. (45). Because the Information Matrix can have very large orders of magnitude change, a base 10 log operation is implemented for ease of interpreting results.

$$J_I(\mathbf{x}) = \log_{10}\left(\frac{2}{\sigma^2}\right) \propto \log_{10}\left[\frac{2}{\left(\frac{1}{2}\text{IFOV}\right)^2}\right] = \log_{10}\left[8\left(\frac{ND}{p}\right)^2\right] \tag{45}$$

As the information objective is the trace of the IM it is also equivalent to the volume of the information ellipsoid contained in a single image. As demonstrated in Eq. (44), the IM is inversely proportional to the measurement uncertainty. Therefore, by maximizing the information objective, the uncertainty in the initial orbit estimate of a SO due to optical system resolution will be minimized.

4.1.2 Limiting Magnitude Objective

With the accuracy of SO angular measurement defined, the next performance metric to consider is the detection capability of the Raven system. The brightness of a SO is typically defined using the apparent visual magnitude scale, and the dimmest object detectable by an optical system is termed its limiting magnitude [76]. The classical determination of a telescope's limiting magnitude assumes the observations are performed by a human eye [94]. These are certainly not applicable in a modern telescope system which uses semiconductor-based imaging sensors. Newer detection formulations, appropriate for EO sensors, rely on the signal-to-noise ratio which require a fixed exposure time [24]. Consequently, the concept of operations and the Raven system performance cannot be evaluated independently . To ameliorate this problem, a second metric is introduced to calculate the limiting magnitude of the telescope system while eliminating the dependence on exposure time.

Substituting Eq. (126) into the SNR equation while assuming z is large, and hence α equal to unity, leads to an expanded form of the SNR equation given in Eq. (46). This

assumption implies that a large number of pixels are utilized to accurately characterize the background noise levels. This assumption may lead to exaggerated values of limiting magnitude for small EO sensors or for frames containing crowded star fields.

$$\mathrm{SNR}^2 = \frac{(q_{\mathrm{SO}}t)^2}{q_{\mathrm{SO}} + \left(m_i + ND\sqrt{m_i}\omega t\frac{1}{p}\right)\left(q_{p,\mathrm{sky}} + q_{p,\mathrm{dark}} + \frac{\sigma_r^2}{n^2}\right)} \tag{46}$$

Another tacit assumption of the SNR equation is that all of the light transmitted to the focal plane is incident on the EO sensor. For larger FOV telescopes, this may not always be case. Some of these optical systems utilize a mosaic of EO sensors and the physical gaps between the chips result in lost light. These optical systems can be described by a "fill-factor" that defines the percentage of light captured by an EO sensor. Since the limiting magnitude metric is derived from the SNR equation, it also assumes that the fill factor is equal to unity.

Using L'Hospital's rule twice to find the SNR as time grows to infinity determines that maximum achievable SNR, resulting in Eq. (49). The first derivative is shown in Eq. (47) while the second derivative is shown in Eq. (48).

$$\frac{\mathrm{d}\left(\mathrm{SNR}^2\right)}{\mathrm{d}t} = \frac{2q_{\mathrm{so}}^2 t}{q_{so} + m_i\left(q_{p,\mathrm{sky}} + q_{p,\mathrm{dark}}\right) + \sqrt{m_i}\omega ND\frac{1}{p}\left[2t\left(q_{p,\mathrm{sky}} + q_{p,\mathrm{dark}}\right) + \frac{\sigma_r^2}{n^2}\right]} \tag{47}$$

$$\frac{\mathrm{d}^2\left(\mathrm{SNR}^2\right)}{\mathrm{d}t^2} = \frac{pq_{\mathrm{so}}^2}{\sqrt{m_i}\omega ND\left(q_{p,\mathrm{sky}} + q_{p,\mathrm{dark}}\right)} \tag{48}$$

Because the quantity of interest is the limiting SNR, simple algebraic manipulation yields Eq. (49). Here, the typical thought process must be altered. Think of Eq. (49) as the SNR required by a detection algorithm for a successful detection.

$$\mathrm{SNR}_{\mathrm{alg}} = \lim_{t\to\infty}\left(\sqrt{\mathrm{SNR}^2}\right) = \frac{q_{so}\sqrt{p}}{\left[\sqrt{m_i}\omega ND\left(q_{p,\mathrm{sky}} + q_{p,\mathrm{dark}}\right)\right]^{1/2}} \tag{49}$$

Thus, Eq. (8) is substituted for the value of q_{so}, and the required photon flux density emitted by the SO is defined as

$$\Phi_{\mathrm{SO}} = \frac{\mathrm{SNR}_{\mathrm{alg}}\left[\sqrt{m_i}\omega ND\left(q_{p,\mathrm{sky}} + q_{p,\mathrm{dark}}\right)\right]^{1/2}}{\tau_{atm}\tau_{opt}\left(\frac{\pi D^2}{4}\right)QE\sqrt{p}} \tag{50}$$

To convert this photon flux density to the apparent magnitude scale, the formula for converting flux to to visual magnitudes is applied. Using the photon flux density of a zero

magnitude object results in the limiting magnitude of the optical system.

$$m_v = -2.5 \log_{10} \left[\frac{\mathrm{SNR}_{\mathrm{alg}} \left[\sqrt{m_i} \omega N D \left(q_{p,\mathrm{sky}} + q_{p,\mathrm{dark}} \right) \right]^{1/2}}{\Phi_0 \tau_{atm} \tau_{opt} \left(\frac{\pi D^2}{4} \right) Q E \sqrt{p}} \right] \tag{51}$$

Using a simple law of logarithms results in the final limiting magnitude objective utilized in this study.

$$J_m \left(\mathbf{x}, \mathbf{p} \right) = 2.5 \log_{10} \left[\frac{\Phi_0 \tau_{atm} \tau_{opt} \left(\frac{\pi D^2}{4} \right) \mathrm{QE} \sqrt{p}}{\mathrm{SNR}_{\mathrm{alg}} \left[\sqrt{m_i} \omega N D \left(q_{p,\mathrm{sky}} + q_{p,\mathrm{dark}} \right) \right]^{1/2}} \right] \tag{52}$$

In taking the limit, the limiting magnitude afforded by this equation assumes an infinite exposure time. However, it is important to note that this capability may not be physically realizable for every SO observation. Appendix A of Schildknecht presents an excellent investigation into the effect differential motion between the SO and telescope boresight, denoted ω, has on the SNR. In the appendix, equations for the time necessary for a significant fraction, e.g. 90%, of the SNR to be reached are developed. It is found that the SNR, and hence limiting magnitude equation, tends towards its maximum value asymptotically with exposure time [24].

As a result, the limiting magnitude is typically approached in integration times as short as a few pixel crossings. This is a consequence of the fact that as the SO streaks through the focal plane the signal from the SO is spread over an increasing number of pixels, each with their own noise contributions. Meanwhile, the pixels initially occupied by the SO, m_i, only serve to accumulate more noise. In order to further demonstrate this point, the time to reach a specific SNR, derived by Howell, can be consulted [79].

4.1.3 Field of Regard

One final aspect of telescope systems not considered by the previous two metrics is the total field of view. For missions such as the "un-cued" detection of SOs, having a wide FOV is desirable. The expression for the total angular field of view (FOV), as a function of the previously defined instantaneous field of view (IFOV), along an axis of the EO sensor is given by Eq. (53).

$$\mathrm{FOV} = n_p \mathrm{IFOV} \tag{53}$$

In Eq. (53) n_p is the number of pixels in the EO sensor. Therefore, FOV increases with larger numbers of pixels, larger individual pixel size, and smaller f-numbers. As discussed, this methodology can not calculate the size of the flat field produced by telescope optics. As a result, it is not possible using the information presented in this work to say what the maximum number of pixels, and hence maximum field of view, would be. However, the total field of view is an important telescope metric. To capture the trade between information content, limiting magnitude, and field of view, the instantaneous field of regard, IFOR, metric is defined as given by Eq. (54).

$$J_R(\mathbf{x}) = \text{IFOR} = \text{IFOV}^2 = 4\arctan^2\left(\frac{p}{2ND}\right) \simeq \left(\frac{p}{ND}\right)^2 \tag{54}$$

This metric is simply the steradians covered by a single pixel. The IFOR metric is defined by design variables that enable the design methodology to retain its performance-centric focus, without require detailed information about internal optics. However, the pixel IFOR monotonically increases with the total FOV, and thus maximizing this metric is equivalent to maximizing the FOV.

4.1.4 Information Rate

The previous three performance metrics describe the performance capabilities of an optical system tasked with SO detection without requiring detailed optical design. However, recent shifts within the community have begun to emphasize alternative metrics, such as total system cost per byte of information gained and total number of bytes of information gained per unit time operational [95]. Since the amount of information contained in an observation of a single SO has been defined previously, the information rate could be calculated as given by Eq. (55).

$$J_{\dot{F}}(\mathbf{x}; t, \mathbf{p}) = \frac{(n_{\text{SO}})(\text{FOV})(J_I(\boldsymbol{x}))\Pr\left(\Gamma_{\text{so+n}} > \text{SNR}_{\text{alg}}\sigma_{\text{n}}\right)}{t} \tag{55}$$

Here, $\Gamma_{\text{so+n}}$ is the random variable for the number of photons reflected by the SO in a background reduced image. Also, n_{SO} is the number density of SO per deg^2 and FOV is the total field of view in deg^2. Intuitively, the quantity of information is divided by the exposure time.

In reality, the time between successive observations is dictated by several sequential events including: image exposure time, image download time, time to slew to the next SO, and time for telescope to "settle" on the next target. Of these, exposure time is the most logical choice for optimization. The other three times are not typically under the control of those assembling COTS optical systems. Ideally, they would be as close to zero as possible. Exposure time, however, must be carefully selected. Enough photons must be collected to successfully detect the object, but maximizing exposure time leads to inefficient use of SSA assets.

It is also necessary to include the probability of successful SO detection, $\Pr\left(\Gamma_{\text{so+n}} > \text{SNR}_{\text{alg}}\sigma_{\text{n}}\right)$. To successfully gain information about the SO, the SO must be successfully detected, which is not a deterministic event. Additionally, if probability were excluded, any optimization would result in designs with long focal lengths and small pixel sizes. Careful study of Eq. (52) reveals that such designs have poor detection sensitivity. By including the probability of successful detection, the impact of perturbing the aperture diameter is captured. As a result, the information rate performance index yields designs that would gather information at an optimal rate for the specified SO. This is useful in current design paradigms where a nominal target SO is defined to evaluate SSA asset performance for an entire class or orbital regime of SO.

The probability of detection is defined as the probability that the number of photons emitted by the SO is greater than the product of the SNR required by the detection algorithm and the variance of the signal emitted by all noise sources combined. This definition follows directly from the SNR equation, where the signal must be higher than a certain threshold above the noise. The difference here, is that the source and variance will be treated probabilistically rather than deterministically. As discussed in Chapter 3, the mean number of photons from the SO is given by Eq. (28) while the variance of all noise sources is provided by Eq. (29). The random variable which describes the number of photons in a background subtracted image of the SO is then given as the Normal distributions shown

below [81].

$$\begin{aligned}\Gamma_{\text{so+n}} &= \text{Pois}(\mu_{\text{SO+n}}) - \text{Pois}(\mu_{\text{sky}}) - \mathcal{N}(\mu_{\text{dark}}, \sigma^2_{\text{dark}}) - \mathcal{N}(\mu_{\text{r}}, \sigma^2_{\text{r}}) \\ &\approx \mathcal{N}(\mu_{\text{SO}}, \sigma^2_{\text{SO+n}})\end{aligned} \tag{56}$$

This approximation, given by the Central Limit Theorem, is valid when the number of incident photons is large. While defining "large" can be subjective, many have studied the error rates in approximating the Poisson distribution as normal. These references indicate this approximation is accurate when the number of incident photons is greater than 30 [96], with additional benefits seen when the "continuity correction" is applied [80]. For example, calculating the difference between a Poisson distribution with rate parameter $\Lambda = 10$ and its Gaussian approximation, the maximum error in the CDF is 0.02. While this error rate is sufficient for the results presented here, if further refinement is desired alternative approximations are available [97]. With this random variables assumed Gaussian, the probability that the signal is greater than the noise can found using the equation for the cumulative distribution function (CDF) of a Gaussian. Note that since the probably sought is for the number of photons greater than the threshold, the complementary CDF is utilized to define the probability of successful SO detection as given by Eq. (57).

$$Pr\left(\Gamma_{\text{so}} > \text{SNR}_{\text{alg}}\sigma_{\text{n}}\right) = \frac{1}{2}\left[1 - \text{erf}\left(\frac{SNR_{\text{alg}} \cdot \sigma_{\text{n}} - \mu_{\text{so}}}{\sqrt{2}(\sigma_{\text{SO}})}\right)\right] \tag{57}$$

To elaborate, a cartoon depicting the probability distribution function (PDF) of the difference in these two random variables is shown for a sample in Fig. 7. In the figure, the

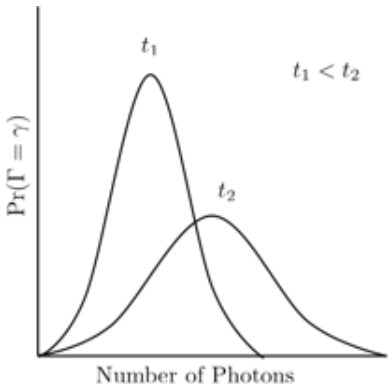

Figure 7: Evolution of PDF with Increasing Exposure Time

PDF with the least variance and largest magnitude mean is for a short exposure time, t_1.

However, as the exposure time is increased to t_2, the mean and variance increase, causing the PDF to exhibit lower kurtosis. This results is intuitive, as the increased exposure time allows photons from all sources, SO and noise, to collect on the EO sensor. The fact that photons from the SO collect at a higher rate is evident by examine Eq. (28) through Eq. (29). One can see that while the signal from the SO increases proportionally with time, the signal from noise sources increases with the square root of time.

Table 3: System Parameters

Parameter	Units	Atlanta	Antarctic	RECONSO
SO altitude	km	1000	1000	1000
SO diameter	m	1	1	1
SO elevation	deg	30	30	30
irradiance of magnitude 0 source	photons/s/m^2	$5.6 \cdot 10^{10}$	$5.6 \cdot 10^{10}$	$5.6 \cdot 10^{10}$
atmospheric seeing/mount jitter	arcsecond	4	1.5	.5
sky brightness	m_v/as^2	15	22	30
CCD quantum efficiency	-	.6	.6	.6
CCD dark current	e/pixel/s	.5	.5	.5
algorithm required SNR	-	4	4	4
atmospheric transmittance	-	.5	.7	1
optical transmittance	-	.9	.9	.9
secondary transmittance	-	.84	.84	1

4.2 Multi-Objective Design Case Studies

The multi-objective sizing methodology is utilized to evaluate the performance of optical systems in three optically diverse environments, as outlined in Table 3. The astute reader will notice slight discrepancies between the parameters in Table 3 and those listed in Eq. (36). Specifically, the altitude, elevation, and diameter of a SO are present in lieu of the slant range and relative velocity between the SO and the observer. This choice is made out of convenience for the analyst. Typically, a specific slant range or relative velocity is not known. However, parameters such as SO orbit typically are known. Therefore, several assumptions are made to ease the production of these results, which are not necessary for the validity of the methodology.

First, the optical systems are assumed to be operating in a "stare mode" where the SO is not actively tracked, thus the relative ω is simply the velocity of the SO [17]. Also, circular orbits were assumed when determining the orbital velocity of SO from orbital altitudes. Furthermore, some of the parameters specified are specific to CCD sensors. This choice is made to present a tractable number of results to demonstrate the methodology, but is by no means necessary. Suitable noise parameters could be introduced for alternative EO sensors.

To facilitate interpretation of the Pareto frontier results, three point designs are identified and discussed, as described in Table 4. The first, denoted by an '*', is a 0.2 m f/8 telescope utilizing the CMOS sensor found in the rear-facing camera on the iPhone 5s.

Table 4: Sample Point Designs

Point Design	Aperture Diameter (m)	F-Number	Pixel Size (μm)
Raven with iPhone (*)	0.2	8	1.59
Raven with CCD (O)	0.5	8	9
NASA MCAT (X)	1.3	4	15
RECONSO (∇)	$84 \cdot 10^{-3}$	1.4	9.7

While such systems are not generally considered "research grade", it serves to illustrate the performance that can be had with low cost COTS components. For comparison, configuration more typical of a Raven-class telescope, a .5m f/8 telescope, is denoted on the charts by an 'O.' The final design point, marked 'X," is NASA's MCAT and is representative of a more traditional large aperture telescope. The performance of these systems is evaluated in two locations: the Antarctic and Atlanta. Chosen for its dark skies and benign seeing, the Antarctic site is typical of a traditional observatory location. The second environment is the Georgia Tech observatory, located in Midtown Atlanta, at approximately N 33° 46′ 39″, W 84° 23′ 55″. This location exhibits bright skyglow and significant seeing effects which greatly impact performance.

To further demonstrate the flexibility of the presented methodology, a small aperture, space-based optical system is also presented. The specifications are those of a small CubeSat named "RECONnaissance of Space Objects" (RECONSO), which was successfully proposed by a research program at Georgia Tech to the Air Force Office of Scientific Research (AFOSR)/Air Force Research Lab (ARFL) University Nanosatellite Program (UNP)-8 Program. To simulate the space environment, the radiant sky intensity is set to a much higher value. While there certainty is not ambient light from city lights, there is ambient light from the Earth or Moon depending on specific problem geometry. This assumed value also implies that the systems do not have to cope with unresolved stars, nebulae, or other celestial phenomena. Additionally, while atmospheric seeing effects are no longer present, there is still the potential for vibrational loads which could impact performance.

The information rate results are presented for the 0.5 m f/8 Raven-class telescope operating in Atlanta, as described in both Table 3 and Table 4. For all of these results, several basic assumptions were made. First, all SO were approximated as spheres whose area was

calculated from an assumed diameter. The specular component of reflectivity for a sphere is given by Eq. (58) while the diffuse component is found in Eq. (59) [76]

$$\rho_{\text{spec}} = \frac{1}{4\pi} \tag{58}$$

$$\rho_{\text{diff}}(\psi) = \frac{2}{3\pi^2}\left[\sin(\psi) + (\pi - \psi)\cos(\psi)\right] \tag{59}$$

The components of reflectivity are dependent on the geometry of the observer-SO-Sun angle, ψ, termed the solar phase angle. A recent study has determined that a reasonable global, average value for the albedo of SO is 0.175. [98] It is assumed that specular and diffuse reflectivity contributed equally to the SO signature, an assumption supported by observational data. [25]

4.2.1 Pareto Frontier - Antarctica

Fig. 8 shows the Pareto surface for optical systems located in the Antarctic. The surface exhibits performance tradeoffs that are consistent with intuition. The peak of limiting magnitude performance is achieved for a system having the largest possible aperture diameter, shortest f-number, and largest pixels. Limiting magnitude performance then diminishes while information increases for combinations of larger f-numbers or smaller individual pixels. This is a result of the fact that the SO image occupies a greater number of pixels in the EO sensor, therefore increasing the amount of noise added "behind" the SO. Fig. 8

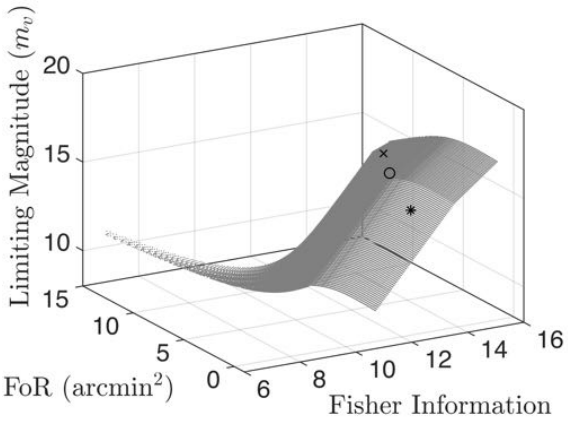

Figure 8: Pareto Frontier of SSA Optical Systems in Antarctic

also highlights three interesting point designs. The specific performances denoted by these

Table 5: Performance of Selected Point Designs in Antarctic

Optics System	Info. Metric	Lim. Mag. (m_v)	IFOR (arcmin^2)	IFOV (as)
0.2 m f/8 (*)	12.7	15.5	1.0E-05	1.93E-01
0.5 m f/8 (O)	11.9	17.8	6.0E-05	4.64E-01
1.3 m f/4 (X)	11.7	18.9	9.8E-05	5.95E-01

symbols are further detailed in Table 5. It was found that in dark skies, e.g. those in the Antarctic, increasing the aperture diameter from 0.2m to 0.5m yielded a limiting magnitude increase of 2.3 m_v. This is approximately equivalent to saying a 0.5m telescope could detect SO 8.3 times dimmer than a 0.2m telescope. However, increasing the aperture diameter from 0.5m to 1.3m yielded a 1.1 m_v limiting magnitude increase. Equivalently, a 1.3m telescope has the ability to detect SO 2.75 times dimmer than a 0.5m telescope. These results should not imply that large aperture telescopes are made obsolete by smaller aperture Raven-class telescopes. Indeed, some missions dictate detecting the smallest, dimmest SO. However, it is posited by the authors that the requirements of a majority of SSA researchers are satisfied by small aperture telescopes.

One benefit of the novel, analytical metrics is that if no design were to satisfy the desired performance the analytical Jacobians of the performance metrics are available. These define which design variables and parameters have the greatest impact on system performance. It is extremely important to note that the sensitivities may depend on other variables. Thus, changing the value of one variable may ultimately change the sensitivity of another. The sensitivities presented here were evaluated using the parameters set forth in Table 3 and the design variables were fixed as $[D, N, p] = [0.5\text{m},\ 8,\ 5\mu\text{m}]$.

Table 6: Information Content Sensitivities for Raven

Variables	$\delta J_I/\delta(\cdot)$	Variable Step Change
aperture diameter	.4	per .1 m
f-number	.25	per 1
pixel size	-4	per 1 μm

Table 6 shows the information metric sensitivities for a Raven telescope in both the Antarctic and Atlanta. These results are valid for both locations, as the partial derivatives of the information objective are a function solely of the design variable in question. When

interpreting these results, it is important to recall that the information metric is transformed using the $\log_{10}$ function. For example, the ratio between 0.4 and -4 is given by $10^{0.4+4}$. The fact that the aperture diameter has the greatest effect on the information objective can be attributed to two causes. The first is the fact that the performance metrics are developed in terms of f-number rather than focal length. As a result, increasing the aperture diameter increases the focal length. The second cause is the specific design point at which the values in Table 6 were calculated. $N = 8$ is a fairly large f-number, meaning an increase in 0.1 m aperture diameter would increase the focal length more than a change in N from 8 to 9.

Table 7 lists the sensitivities of limiting magnitude for a Raven in the Antarctic. These sensitivities are not provided in base units, but have been converted to increments that would most likely be used by the analyst. When interpreting these results, the positive and negative signs indicate the direction of change in the limiting magnitude for a unit increase in the variable listed in the last column. Care must be taken for the case of sky brightness, as an "increase" in 1 m_v/as^2 means the skies are darker, causing an increase in the limiting magnitude, implying the telescope can detect dimmer objects. It is interesting to note that even under "excellent" atmospheric conditions, the sky brightness and atmospheric seeing still have the greatest impact on system performance. However, of the parameters that constitute a telescope, the CCD dark current has the greatest impact on the limiting magnitude for the conditions and telescope design specified.

4.2.2 Pareto Frontier - Atlanta

The Pareto Frontier for SSA assets located in Atlanta is shown in Fig. 9. The greatest change in Fig. 9 compared to Fig. 8 is the dramatic difference in limiting magnitude performance. Examining Table 8 reveals that the sensitivity of each system has been degraded by at least 3.5 m_v. As a result, for systems operating around urban areas, there is little performance penalty for selecting faster f-number optics, or EO sensors with smaller pixels.

Table 9 lists the sensitivities for the limiting magnitude for a Raven-class telescope in Atlanta. Unsurprisingly, the sky brightness becomes a greater detriment to the overall detection capability of the system. Additionally, the design variable of greatest importance

Table 7: Limiting Magnitude Sensitivities for Raven in Antarctic

Variable	$\delta J_m/\delta(\cdot)$	Variable Step Change
sky brightness	3.86E-01	per 1 m_v/as^2
atmospheric seeing	-2.91E-01	per 1 as
algorithm required SNR	-2.71E-01	per 1
CCD dark current	-2.47E-01	per .1 electron/pixel/s
aperture diameter	2.17E-01	per .1 m
atmospheric transmittance	1.55E-01	per .1
CCD quantum efficiency	1.11E-01	per .1
SO diameter	-1.06E-01	per 1 m
optical transmittance	7.41E-02	per .1
secondary transmittance	-4.99E-02	per .1
f-number	-3.13E-02	per 1
pixel size	2.75E-02	per 1 μm
SO orbital velocity	-1.02E-04	per 1 as/s
slant range	1.89E-10	per 1 km

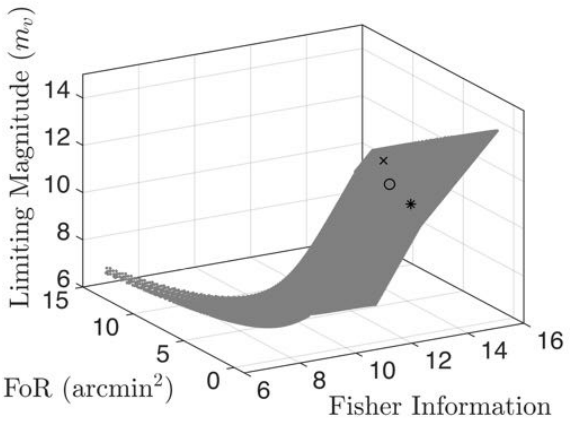

Figure 9: Pareto Frontier of SSA Optical Systems in Atlanta

Table 8: Performance of Selected Point Designs in Atlanta

Optics System	Info. Metric	Lim. Mag. (m_v)	IFOR (arcmin^2)	IFOV (as)
0.2 m f/8 (*)	12.7	11.9	1.0E-05	1.93E-01
0.5 m f/8 (O)	11.9	12.9	6.0E-05	4.64E-01
1.3 m f/4 (X)	11.7	13.9	9.8E-05	5.95E-01

to the designer trying to maximize the detection capability for a Raven in Atlanta is the aperture diameter. The SNR required for algorithm detection again plays a large role in the overall limiting magnitude, as it did in the Antarctic case.

This is an important consideration for another party that might be interested in this work. Due to its high level system performance emphasis, program managers looking to marginally increase performance of existing optical assets could use the performance sensitivities to allocate program funds. So, by evaluating the performance increase due to SNR threshold, the program manager may realize that devoting additional funds to software development or computational power rather than optics hardware may yield the best performance improvement for their investment.

Table 9: Limiting Magnitude Sensitivities for Raven in Atlanta

Variable	$\delta J_m/\delta(\cdot)$	Unit Step Change
sky brightness	5.00E-01	per 1 m_v/as^2
algorithm required SNR	-2.71E-01	per 1
aperture diameter	2.17E-01	per .1 m
atmospheric transmittance	2.17E-01	per .1
atmospheric seeing	-1.24E-01	per 1 as
CCD quantum efficiency	9.05E-02	per .1
secondary transmittance	-6.46E-02	per .1
optical transmittance	6.03E-02	per .1
SO diameter	-4.55E-02	per 1 m
f-number	-5.91E-04	per 1
CCD dark current	-5.08E-04	per .1 electron/pixel/s
SO orbital velocity	-1.02E-04	per 1 as/s
pixel size	5.64E-05	per 1 μm
slant range	8.06E-11	per 1 km

4.2.3 CubeSat RECONSO

While the primary motivation of this study was better understanding of Earth-based observatories, the methodology is general enough to be extended to all optical systems. Showcasing this ability, results presented here are for a small, space-based optical system tasked with SO detection. The largest simplification made in this modeling effort was a lack of of detail concerning various "sky brightness" contributions such as moon glow, earthshine, unresolved stars, nebulae, or other celestial phenomena. More detailed modeling would be

necessary if the ultimate subject of this study were space-based, but for the current effort it is worthwhile to reinforce how darker skies impact design tradeoffs.

Fig. 10 illustrates the Pareto frontier for space-based optical systems. The increased convexity exhibited by the surface is due to a lack of light pollution, as compared to those frontiers depicted in Fig. 8 or Fig. 9. Also intuitively, Fig. 10 demonstrates that utilizing aperture diameters larger than those suitable for CubeSats, space-based platforms are capable of viewing much smaller SO than terrestrial installations. The small CubeSat

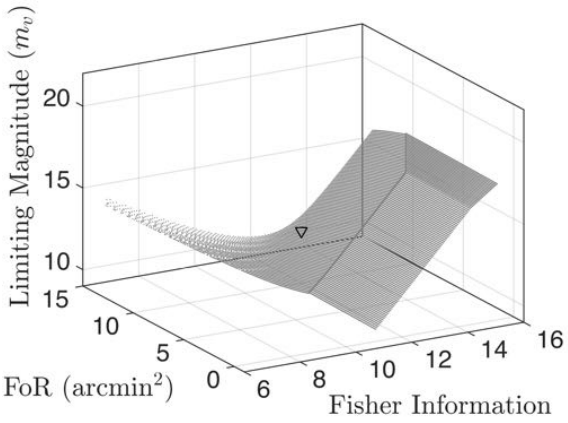

Figure 10: Pareto Frontier of SSA Optical Systems in Space

Table 10: Performance of RECONSO in LEO orbit

Optics System	Info. Metric	Lim. Mag. (m_v)	IFOR (arcmin^2)	IFOV (as)
0.084 m f/1.4 (∇)	12.7	11.9	1E-05	17.01E+00

RECONSO is denoted in Fig. 10 using a '∇'. In such a system, the CubeSat form factor constrains the aperture diameter to be small and focal lengths short. Such systems will inevitably have greater limiting magnitudes than information gathering ability.

The sensitivities for a small CubeSat like RECONSO are presented in Table 11. As noted previously, the RECONSO spacecraft is limited by its small form factor, with its small aperture diameter becoming the greatest detriment to its performance. Additionally, the dark and clear viewing conditions cause the dark current of the CCD sensor to become a much greater noise source compared to ground-based assets.

Table 11: Limiting Magnitude Sensitivities for CubeSat RECONSO

Variable	$\delta J_m/\delta(\cdot)$	Variable Step Change
aperture diameter	1.29E+00	per .1 m
CCD dark current	-1.01E+00	per .1 electron/pixel/s
f-number	-7.29E-01	per 1
pointing jitter	-3.02E-01	per 1 as
algorithm required SNR	-2.71E-01	per 1
CCD quantum efficiency	1.75E-01	per .1
optical transmittance	1.17E-01	per .1
atmospheric transmittance	1.09E-01	per .1
pixel size	1.04E-01	per 1 μm
SO diameter	-8.91E-02	per 1 m
sky brightness	3.37E-02	per 1 m_v/as^2
secondary transmittance	-4.35E-05	per .1
SO orbital velocity	-7.95E-05	per 1 as/s
slant range	1.27E-10	per 1 km

4.2.4 Information Rate

The results presented here use the information rate performance index to predict the performance of an SSA sensor. The same radiometric model used in the previous methodology is also used to calculate the photon flux from the SO and background sky. The photon flux values needed as arguments for Poisson distributions can be found from Eq. 8 and Eq. 16. In these results, the number of pixels occupied by the SO is held constant through the entire exposure. This situation describes the case where the telescope is actively tracking the SO. In Fig. 11 and Fig. 12, the contour lines represent probabilities of 5%, 25%, 50%, 75%, and 95% in ascending order. Fig. 11 shows the probability of successful SO detection as a function of both exposure time and aperture diameter for a specific SO. These results use the system parameters for the Antarctic as defined in Table 19. Fig. 12 shows how the probability of successfully detecting the SO varies as a function of the exposure time and SO brightness, for a .4 m f/3.8 Raven-class telescope with a CCD comprised of 9 μm pixels. The probability of detection in both figures starts close to zero, with the order of magnitude ranging from 10^{-4} for the smallest aperture diameter to 10^{-7} for the largest aperture diameter. This is a result of the f-number being held constant, therefore the focal length of the larger diameter scopes is also larger. It can also be seen that after some exposure time, all these design points eventually reach a probably of detection equal

to unity. Fig. 13 illustrates the information rate gain for several telescopes of different

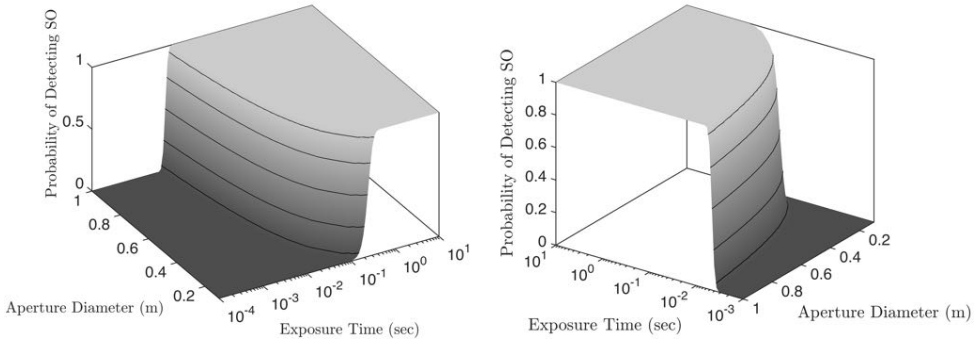

(a) For SO = 13.3 m_v (b) For SO = 13.3 m_v

Figure 11: Probability of Successful SO Detection

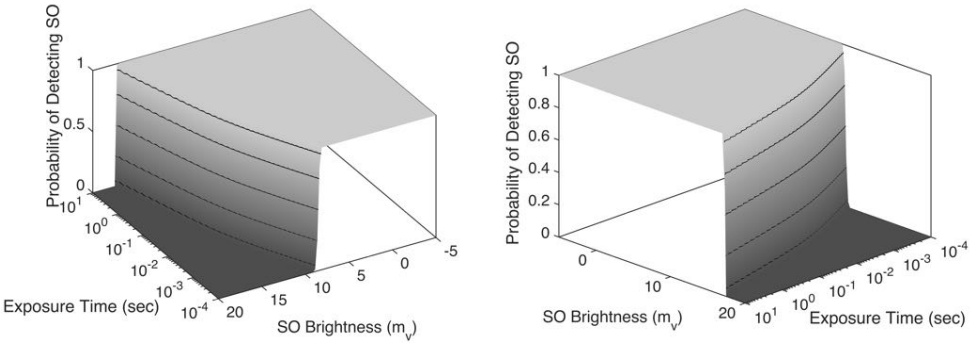

(a) For D = 0.5m (b) For D = 0.5m

Figure 12: Probability of Successful SO Detection

aperture diameters, using the same data that generated Fig. 11. Generally, Fig. 13 can be broken into two sections. From $t = 0$ sec. until $t_{max(\mathrm{Pr})}$ sec. the probability of detection the SO is very low. The length of this period is dependent upon aperture diameter, environmental conditions, and SO parameters. If design variables vary to increase the telescopes sensitivity, the time of peak information gain moves closer to $t = 0$ s. Once the mean of the difference distribution becomes greater than 0, the information rate peaks. The rapid decline in information rate is due to the fact that the rate of probability increase due to additional time in a single exposure is not greater than simply starting a new exposure with equivalent probability. Finally, the sensitivities of information rate performance index are presented in Table 12. Unsurprisingly, the exposure time has the greatest impact on the

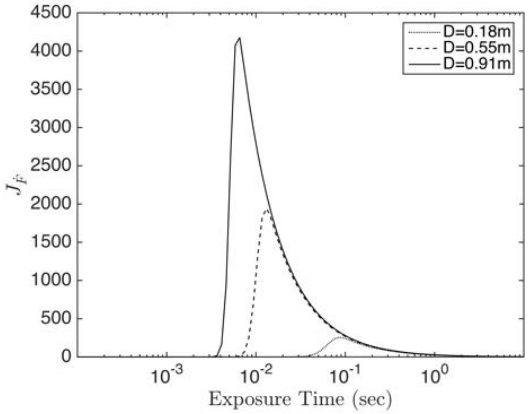

Figure 13: Information Rate vs. Exposure Time for Different Apertures

systems ability to maximize the information rate. What is surprising, is that the design parameters of the telescope now all have the greatest impact on system performance, in contrast to previous performance metrics which were dominated by environment and SO parameters. It is intuitive that the designs with the highest information rate performance would be those systems with large diameters and large pixel pitch. However, the decision maker must be cautious, as a large FOV is sometimes desired, and a large pixel pitch may push the design away from this objective. But, as seen the focal length and pixel size have relatively the same order of magnitude impact. As a result, decision makers in the position of needing a large FOV would be best to allocate program funding for large CCDs with small pixels. Additionally, the SO orbital velocity has no impact on the system performance because the results presented are for the case where the telescope is slewing at the same rate as the SO. Finally, the decision maker should be cognizant of the physical limitations on exposure time enforced by the length of streaking stars through the image plane.

4.3 Summary

A radiometric model, defined in consistent nomenclature, is defined which describes the path photons take from the Sun to the telescope's EO sensor payload. Consequently, SSA researchers will be able to successfully duplicate the systems studies presented here. Three novel performance metrics are motivated and derived which define the ability of an optical

Table 12: Information Rate Sensitivities for Raven in Atlanta

Variable	Sensitivity	Unit Step Change
time	-8.98E-01	per 1 s
aperture diameter	6.77E-02	per .1 m
f-number	4.20E-02	per 1
pixel size	-3.74E-02	per 1 μm
SO diameter	2.12E-03	per 1 m
algorithm required SNR	-5.20E-04	per 1
atmospheric transmittance	2.12E-04	per .1
CCD quantum efficiency	1.74E-04	per .1
optical transmittance	1.16E-04	per .1
albedo	6.07E-05	per .01
sky brightness	1.78E-05	per 1 m_v/as^2
atmospheric seeing	-8.86E-06	per 1 as
secondary transmittance	-2.30E-06	per .1
CCD dark current	-1.81E-08	per .1 electron/pixel/s
read noise	-3.61E-09	per 1
slant range	-3.76E-12	per 1 km

space surveillance asset for to detect, track, and characterize SO. These performance metrics form the basis of a well-posed multi-objective optimization problem. The generation of Pareto efficient frontiers provide a means for designers to identify "knee-in-the curve" performance tradeoffs, and quickly evaluate SSA asset performance relative to mission requirements. These Pareto frontiers are intended to be used as a part of the conceptual design phase, and provide insight into the performance of optical systems in the end user's specific optical environment. This enables systems designers to quickly identify feasible families of optical designs, which are candidates for detailed optical design. Sensitivities of performance metrics are also derived, allowing the identification and ranking of major system performance drivers which may be under the designer's control. These can also be used by decision makers to determine the performance improvements afforded by incremental upgrades to an existing design point. An information rate performance index is also defined, which enables the designer to compare how system design variables and exposure time influence the successful detection and operation of SSA assets.

Generally, it was found that optical systems with large f-numbers and small pixel sizes sacrificed less detection sensitivity under light polluted skies, like those found in urban environments, than under darker skies. For space-based SSA assets, the lack of background

radiant intensity dictates that low noise EO sensors be utilized to maximize limiting magnitude. It is also shown that in all optical environments, the SNR threshold required by the detection algorithm largely influences the overall detection capability of the system. Therefore, program funds may be better invested in more sophisticated software rather than more sophisticated optical hardware. Finally, several trade studies demonstrate the efficacy of small aperture diameter telescopes. While large aperture telescopes will continue to be necessary for SSA assets which contribute to the SSN, this work demonstrates that the requirements of a majority of SSA researchers may be met by small aperture telescopes, such as those built according to the Raven design paradigm.

CHAPTER V

LIGHT CURVE INVERSION

Using the radiometric principles of Chapter 3, a physics based noise model is described in §5.1. Following this, §5.2 summarizes the how the dynamics of an agile SO can be modeled with exponentially correlated angular accelerations, i.e. the Singer model. Finally, §5.3 details how the proposed dynamics model greatly reduces computational burden when coupled with a Rao-Blackwellized particle filter.

5.1 Measurement Noise Model

This work utilizes the photon flux incident on the CCD for simulating SO light curves and measurement variance. The radiometric measurement function captures the noise present in an image as a function of optical and environmental parameters, as shown in Eq. (60). This stands in contrast to much of the literature in the field, which uses visual magnitudes and a time invariant measurement variance. Because the number of photons incident on an EO sensor are typically on the order of 10^3 and higher, this Poisson process is well approximated by a Gaussian distribution, leading to the definition of measurement noise in Eq. (61).

$$y_k(\mathbf{x}, t_k) = q_{\mathrm{SO}}(\mathbf{x}, t_k) + v_k(\mathbf{x}, t_k) \tag{60}$$

$$v_k(\mathbf{x}, t_k) \sim \mathcal{N}\left(\mathbf{0}, R_k(\mathbf{x}, t_k)\right) \tag{61}$$

In Chapter 3, the variance of a SO signature captured by an EO sensor is defined by Eq. (29). In this equation, the values of atmospheric losses and sky brightness are deterministic. However, the phase and position of the moon, time of night, presence of clouds, and scintillation effects all cause the atmospheric transmittance and radiant sky intensity to be random variables. Atmospheric transmittance and radiant sky intensity vary temporally and spatially, and both typically increase near the local horizon. Since this work simulates the SO light curve over a short time period, the radiant sky intensity is treated as constant

while the atmospheric transmittance is treated as a random variable. For stars near zenith the atmospheric transmittance is best described as a Gaussian, log-normal, or F distribution, depending on the power of the scintillation [99]. For simplicity of implementation, this work will implement the atmospheric transmittance as a normally distributed random variable.

Consequently, the measurement variance is best described by a class of nonhomogeneous Poisson processes, termed mixed Poisson processes. A mixed Poisson processes is a Poisson process where the intensity, i.e. rate parameter of the Poisson distribution, is itself dependent on separate random variables as shown in Eq. (62).

$$P(\zeta < z_p) = \int_0^\infty \frac{e^{-\lambda}\lambda^{z_p}}{z_p!} G(\lambda)\ \mathrm{d}\lambda \tag{62}$$

Generally, ζ is the Poisson distributed random variable where the rate parameter is determined by $G(\lambda)$, termed the mixing distribution. In this work specifically ζ is the number of photoelectrons registered by the EO sensor and the mixing distribution $G(\lambda)$ is the atmospheric transmittance.The variance of a mixed Poisson process has been analytically derived to be greater than that of a homogenous Poisson process, as shown in Eq. (63) [100, 81, 101].

$$Var(\zeta) = E(\zeta^2) - [E(\zeta)]^2 = E(\lambda) + Var(\lambda) \tag{63}$$

Examining Eq. (29), the first term, representing the shot noise component, is the only term subjected to losses from atmospheric transmittance. Therefore, the mean and variance of the shot noise is defined by

$$E(\lambda) = \left(\Phi_{\mathrm{SO}}\tau_{\mathrm{opt}}\left(\frac{\pi D^2}{4}\right)\mathrm{QE}\ t_I\right)\mu_{\mathrm{atm}} \tag{64}$$

$$Var(\lambda) = \left(\Phi_{\mathrm{SO}}\tau_{\mathrm{opt}}\left(\frac{\pi D^2}{4}\right)\mathrm{QE}\ t_I\right)^2\sigma^2_{\mathrm{atm}} \tag{65}$$

One can define a time dependent zero mean Gaussian white noise using the covariance defined by Eq. (66). Comparing the deterministic noise of Eq. (29) to Eq. (66) reveals that the only difference is the addition of the second term in Eq. (66), which includes the effect of the varying atmosphere Eq. (66)

$$R_k(\mathbf{x}, t_I) \approx E(\lambda) + Var(\lambda) + m\left(1 + \frac{1}{z}\right)\left[\left(q_{p,\mathrm{sky}} + q_{p,\mathrm{dark}}\right)t + \frac{\sigma_r^2}{n^2}\right] \tag{66}$$

As a demonstration of the accuracy of the radiometric model, and to further illustrate the error of using constant magnitude measurement error, refer to Fig. 14. These 2,829 observations of GALAXY 15 were experimentally collected in May and June of 2015 using a Raven-class telescope located in Kihei, HI. The 16" f/5.628 Raven telescope utilized a Apogee U47 CCD, a Johnson R filter, and a 5 second exposure time. To generate the radiometric model represented in Fig. 14 the atmospheric transmittance is assumed to be $\tau_{\text{atm}} \sim \mathcal{N}(.6, .01)$ (unitless) and the radiant sky intensity is assumed to be $L_{\text{sky}} = 16.5$ m_v/arcsec^2. In Fig. 14 the gray dots are the experimentally calculated observations, the

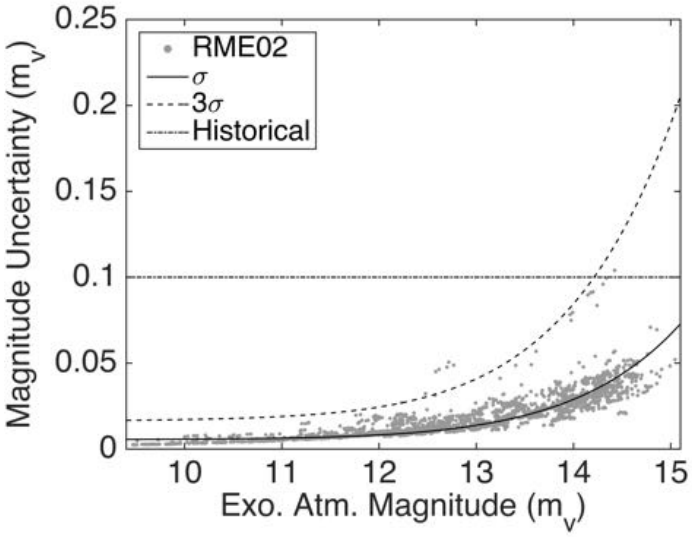

Figure 14: Measurement Noise of GALAXY 15 Observations

black line is the radiometric model, and the dashed black line is a constant measurement noise of 0.1 m_v. For this specific Raven-class telescope the historically assumed magnitude noise is greater than actual system noise, but this trend should not be construed to be true for all systems. Examining Eq. (29), for example, indicates that the historically assumed 0.1 m_v noise could underrepresent the noise of a system observing dim objects under very bright skies.

Careful inspection of Fig. 14 reveals that almost all experimentally determined measurement noises lie within the 3σ bound. While the outlying points could be the .03% of points expected outside the 3σ bound, it is important to note additional sources of noise that are not captured in our model. Because the model presented in this work does not

simulate individual images, one source of error present in experimentally obtained data but not captured by the model are uncertainties in the star catalog utilized in the conversion from instrumental counts to visual magnitude. Another source of error is the assumption of a constant sky brightness, where the phase of the moon and elevation of the telescope at the time of observation both ensure the sky brightness is varying both spatially and temporally. Finally, local weather conditions, such as cloud cover, can cause abrupt changes in atmospheric transmittance which are not captured by the model.

Using the radiometric model developed in this work, it is possible to simulate much of the experimentally produced observed noise. By modeling the stochastic process of photon arrival on the EO sensor image plane, the measurement variance is consistently determined for all SO signatures. Additionally, by correctly defining the photon noise, the photon radiance model developed here is also time varying. Thus, the measurement variance is accurate for measurements constituting the SO light curve. Finally, it should be noted that alternative measurement models using radiance as defined in the SI system, i.e. $W/m^2/sr$, would also afford these benefits. However, dark current and read noise are typically defined in manufactures' data sheets in terms of electrons, making the presented model easier to implement in practice.

5.2 Exponentially Correlated Angular Velocity Model

The light curve attitude estimation problem involves estimating both attitude and angular velocity states where attitude kinematics are well known but the angular velocity dynamics may be unknown due to unknown control torques, unknown inertia tensors, and unknown disturbance torques. This work seeks to account for all of these unknowns using an exponentially correlated process noise model. The general continuous time dynamics of such a problem with scalar measurements can be described by Eq. (67).

$$\begin{aligned} \dot{\mathbf{x}}(t) &= \mathbf{f}\left(\mathbf{x}, t\right) + \mathbf{G}\left(\mathbf{x}, t\right) \mathbf{w}(t) \\ y(t) &= h\left(\mathbf{x}, t\right) + v_k\left(\mathbf{x}, t\right) \end{aligned} \tag{67}$$

It is emphasized that the measurement is defined by Eq. (60) for the light curve inversion problem. The system state is defined as $\mathbf{x}^T = [\boldsymbol{\theta}_I^{B^T} \boldsymbol{\omega}^T]^T$ where $\boldsymbol{\theta}_I^B$ are the 3-2-1 Euler

angles defining the rotation between the SO body frame, B, to the inertial frame, I, and the angular velocity of the SO is denoted by $\boldsymbol{\omega}$. The true state dynamics for SO rotational motion is given by Euler angles kinematic relationship and Euler's rotational equation of motion.

$$\begin{bmatrix} \dot{\boldsymbol{\theta}}_I^B \\ \dot{\boldsymbol{\omega}} \end{bmatrix} = \begin{bmatrix} \mathbf{B}(\boldsymbol{\theta}_I^B)\boldsymbol{\omega} \\ -\mathbf{J}^{-1}\left(\boldsymbol{\omega} \times \mathbf{J}\boldsymbol{\omega}\right) + \mathbf{J}^{-1}\mathbf{T} \end{bmatrix} \tag{68}$$

where

$$\mathbf{B}(\boldsymbol{\theta}_I^B) = \frac{1}{\cos\theta_2} \begin{bmatrix} 0 & \sin\theta_3 & \cos\theta_3 \\ 0 & \cos\theta_2\cos\theta_3 & -\cos\theta_3\sin\theta_3 \\ \cos\theta_2 & \sin\theta_2\sin\theta_3 & \sin\theta_2\cos\theta_3 \end{bmatrix} \tag{69}$$

Here, $\mathbf{J}$ and $\mathbf{T}$ represents the true inertia tensor matrix and the sum of all applied control and external torques respectively. For agile SO the true inertia and torques acting on a SO are typically unknown. The resultant time varying accelerations of maneuvering objects are thus modeled as a random process. Random processes described in the literature can be classified in 3 general groups: white noise models, Markov process models, and semi-Markov jump process models [102].

White noise models have been previously applied to the SO attitude estimation problem by Wetterer et al. [52] Holzinger et al. [51]. The angular velocity dynamics can account for un-modeled torques $\mathbf{T}$ by representing this term as additive process noise, $\mathbf{w}$, and Eq. 70 becomes

$$\dot{\boldsymbol{\omega}} = -\mathbf{J}^{-1}\left[\boldsymbol{\omega}\times\right]\mathbf{J}\boldsymbol{\omega} + \mathbf{w} \tag{70}$$

where the stochastic process $\mathbf{w}$ has spectral density matrix $E\{\mathbf{w}(t)\mathbf{w}(t-\tau)\} = \bar{\mathbf{Q}}_{\mathbf{w}}\delta(\tau)$ and $\delta(\tau)$ is the kronecker delta. This representation is still problematic since $\mathbf{J}$ in general is unknown and although inertia parameters can be added to the estimation process they increase the dimensionality of the problem and suffer from observability issues. Holzinger et al. overcame these issues by modeling both $\mathbf{J}^{-1}\mathbf{T}$ and $-\mathbf{J}^{-1}\left(\boldsymbol{\omega} \times \mathbf{J}\boldsymbol{\omega}\right)$ with process noise described by Eq. (71) [51].

$$\begin{bmatrix} \dot{\boldsymbol{\theta}}_I^B \end{bmatrix} = \begin{bmatrix} \mathbf{B}(\boldsymbol{\theta}_I^B)\left(\boldsymbol{\omega}_\mu + \delta\boldsymbol{\omega}_0\right) \end{bmatrix} \tag{71}$$

$$\delta\boldsymbol{\omega}_0 \sim \mathcal{N}\left(\mathbf{0}, \mathbf{Q}_\omega\right) \tag{72}$$

Using this white noise process, the mean motion of the SO can be defined as ω_μ and motion about this nominal trajectory is modeled by the process noise with appropriately sized $\delta\boldsymbol{\omega}_0$. If the mean motion is unknown, then $\boldsymbol{\omega}_\mu = \mathbf{0}$ and $\mathbf{Q}_\omega$ can be sized such that $\delta\boldsymbol{\omega}_0$ is representative of SO maneuver capability.

This work adapts a Markov process model, first proposed in the 1970's to track maneuvering aircraft. Known by its inventor, the "Singer model" defines the target accelerations as correlated in time during a maneuver [103]. In this work, the angular accelerations, $\dot{\boldsymbol{\omega}}(t) = \boldsymbol{\alpha}(t)$, are assumed to be correlated in time with the autocorrelation defined by Eq. (73).

$$R_\alpha(\tau) = E\left[\boldsymbol{\alpha}(t)\boldsymbol{\alpha}(t+\tau)\right] = \sigma_m^2 e^{-\beta|\tau|}\mathcal{I}_{3\times 3} \tag{73}$$

In Eq. (73), σ_m^2 is the resulting variance of the maneuvering target body angular acceleration and β is the inverse of the maneuver acceleration time constant, τ. Taking the Laplace transform, $\mathcal{L}\{\cdot\}$, of the autocorrelation $R_\alpha(\tau)$ yields an equivalent power spectrum in the frequency domain, $R_\alpha(s)$, as shown.

$$R_\alpha(s) = \mathcal{L}\{R_\alpha(\tau)\} = \frac{-2\beta\sigma_m^2}{(s-\beta)(s+\beta)} \tag{74}$$

The angular acceleration can therefore be expressed as the 2nd order Markov process shown below.

$$\dot{\boldsymbol{\alpha}}(t) = -\beta\boldsymbol{\alpha}(t) + \mathbf{w}(t) \tag{75}$$

The process noise of the angular acceleration, $\mathbf{w}(t)$, is driven by the power spectral density of the angular acceleration, as given by Eq. (141).

$$Q_\alpha(\tau) = 2\beta\sigma_m^2\delta(\tau)\mathcal{I}_{3\times 3} \tag{76}$$

Without loss of generality, one can define different time constants and acceleration variances for each axis of the SO body fixed frame. Letting the subscripts 1 through 3 denote each orthogonal axis yields

$$Q_\alpha(\tau) = 2\delta(\tau)\left[\beta_1\ \beta_2\ \beta_3\right]^T\left[\sigma_{m,1}^2\ \sigma_{m,2}^2\ \sigma_{m,3}^2\right] \tag{77}$$

Implementing the Singer model, where the angular velocities are exponentially correlated, leads to Eq. (78), the continuous dynamics model proposed in this work for agile SO.

Similarly to Eq. (139), $\boldsymbol{\theta}_I^B$ defines the relationship between the body angular rates and the attitude coordinates used to represent SO(3) in the inertial frame.

$$\begin{bmatrix} \dot{\boldsymbol{\theta}}_I^B \\ \dot{\boldsymbol{\omega}} \\ \dot{\boldsymbol{\alpha}} \end{bmatrix} = \begin{bmatrix} \mathbf{0}_{3\times3} & \mathbf{B}\left(\boldsymbol{\theta}_I^B\right) & \mathbf{0}_{3\times3} \\ \mathbf{0}_{3\times3} & \mathbf{0}_{3\times3} & \mathcal{I}_{3\times3} \\ \mathbf{0}_{3\times3} & \mathbf{0}_{3\times3} & \operatorname{diag}\left(-\boldsymbol{\beta}\right) \end{bmatrix} \begin{bmatrix} \boldsymbol{\theta}_I^B \\ \boldsymbol{\omega} \\ \boldsymbol{\alpha} \end{bmatrix} + \begin{bmatrix} \mathbf{0}_{3\times3} \\ \mathbf{0}_{3\times3} \\ \mathcal{I}_{3\times3} \end{bmatrix} \mathbf{w} \tag{78}$$

To implement the model in discrete time, the spectral density matrix must be related to the discrete time exponentially correlated process noise. The resultant discrete process noise for the attitude and angular velocity is given[103],

$$\mathbf{Q}_k(t_{k+1}, t_k, \mathbf{x}) = \int_{t_k}^{t_{k+1}} \boldsymbol{\Phi}(t_{k+1}, \mathfrak{s}; \beta)\mathbf{G}(\mathfrak{s})\mathbf{Q}_\alpha(\tau)\mathbf{G}(\mathfrak{s})^T\boldsymbol{\Phi}^T(t_{k+1}, \mathfrak{s}; \beta)\,\mathrm{d}\mathfrak{s} \tag{79}$$

where, $\boldsymbol{\Phi}(t_{k+1}, \mathfrak{s}; \beta)$, the state transition matrix, is computed using numerical integration of the continuos time state matrix given in Eq. (78).

The success of this model lies on the successful determination of β and σ_m^2. Like previous models Q_α, by careful selection of β and σ_m^2, must be sized appropriately to represent SO maneuver capability. Since β is the inverse of τ, it is selected by matching τ to the length of the expected SO maneuver. It is important to note that when $\tau \neq 0$, the angular velocities are continuous in time, as they are in the true kinematic motion of the SO. In the special case where $\tau = 0$, the dynamics reduce to a white noise process model very similar to that proposed by Holzinger et al. [51].

Singer proposes modeling the variance of target acceleration as a ternary uniform distribution, where probabilities of success and failure of the maneuver are assigned. This work avoids assuming these unknown probabilities by modeling the variance in the acceleration as a uniform distribution having a maximum acceleration amplitude, $\alpha_{\max}$, as defined by Eq. (80).

$$\sigma_m^2 = \frac{\alpha_{\max}^2}{3} \tag{80}$$

Since $\alpha_{\max}$ will seldom be known, one has two primary methodologies for establishing this maximum value. The first is to pick values representative of the hypothesized SO class, where knowledge of SO size could come from auxiliary characterization. The second

methodology is to hypothesize multiple targets the SO could be tracking, and selecting the maximum acceleration of those hypotheses.

5.3 Rao-Blackwellized Particle Filter

While several correlation functions are available to model the dynamics of an agile SO, the exponentially correlated angular acceleration model is chosen purposefully. In Eq. (78), the Euler angles appear non-linearly in the dynamics and measurement models, while the angular velocity and angular acceleration states appear linearly in the dynamics. The linear structure of the angular velocity and acceleration states can be exploited to reduce the computational burden of a traditional Particle Filter (PF), by marginalizing out the linear state variables. These linear states can then be estimated using a Kalman filter (KF), which improves state estimates as it is the optimal estimator of these linear states. This concept is sometimes referred to as Rao-Blackwellization, and hence is referred to as a Rao-Blackwellized particle filter (RBPF).

The goal of a nonlinear non-Gaussian filter, like the RBPF, is to determine the posterior probability density function, $p(\mathbf{x}_k|\mathbf{Y}_k)$, recursively. The RBPF approach analytically marginalizes out the linear state by solving for the posterior probability density function (PDF) at time step k as

$$p(\mathbf{x}_k^n, \mathbf{x}_k^\ell|\mathbf{Y}_k) = \underbrace{p(\mathbf{x}_k^\ell|\mathbf{x}_k^n, \mathbf{Y}_k)}_{\text{KF}} \underbrace{p(\mathbf{x}_k^n|\mathbf{Y}_k)}_{\text{PF}} \tag{81}$$

where $p(\mathbf{x}_k^\ell|\mathbf{x}_k^n, \mathbf{Y}_k)$ is the marginalized posterior probability density for the linear states and can be optimally solved with the Kalman Filter. However, the marginalized posterior probability density for the non-linear states, $p(\mathbf{x}_k^n|\mathbf{Y}_k)$, has no closed-form solution and therefore it is approximated with a Particle Filter. The posterior for the linear portion of the state space is given by

$$p(\mathbf{x}_k^\ell|\mathbf{x}_k^n, \mathbf{Y}_k) = \mathcal{N}\left(\hat{\mathbf{x}}_k^\ell, \mathbf{P}_k\right) \tag{82}$$

where $\hat{\mathbf{x}}_k^n$ and $\mathbf{P}_k$ are the linear mean and covariance determined from a KF with the nonlinear states marginalized. Combining the KF posterior with the PF posterior gives the

overall state posterior PDF as

$$p(\mathbf{x}_k^n, \mathbf{x}_k^\ell | \mathbf{Y}_k) = \sum_{i=1}^{N} p(\mathbf{x}_k^\ell | \mathbf{x}_k^n(i), \mathbf{Y}_k) w_k^i \delta(\mathbf{x}_k^n - \mathbf{x}_k^n(i)) \tag{83}$$

note that this representation of the PDF can model both non-Gaussian PDFs in the linear and non-linear state. In this representation, the linear state are modeled using a Gaussian distribution, assuming the initial state is Gaussian, and the nonlinear state are modeled using a collection of weighted particles. This general outline of the RBPF can also found in Schon, while the specific algorithm utilized in this work is given by Algorithm 1[104].

Using the notation of Schon, the state space is segregated into a non-linear portion, $\mathbf{x}_k^n$, and a linear portion, $\mathbf{x}_k^\ell$, as illustrated in Eq. (84). This segregation leads to the system described by Eq. (85), where again it is noted the general form of the system has been replaced with one specific to the SO light curve inversion problem.

$$\mathbf{x}_k = \left[\begin{array}{c} \boldsymbol{\theta}_{\boldsymbol{I}}^{\boldsymbol{B}} \\ \hline \boldsymbol{\omega} \\ \boldsymbol{\alpha} \end{array}\right]_{t=t_k} = \left[\begin{array}{c} \mathbf{x}_k^n \\ \hline \mathbf{x}_k^\ell \end{array}\right] \tag{84}$$

$$\begin{aligned} \mathbf{x}_{k+1}^n &= \mathbf{F}_{n,k}^n(\mathbf{x}_k^n) \quad + \mathbf{A}_k^n(\mathbf{x}_k^n)\mathbf{x}_k^\ell + \mathbf{G}_k^n(\mathbf{x}_k^n)\mathbf{w}_k^n \\ \mathbf{x}_{k+1}^\ell &= \qquad\qquad \mathbf{A}_k^\ell(\mathbf{x}_k^n)\mathbf{x}_k^\ell + \mathbf{G}_k^\ell(\mathbf{x}_k^n)\mathbf{w}_k^\ell \\ y_k &= h_k^n(\mathbf{x}_k^n) \qquad\qquad + \mathbf{v}_k \end{aligned} \tag{85}$$

To further illustrate the relationship between the Rao-Blackwellized particle filter notation of Eq. (85) and the exponentially correlated dynamics defined in Eq. (78), let the following relationships be defined. In Eq. (86), $\boldsymbol{\Phi}$ is the state transition matrix $\boldsymbol{\Phi}(t_{k+1}, \mathfrak{s}; \beta)$ with inputs suppressed for brevity. The subscripts, eg. θ, indicate which rows and columns correspond of the state transition matrix correspond to the F matrix.

$$\mathbf{F} = \left[\begin{array}{c|c} \mathbf{F}_{n,k}^n(\mathbf{x}_k^n) & \mathbf{A}_k^n(\mathbf{x}_k^n) \\ \hline \mathbf{0}_{6x3} & \mathbf{A}_k^\ell(\mathbf{x}_k^n) \end{array}\right] = \left[\begin{array}{c|cc} \boldsymbol{\Phi}_{\theta,\theta} & \boldsymbol{\Phi}_{\theta,\omega} & \boldsymbol{\Phi}_{\theta,\alpha} \\ \hline \boldsymbol{\Phi}_{\omega,\theta} & \boldsymbol{\Phi}_{\omega,\omega} & \boldsymbol{\Phi}_{\omega,\alpha} \\ \boldsymbol{\Phi}_{\alpha,\theta} & \boldsymbol{\Phi}_{\alpha,\omega} & \boldsymbol{\Phi}_{\alpha,\alpha} \end{array}\right] \tag{86}$$

Algorithm 1: Rao-Blackwellized Particle Filter

$x_{k+1}^i = \text{RBPF}\left(x_k^i, z_k\right)$
1) Initialize Particles
2) PF Measurement Update, Eq. (89) - Eq. (90)
3) Evaluate PF Weights, Eq. (91)
4) PF Resampling
5) PF Time Update, Eq. (78)
6) KF Time Update, Eq. (92) - Eq. (98)

$$\left[\begin{array}{c} \mathbf{G}_k^n\left(\mathbf{x}_k^n\right) \\ \hline \mathbf{G}_k^\ell\left(\mathbf{x}_k^n\right) \end{array}\right] = \left[\begin{array}{c} \mathcal{I}_{3\times 3} \\ \hline \mathcal{I}_{3\times 3} \\ \\ \mathcal{I}_{3\times 3} \end{array}\right] \tag{87}$$

Additionally, the discrete time process noise can be sampled utilized the discrete time process noise covariance matrixes defined by Eq. (79).

$$\mathbf{w}_k \sim \mathcal{N}\left(\mathbf{0}, \mathbf{Q}_k(t_{k+1}, t_k, \mathbf{x})\right) \tag{88}$$

The general RBPF algorithm is the same as a traditional PF, except for the final step, which is the KF time update of the linear states. The RBPF algorithm begins by drawing random samples from an assumed distribution. One of the key advantages of both PF and RBPF over other non-linear sequential estimators, such as UKF, is that the distribution need not be Gaussian. Given sufficient computational power, it is possible that no a priori attitude is assumed. The next step, the PF update equation defined in Eq. (90), is used to calculate the likelihood of each particle, $\tilde{c}_k^i$, conditioned on the true measurement, y_k.

$$z_{1,k}^i = y_k - h_k^n\left(\mathbf{x}_k^{i,n}, t\right) \tag{89}$$

$$\tilde{c}_k^i = p\left(z_{1,k}|\mathbf{x}_k\right) = \frac{1}{\left(2\pi R_k(\mathbf{x}, t_I)\right)^2} \exp\left[-\frac{1}{2}\left(z_{1,k}^i R_k(\mathbf{x}, t_I)^{-1} z_{1,k}^i\right)\right] \tag{90}$$

These likelihoods are often referred to as the "importance weights" of each particle, and are used in the PF resampling algorithm after normalizing the weights according to Eq. (91). The fourth step, particle resampling, solves the much discussed shortcoming of the PF, which is sample impoverishment. This approach utilizes residual resampling, although other methods such as Metropolis or stratified resampling have been offered as equally effective

alternatives [105].

$$c_k^i = \frac{\tilde{c}_k^i}{\sum_{i=1}^{N} \tilde{c}_k^i} \tag{91}$$

The next step in the typical RBPF would be the KF measurement update to the linear portion of the state vector of each particle. However, examining Eq. (85) reveals that the measurement equation is a non-linear function of the body attitude only. As a result, the KF measurement update step is skipped and the next step is to propagate the non-linear particles to the next time step. The final step is the KF time update, where the innovation used is given by Eq. (85).

$$\mathbf{z}_{2,k}^i = \mathbf{x}_{k+1}^{i,n} - \mathbf{F}_{n,k}^n \left(\mathbf{x}_k^n\right) \tag{92}$$

This second "measurement", $\mathbf{z}_{2,k}^i$, incorporates the couple between the linear and nonlinear states and is the only means for information from the light curve measurement to be used to update the linear states. The linear KF propagation and update equations are given by [104]

$$\mathbf{x}_{k+1}^\ell = \bar{\mathbf{F}}_k^\ell \mathbf{x}_k^\ell + \mathbf{G}_k^\ell \left(\mathbf{Q}_k^{\ell n}\right)^T \left(\mathbf{G}_k^n \mathbf{Q}_k^n\right)^{-1} \mathbf{z}_{2,k}^i + \mathbf{L}_k \left(\mathbf{z}_{2,k}^i - \mathbf{F}_k^n \mathbf{x}_k^\ell\right) \tag{93}$$

$$\mathbf{P}_{k+1}^\ell = \bar{\mathbf{F}}_k^\ell \mathbf{P}_k^\ell \left(\bar{\mathbf{F}}_k^\ell\right)^T + \mathbf{G}_k^\ell \bar{\mathbf{Q}}_k^\ell \left(\mathbf{G}_k^\ell\right)^T - \mathbf{L}_k \mathbf{N}_k \mathbf{L}_k^T \tag{94}$$

where it is noted that some parameters have been dropped from the following equations to make them specific to the light curve inversion problem. The equations necessary for these computations are given by [104].

$$\mathbf{N}_k = \mathbf{F}_k^n \mathbf{P}_k^\ell \left(\mathbf{F}_k^n\right)^T + \mathbf{G}_k^n \mathbf{Q}_k^n \left(\mathbf{G}_k^n\right)^T \tag{95}$$

$$\mathbf{L}_k = \bar{\mathbf{F}}_k^\ell \mathbf{P}_k^\ell \left(\mathbf{F}_k^n\right)^T \mathbf{N}_k^{-1} \tag{96}$$

$$\bar{\mathbf{F}}_k^\ell = \mathbf{F}_k^\ell - \mathbf{G}_k^\ell \left(\mathbf{Q}_k^{\ell n}\right)^T \left(\mathbf{G}_k^n \mathbf{Q}_k^n\right)^{-1} \mathbf{F}_k^n \tag{97}$$

$$\bar{\mathbf{Q}}_k^\ell = \mathbf{Q}_k^\ell - \left(\mathbf{Q}_k^{\ell n}\right)^T \left(\mathbf{Q}_k^n\right)^{-1} \mathbf{Q}_k^{\ell n} \tag{98}$$

These equations complete the RBPF algorithm. The RBPF affords the estimation of both attitude and angular velocity states of maneuvering space objects without requiring knowledge of the initial orientation of the SO, while maintaining computational tractability. The next section highlights these benefits compared to previously developed particle filters.

5.4 Simulation Results

If the algorithms presented are to one day be used operationally, the simulation must match observational data as closely as possible. Accordingly, every effort is made to create a realistic physics based simulation, as outlined below.

5.4.1 Data Flow

The first component of this simulator is the Simplified General Perturbations Propagator (SGP4). This software calculates the position and velocity of a SO by propagating the information from a two line element (TLE) file. A MATLAB implementation is available from Vallado et. al. [106] The next piece of software critical to the simulator is the 1987 implementation of Variations Séculaires des Orbites Planétaires (VSOP87) [107]. The adaptation of VSOP87 by Bretagnon and Francou[108] combined with the coordinate transformations provided by Meeus [109] enables the ephemerides of the Sun and Earth to be calculated with less than 1" error until 6000 A.D. The geometry necessary to define the reflectance of light can be defined using the the position of the Sun, observer, and SO. This geometry is used in the final part of the simulator, a bidirectional reflectance distribution function (BRDF) model. This particular work utilizes the Cook-Torrance BRDF model for specular contributions [110], and Lambertian reflectance for diffuse contributions to the total radiant flux of the SO at various attitudes [51].

5.4.2 Test Cases

All test cases presented are derived from a two-line element set (TLE) for the NOAA 18 satellite downloaded from SpaceTrack.org [111]. Each TLE comprises two lines of 80-column ASCII text identifying the satellite by its catalog ID number and defining its orbital elements at the given epoch time. The simulation represents observations collected on June 6th, 2014 from 10:19:21 to 10:23:19 UTC from the Fenton Hill Observatory.

```
NOAA 18 [B]
1 28654U 05018A 15024.53745670 .00000182 00000-0 12433-3 0 4147
2 28654 99.1733 13.7659 0014261 7.4244 99.1613 14.12137281498803
```

The NOAA 18 spacecraft orbits at $a = 7226$ km, $e = 2.3 \times 10^{-3}$, $i = 99.2$ deg, $\Omega = 17.8$ deg, $\omega = 14.6$ deg, and $f = 114.8$ deg. The problem is simplified such that NOAA 18 is

represented by a simple cube, with the shape model parameters presented in Table 17. In

Table 13: Assumed Shape Model Parameters

Facet	A (m^2)	ξ	a	m
+X	2	0.5	0.25	0.3
+Y	2	0.5	0.5	0.3
+Z	2	0.5	0.75	0.3
-X	2	0.5	0.9	0.3
-Y	2	0.5	0.4	0.3
-Z	2	0.5	0.1	0.3

the shape model, A is the facet area, ξ is the affine transformation weighting parameter, a is the diffuse albedo, and m is the microfacet slope parameter where ξ, a, and m $\in [0,\ 1]$. Since previous work has addressed shape model uncertainty, this work assumes the shape model is known perfectly [51]. To simulate an agile SO, the problem is modeled such that the -Z facet of NOAA 18 is constrained to the line-of-sight vector from the spacecraft to Colorado Springs, CO for the duration of the pass. This results in the acceleration profile depicted in Fig. 15. This simulated mission results in the light curves presented in Fig. 16.

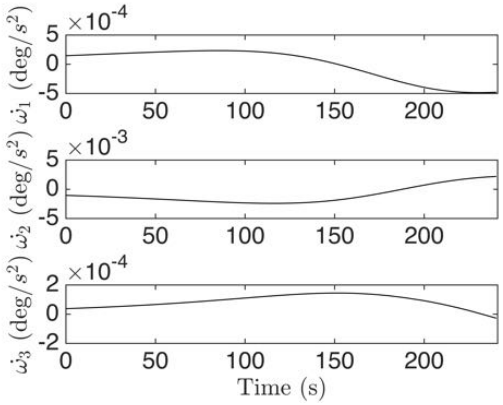

Figure 15: True Agile SO Acceleration

The telescope parameters utilized, shown in Table 14, are those of the 0.5 m f/8 GT-SORT telescope, and are representative of a typical Raven-class telescope [19].

Ideally, it would be desirable to introduce a separate test case for each improvement outlined in this paper. However, the inclusion of a comparison between the time invariant, limiting magnitude measurement model and the radiometric measurement model was

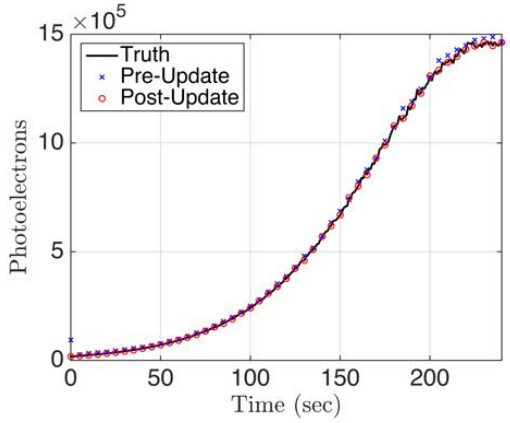

(a) TC1 Light Curve

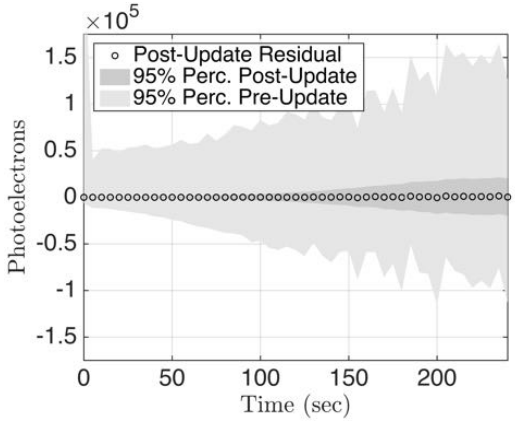

(b) TC1 Residual vs Time

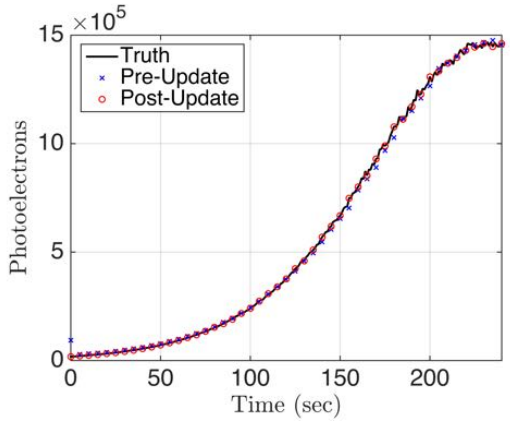

(c) TC2 Light Curve

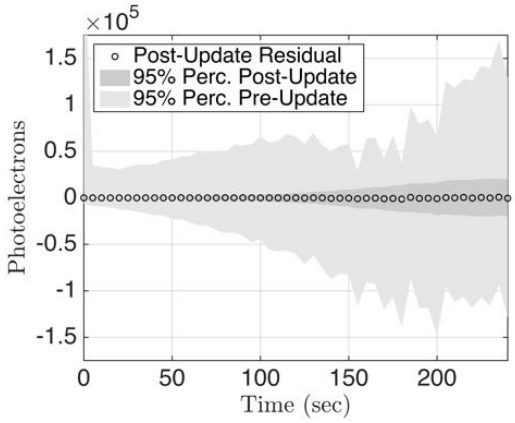

(d) TC2 Residual vs Time

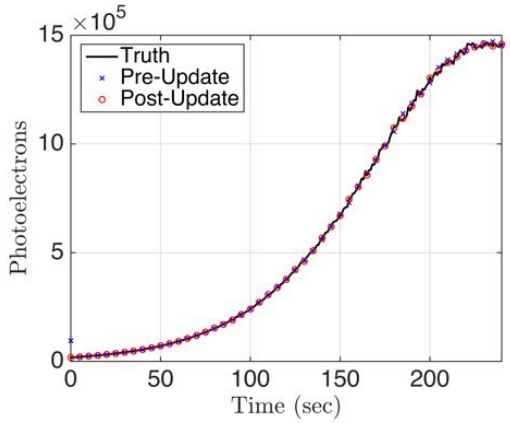

(e) TC3 Light Curve

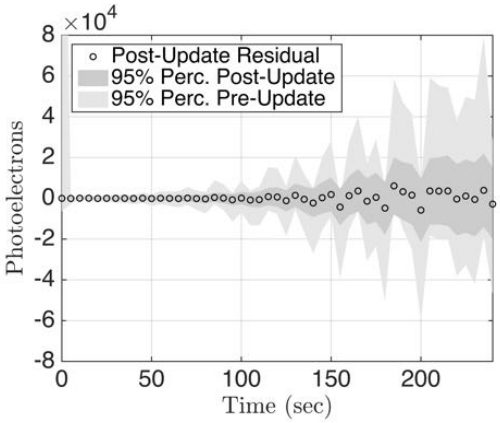

(f) TC3 Residual vs Time

Figure 16: Pre and Post Update Estimate of Light Curve

Table 14: Radiometric Model Parameters

Parameter	Value	Units
Telescope Aperture Diameter	.5	m
Effective Focal Length	8	-
Pixel Size	9e-6	m
Mean Atmospheric Transmittance	.6	-
Variance Atmospheric Transmittance	2.5e-5	-
Optical Transmittance	.7	-
Quantum Efficiency	.5	-
Radiant Sky Intensity	18	m_v/arcsec^2
Exposure Time	1	s
Dark Current	.5	e/pixel/s
Read Noise	10	e (RMS)
Pixels Occupied by SO	10	pixels
Pixel Sample Estimate Background Level	200	pixels

deemed trivial. Since the benefit afforded by each improvement is judged by its reduction in the error of estimated states, it seemed illogical to compare estimates arrived at using a measurement model that produced incorrect uncertainties. Additionally, it was computationally infeasible to include a comparison between the standard PF utilizing the ECA dynamics model and the RBPF. Indeed, computational tractability is one of the main benefits of the RBPF.

As a result, three test cases (TC) are implemented to demonstrate the improvements outlined in this paper over the current "state-of-the-art." TC1 represents one version of the current "state-of-the-art," using a PF and a white noise process for the unknown angular velocities. TC1 also implements the time-varying radiometric noise model, where the total photon count is given using Eq. (60). Importantly, TC1 does not assume any knowledge of the mean angular velocity states. In contrast, TC2 showcases the performance of the current state-of-the-art when knowledge of the mean angular velocities is introduced. While this improves the accuracy of tracking, as shown below, this information is unlikely to be available in an operational setting. Consequently, TC3, like TC1, does not assume any a priori knowledge of SO mean angular velocity. TC3 keeps the radiometric nose model, and adds the exponentially correlated acceleration (ECA) model, enabling the use of the RBPF.

All TC are presented utilizing the same number of particles: 10,000. Additionally, the

following levels of process noise were utilized to keep comparisons between the PF and RBPF consistent. For the PF, $Q_\omega(\tau) = \text{diag}\big(1^{-4} \cdot [0.0113,\ 0.7243,\ 0.0025]\big)\,\text{rad}^2/\text{sec}^2$. Meanwhile, the RBPF utilized $Q_\alpha(\tau) = \text{diag}\big(1^{-5} \cdot [0.0029,\ 0.1196,\ 0.0003]\big)\,\text{rad}^2/\text{sec}^2$ and $\beta_1 = \beta_2 = \beta_3 = 1/15$ with units of 1/sec. For an initial attitude of $\boldsymbol{\theta}_I^B = \mathbf{0}$ these settings resulted in 1σ noise levels of $\delta\boldsymbol{\omega}_0 = [0.061,\ .488,\ .029]^T$ deg/sec.

Table 15: Test Case Descriptions

Test Case	NL/L States	Measurement Model	Dynamics Model	$\boldsymbol{\omega}_\mu$	Filter
#1	3/0	Radiometric	White-Noise	$\mathbf{0}$	PF
#2	3/0	Radiometric	White-Noise	Truth	PF
#3	3/6	Radiometric	ECA	$\mathbf{0}$	RBPF

Fig. 17 through Fig. 20 illustrate the particle clouds of the three test cases at four instances during the simulation time. TC1 is always presented on the top row, while the middle and bottom rows are TC2 and TC3, respectively. The particles themselves are shaded such that the particles with the highest likelihoods, i.e. weights, are shown in black while particles that represent less likely states are represented with lighter shades of gray. In all subfigures, the true simulated state is shown with a red star.

Fig. 17 illustrates the initialized particles for all test cases. In all test cases, the particles are uniformly distributed in Euler angle space in a window around the true state. This is purely a constraint of the computational resources available to the authors. Given a high performance computer, both the PF and RBPF filters are capable of uniformly sampling the entire state space. Fig. 18 shows both filters 75 seconds into the simulation. One can see that the particles of the RBPF (TC3) are distributed in smaller volume of state space than either PF test case. Additionally, the large swaths of gray particles in TC1 and TC2 highlight that the RBPF is much more computationally efficient, with each resampled particle having a higher likelihood according to Eq. (90).

Fig. 19 shows both filters 155 seconds into the simulation, and is an excellent illustration of the highly non-Gaussian distributions typical of the SO attitude estimation problem. It is also evident by examining TC1 that without knowledge of the SO's mean angular velocity, the state of the art PF begins to diverge, with the true SO state no longer bounded by the

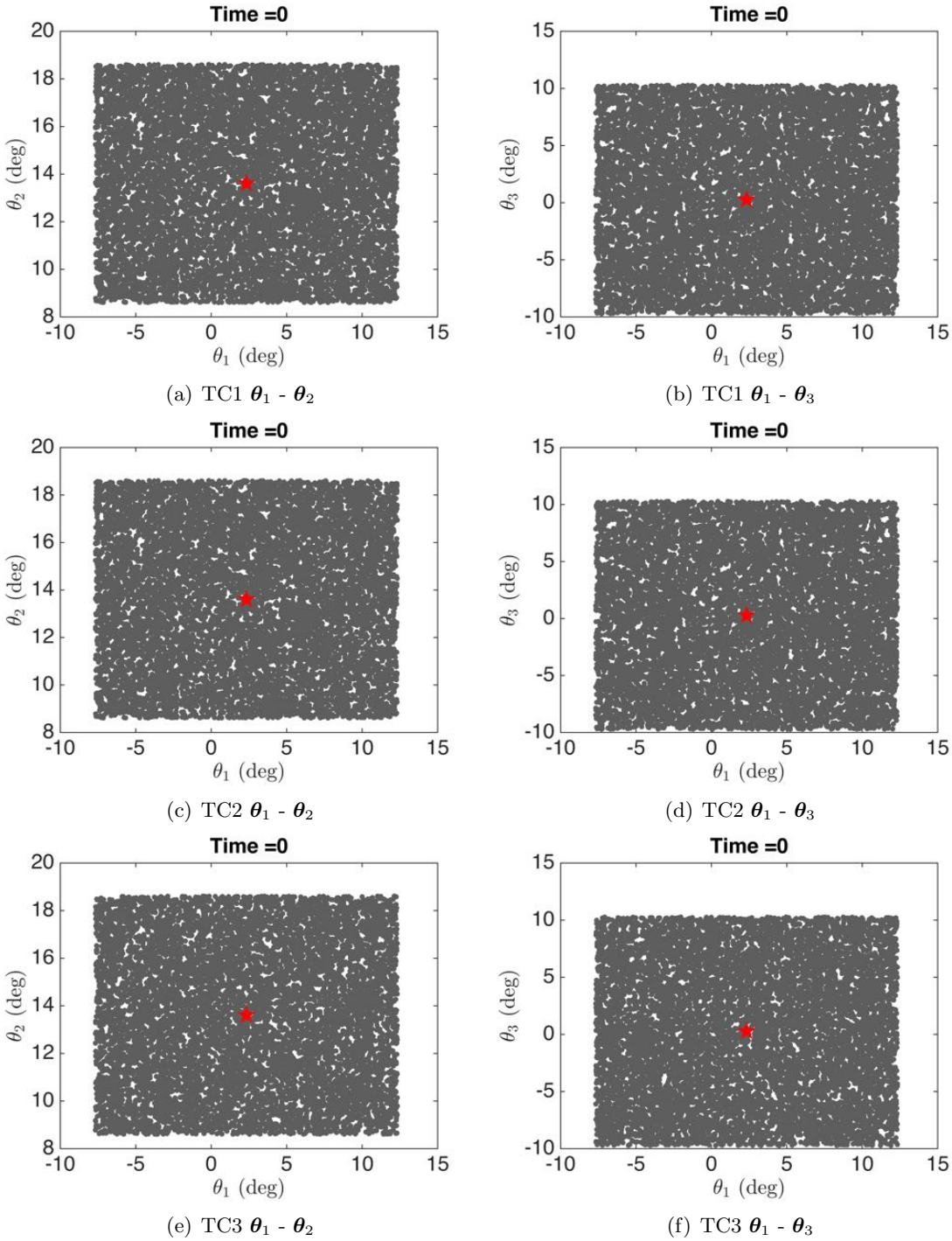

(a) TC1 $\boldsymbol{\theta}_1$ - $\boldsymbol{\theta}_2$

(b) TC1 $\boldsymbol{\theta}_1$ - $\boldsymbol{\theta}_3$

(c) TC2 $\boldsymbol{\theta}_1$ - $\boldsymbol{\theta}_2$

(d) TC2 $\boldsymbol{\theta}_1$ - $\boldsymbol{\theta}_3$

(e) TC3 $\boldsymbol{\theta}_1$ - $\boldsymbol{\theta}_2$

(f) TC3 $\boldsymbol{\theta}_1$ - $\boldsymbol{\theta}_3$

Figure 17: Test Cases at t=0 seconds

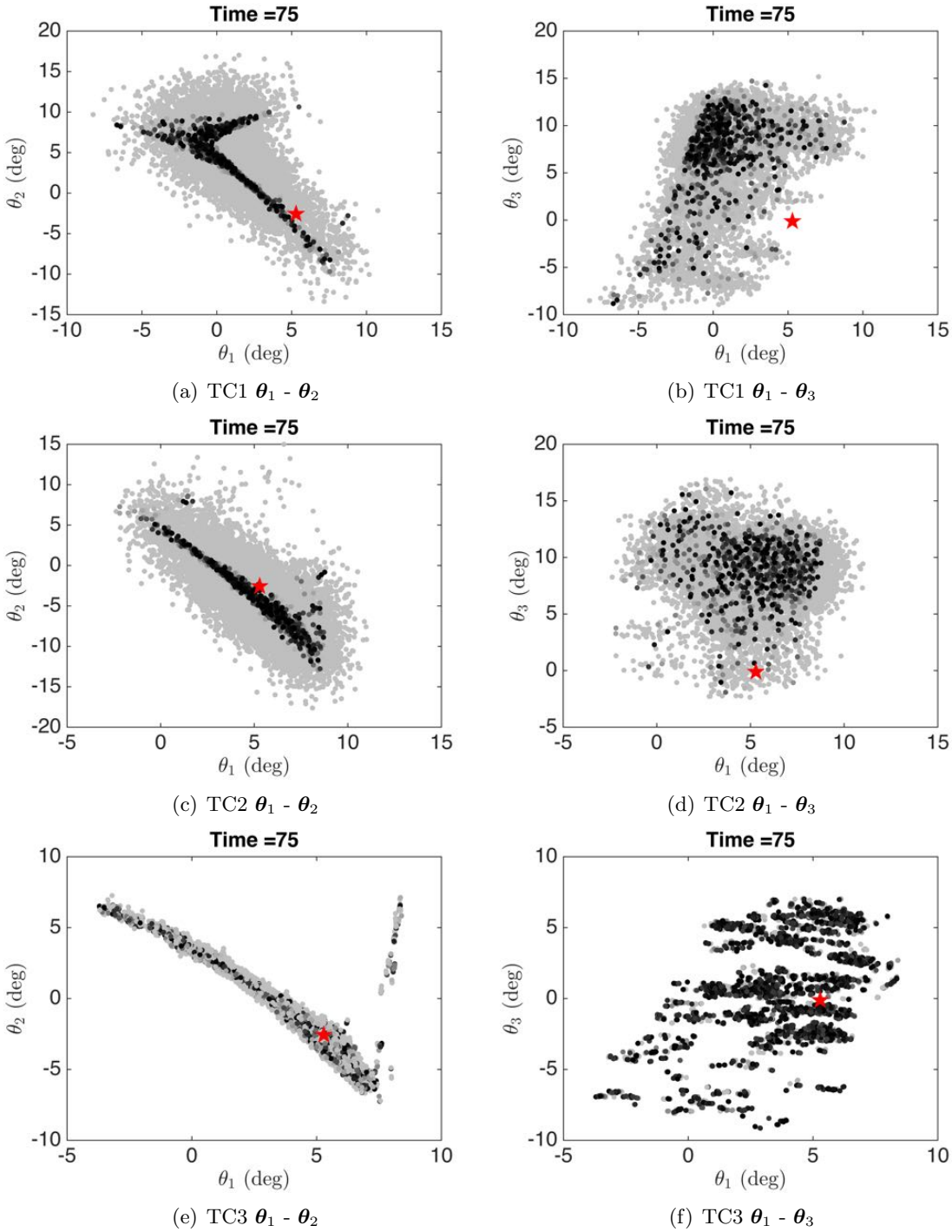

(a) TC1 $\boldsymbol{\theta}_1$ - $\boldsymbol{\theta}_2$

(b) TC1 $\boldsymbol{\theta}_1$ - $\boldsymbol{\theta}_3$

(c) TC2 $\boldsymbol{\theta}_1$ - $\boldsymbol{\theta}_2$

(d) TC2 $\boldsymbol{\theta}_1$ - $\boldsymbol{\theta}_3$

(e) TC3 $\boldsymbol{\theta}_1$ - $\boldsymbol{\theta}_2$

(f) TC3 $\boldsymbol{\theta}_1$ - $\boldsymbol{\theta}_3$

Figure 18: Test Cases at t=75 seconds

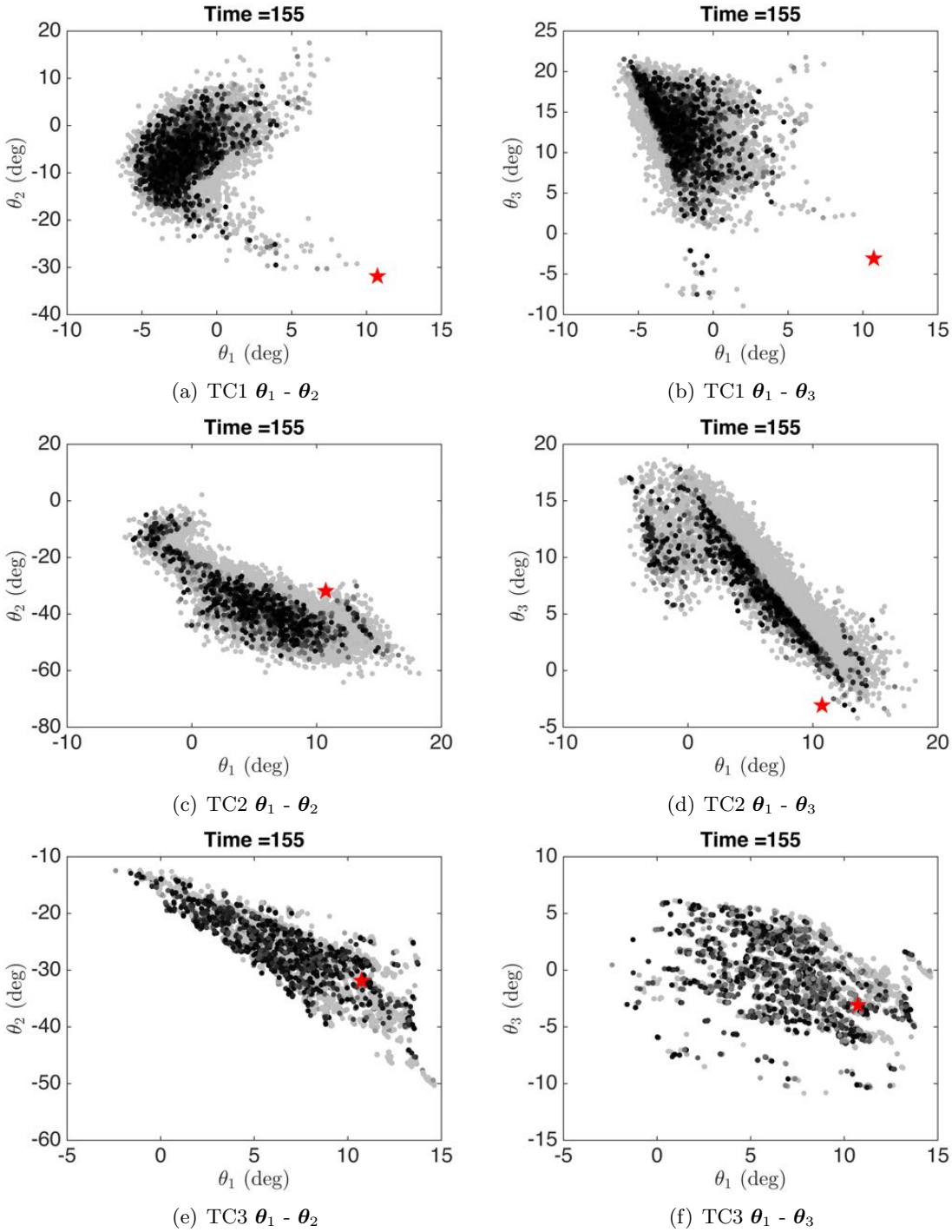

(a) TC1 $\boldsymbol{\theta}_1$ - $\boldsymbol{\theta}_2$

(b) TC1 $\boldsymbol{\theta}_1$ - $\boldsymbol{\theta}_3$

(c) TC2 $\boldsymbol{\theta}_1$ - $\boldsymbol{\theta}_2$

(d) TC2 $\boldsymbol{\theta}_1$ - $\boldsymbol{\theta}_3$

(e) TC3 $\boldsymbol{\theta}_1$ - $\boldsymbol{\theta}_2$

(f) TC3 $\boldsymbol{\theta}_1$ - $\boldsymbol{\theta}_3$

Figure 19: Test Cases at t=155 seconds

particle cloud. Fig. 20 shows all test cases at the final time step in the simulation, at 240 seconds. Only in TC2 and TC3 is the SO successfully tracked, with the true state contained within the particle cloud. The left hand side of Fig. 21 shows the true SO attitude, denoted by the solid black line, compared to the first moment of the particle cloud, shown by black circles, along with the 5 and 95 percentile bounds of the particle cloud illustrated by the shaded gray area. The right hand side of Fig. 21 shows the residuals of the attitude state, denoted by black 'X', along with the 5 and 95 percentile residual bounds.

The percentile bounds grow as observations of the SO are collected due to the interaction between the measurement noise and process noise. The observing environment described in Table 14 is shot-noise limited and in this anecdotal example the SO being observed becomes brighter with time, as shown in the left hand subfigures of Fig. 16. Consequently, the shot noise increases the measurement noise during the simulation, as defined in Eq. (29). This increase in measurement noise causes more particles around the truth to represent brightness values consistent with the measurement statistics. As a result, particles which have been randomly subjected to higher levels of process noise are not eliminated, and the cloud of particles grows as the simulation progresses.

Through the contributions of this work, illustrated in TC3, the angular velocity states are able to be simultaneously estimated. Fig. 22(b) gives the body angular velocities provided by the KF update portion of the RBPF. The estimation error is given by the solid black line, while the 5 and 95 percentile bounds are given by the shaded gray area. The ability of the RBPF to provide angular velocity estimates, via the adoption of the Singer dynamics mode, is a novel improvement to the SO attitude estimation problem.

The first benefit of this ability is that knowledge of SO body angular velocity can be used to better estimate the attitude states via the KF update step of the RBPF. This benefit is evident in the preceding figures, where the volume of state space occupied by the particle cloud is less for the RBPF than the PF. The second benefit afforded by knowledge of SO angular velocities manifests itself in SO operational mode classification. While determining the current attitude of a SO is a critical aspect of characterization, it is not an immediately actionable piece of information. Indeed, SSA stakeholders desire information on the

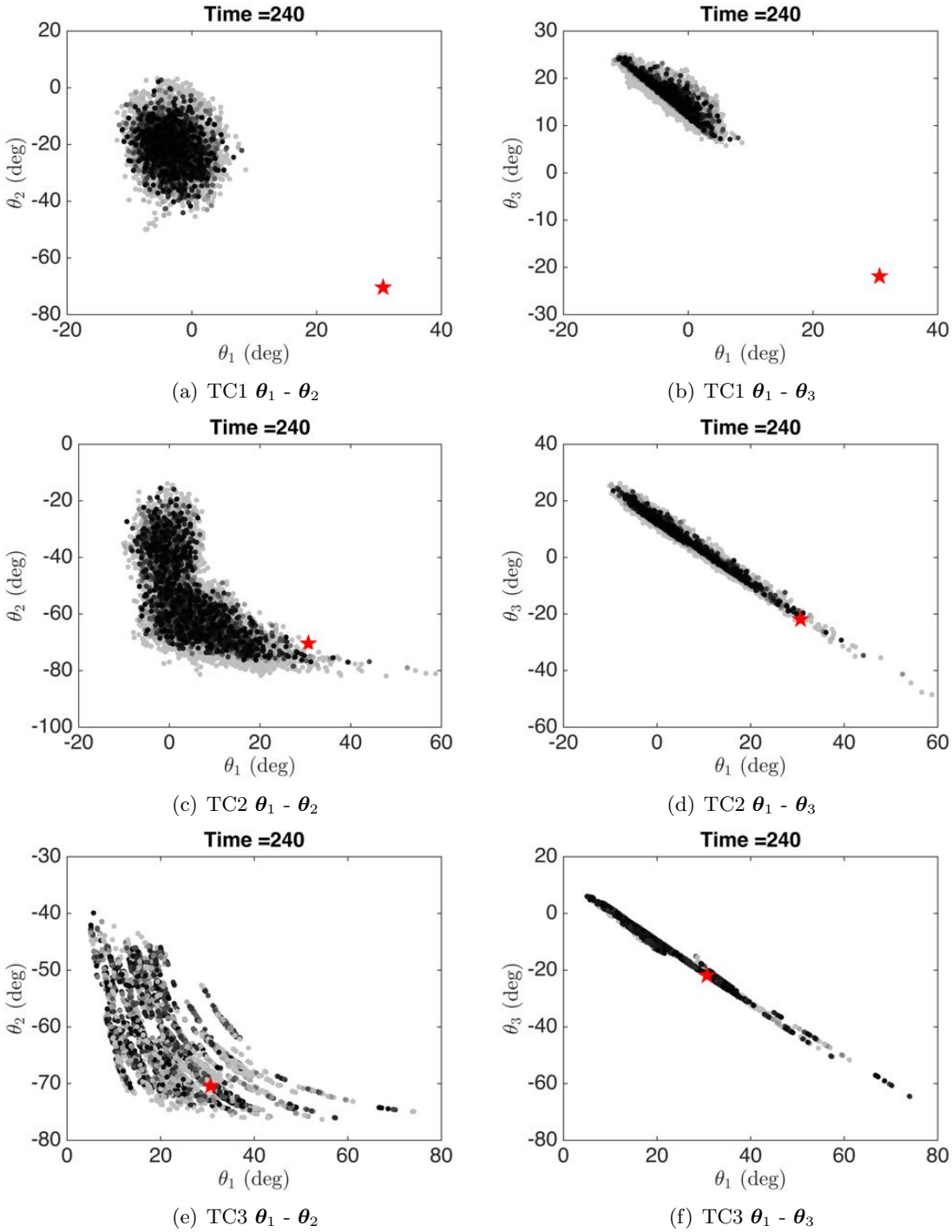

(a) TC1 $\boldsymbol{\theta}_1$ - $\boldsymbol{\theta}_2$

(b) TC1 $\boldsymbol{\theta}_1$ - $\boldsymbol{\theta}_3$

(c) TC2 $\boldsymbol{\theta}_1$ - $\boldsymbol{\theta}_2$

(d) TC2 $\boldsymbol{\theta}_1$ - $\boldsymbol{\theta}_3$

(e) TC3 $\boldsymbol{\theta}_1$ - $\boldsymbol{\theta}_2$

(f) TC3 $\boldsymbol{\theta}_1$ - $\boldsymbol{\theta}_3$

Figure 20: Test Cases at t=240 seconds

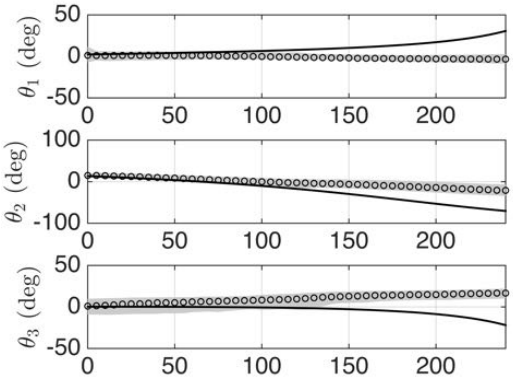

(a) TC1 Attitude Estimates

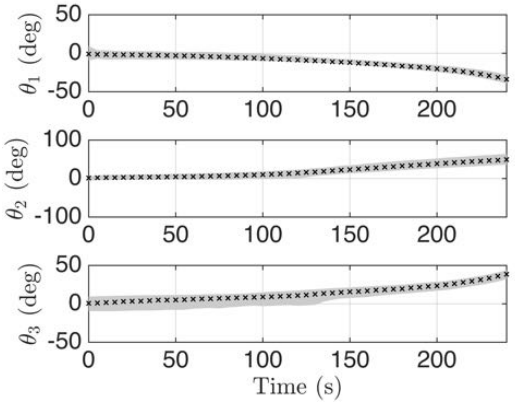

(b) TC1 Attitude Residuals

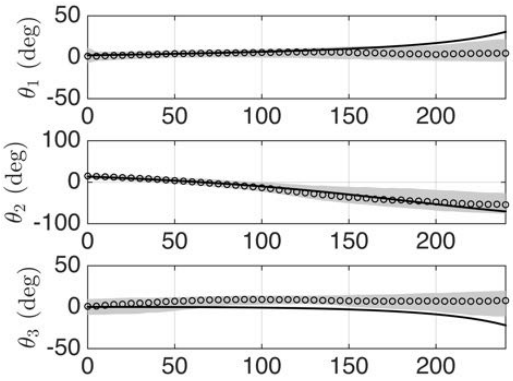

(c) TC2 Attitude Estimates

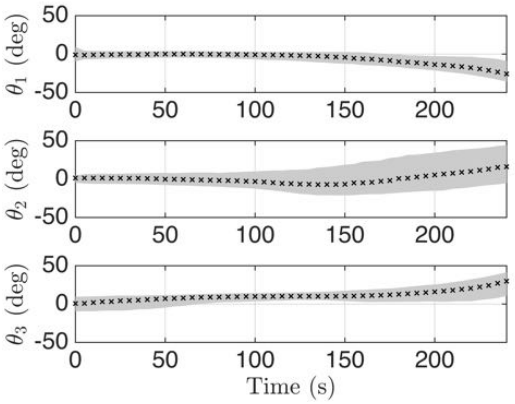

(d) TC2 Attitude Residuals

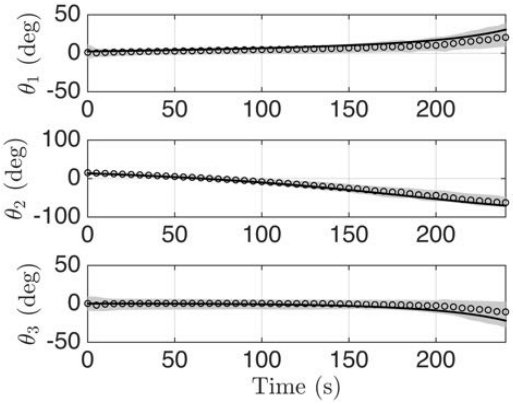

(e) TC3Attitude Estimates

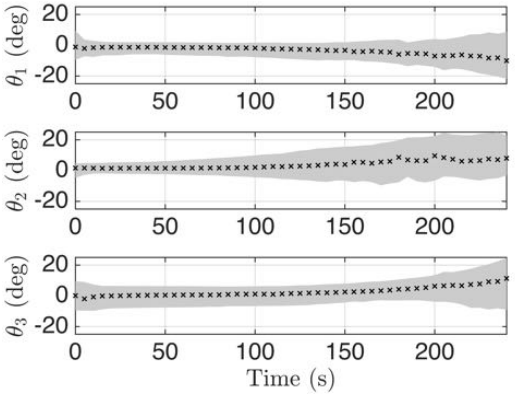

(f) TC3 Attitude Residuals

Figure 21: Comparison of Attitude Estimates for all Test Cases

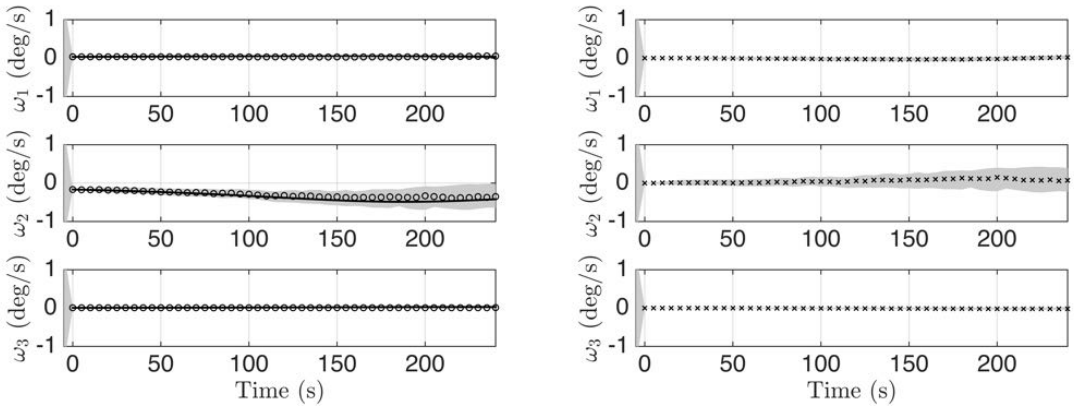

(a) Angular Velocity Estimates

(b) Estimation Error with 3σ bounds

Figure 22: RBPF Estimate of Angular Velocity

operational mode of a SO, e.g. if the SO is currently Sun-pointing, nadir-pointing, or tracking another SO. Information on SO angular velocity could be an important discriminator in operational mode classification if multiple operational classifications are represented by similar SO attitude states alone.

5.5 Summary

Physics based measurement models can be utilized to more closely reflect measurement noise present in observational data. The implementation of a correlated angular rate dynamics model, adapted from the Singer Markov process model, provided a framework for defining a space object maneuver model. This dynamics model enables the implementation of marginalized particle filters, enabling estimation of attitude and angular velocity states of maneuvering space objects without a prior knowledge of initial attitude, while maintaining computational tractability. These three contributions enhance the quality of information gleaned from scarce observation assets and further improve the state estimation of agile space objects. The increased knowledge afforded by these methods directly aids space object characterization and the overall mission of Space Domain Awareness.

CHAPTER VI

ACTIVE CONTROL MODE INFERENCE

6.1 Methodology

Chapter 5 outlined the light curve inversion approach developed for agile SO. This chapter presents several inference techniques for determining the most likely subject under observation by an agile SO. To give context to these contributions, It is prudent to discuss the spectrum of SO characterization. Consider Fig. 23 below, which proposes three general levels of SO classification. The general concept conveyed by Fig. 23 is that as information is gathered on a SO, further characterization is enabled.

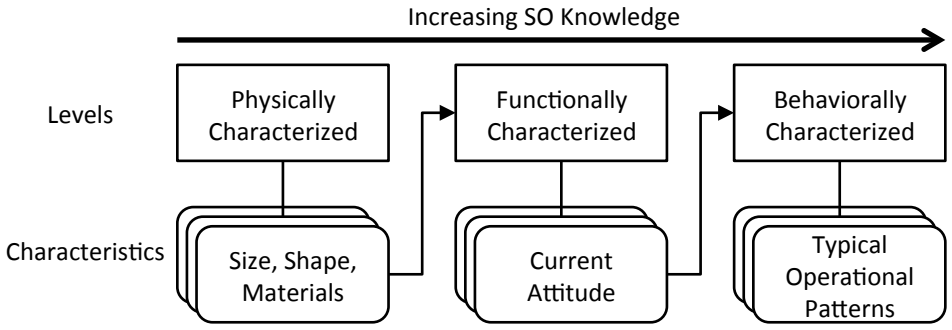

Figure 23: Increasing Knowledge of Agile SO Enable Refined Characterization

The most basic characteristics of SO, such as size or shape, could be estimated with no a priori information available [112]. Typically, the characteristics determined are intrinsic properties of the SO, and therefore this level constitutes a physical characterization. Determining the shape model enables light curve inversion techniques, affording estimates of current SO attitude or enabling inference on SO active control mode. Therefore, this information constitutes a functional description of current SO activity. While methods for determining shape independent attitude of non-agile SO have been presented [28], the current work focuses on agile SO. Finally, if these activities are aggregated over time, further inference could help establish routine operational patters or indicate payload capability of

the SO.

The contributions of this work best fit under the "functional characterization" block of Fig. 23. Subsection 6.1.1 and Subsection 6.1.2 outline metrics which utilize the estimated states directly to infer the active control mode of the SO. Subsection 6.1.3 couples statistical inference techniques with angular momentum and rotational kinetic energy analogs to establish formal hypothesis testing techniques. Finally, Subsection 6.1.4 outlines how radiometric first principles can bound the allowable tracking error between the target and subject SO.

6.1.1 Inference Using Attitude States

As illustrated in Fig. 24, $\boldsymbol{\rho}_{ij}$ defines the line-of-sight (LOS) vector from the SO to a hypothesized target, and $\hat{\rho}_b$ defines the vector along the SO bore-sight calculated from the estimated attitude angles. The simplest technique to infer SO active control mode is to determine the smallest angle between the estimated attitude states and each hypothesized attitude triple. The instantaneous angle between two unit vectors, $\hat{\boldsymbol{\rho}}_b$ and $\hat{\boldsymbol{\rho}}_{ij}$, is determined from the definition of the cross product as shown in Eq. (99).

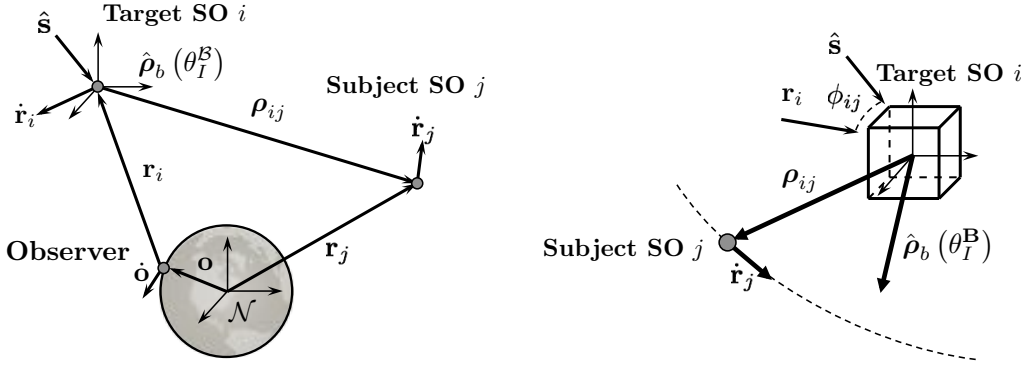

(a) Observer, Target SO, and Subject SO Geometry

(b) Instantaneous Angle Between Target Sensor Bore-axis and Subject SO

Figure 24: Problem Geometry and Instantaneous Angle Illustration

$$\Delta\theta_{a,b}\left(t\right) = 2\arcsin\left(\frac{\|\hat{\boldsymbol{\rho}}_b(t) - \hat{\boldsymbol{\rho}}_{ij}(t)\|}{2}\right) \tag{99}$$

Intuitively, the most likely subject of observation for the target SO at any instant in time is the hypothesis with the smallest instantaneous angle. However, for very cluttered regions

of space, such as those regions near to the poles, it is the case that many hypothesized SOs have small instantaneous angles.

To address this problem, this work adopts a measurement arc dissimilarity metric (MDM) developed for a match filtering technique for detecting SOs in low signal-to-noise ratio imagery [62]. To classify the active control mode of the SO, one desires the dissimilarity in the measurement arcs over the entire observation window $t \in [t_k - T,\ t_k]$. For ease of interpretation, one can define the mean MDM as given by Eq. (100) .

$$\bar{d}_{\mathrm{MD}} = \frac{1}{T} \int_{t_k - T}^{t_k} \Delta\theta_{a,b}\left(\tau\right) \mathrm{d}\tau \tag{100}$$

Because the bidirectional reflectivity distribution function (BRDF) measurement models of SO are non-linear functions of attitude states, non-Gaussian state distributions frequently arise. Commonly, the particle cloud grows to define a multi-modal distribution representing the symmetry commonly exhibited by man-made satellites. For example, if a satellite shaped as a cube has roughly the same material properties on each side, the RBPF correctly exhibits distinct clusters of particles. As shown in Fig. 34, it is common for the mean attitude state, represented by the black 'X', to lie outside the actual particle cloud. To more closely align the vectors $\hat{\boldsymbol{\rho}}_{ij}$ and $\hat{\boldsymbol{\rho}}_b$, k-means clustering is utilized to identify the number of distinct clusters in the particle cloud.

In traditional k-means, as developed by Lloyd, an arbitrary number of data samples, in this case particles of a PF, are assigned to c clusters where the number c is selected by the analyst [113]. While the methodologies presented in this work were not developed specifically with automation in mind, the more sophisticated k++ means algorithm, such as implemented in MATLAB®, do not require a priori specification of c [114]. Additionally, there is no theoretical reason why other clustering or fuzzy logic routines would be less appropriate for the task at hand. Moreover, it may serve as motivation for the implementation of a Rao-Blackwellized unscented Kalman filter, as discussed in the previous section.

Fig. 25 illustrates an instantiation of the attitude states at a single time step that resulted in two distinct clouds, shaded lighter and darker gray respectively. Since each particle has an associated weight, it is possible to identify the most likely cluster of particles.

The centroid of that cluster is then taken as $\hat{\rho}_b$, shown as a open circle in Fig. 25.

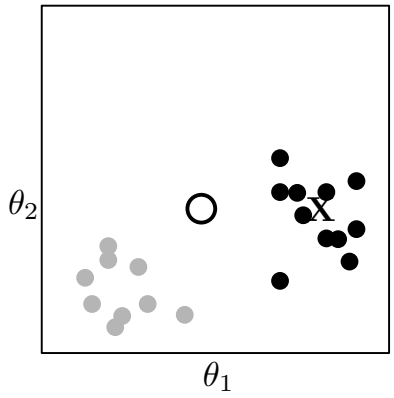

Figure 25: 2D View of Attitude States Sorted Via k-means

If the target SO has a continuous attitude rate over the entire observation window, the correct hypothesis is described by the lowest magnitude MDM. This will not be the case if the target SO exhibits discrete changes in attitude during the observation window. It is also possible that hypotheses with different orbits appear to be closely oriented in space from the perspective of the target SO. As an intuitive approach to disambiguate these important cases, one could examine the time derivative of the instantaneous angle defined by Eq. (99) to provide more information.

$$\frac{\mathrm{d}}{\mathrm{d}t}\left(\Delta\theta_{a,b}\left(t\right)\right) = \frac{\delta}{\delta t}\left(2\arcsin\left(\frac{\|\hat{\boldsymbol{\rho}}_b(t) - \hat{\boldsymbol{\rho}}_{ij}(t)\|}{2}\right)\right) \tag{101}$$

For ease of implementing the chain rule, let $u = \frac{1}{2}\|\hat{\boldsymbol{\rho}}_b(t) - \hat{\boldsymbol{\rho}}_{ij}(t)\|$ such that $u \in [0,1]$. Applying the chain rule to Eq. 101 yields Eq. 102.

$$\frac{\mathrm{d}}{\mathrm{d}t}\left(\Delta\theta_{a,b}\left(t\right)\right) = 2\left(\frac{\delta}{\delta u}\left(\arcsin\left(u\right)\right)\right)\left(\frac{\mathrm{d}u}{\mathrm{d}t}\right) \tag{102}$$

Solving the partial derivative yields Eq. 103.

$$\frac{\mathrm{d}}{\mathrm{d}t}\left(\Delta\theta_{a,b}\left(t\right)\right) = 2\left(\frac{1}{\sqrt{1-u^2}}\right)\left(\frac{\mathrm{d}u}{\mathrm{d}t}\right) \tag{103}$$

Examining the total time derivative of u from Eq. 103 yields Eq. 104.

$$\left(\frac{\mathrm{d}u}{\mathrm{d}t}\right) = \frac{1}{2}\left(\frac{\mathrm{d}}{\mathrm{d}t}\|\hat{\boldsymbol{\rho}}_b(t) - \hat{\boldsymbol{\rho}}_{ij}(t)\|\right) \tag{104}$$

To again apply the chain rule define the vector quantity $\xi = \hat{\boldsymbol{\rho}}_b(t) - \hat{\boldsymbol{\rho}}_{ij}(t)$. Using the identity for the derivative of the 2-norm, shown in Eq. 105, yields Eq. 106.

$$\frac{\delta}{\delta\xi}\|\xi\|_2 = \frac{\xi}{\|\xi\|_2} \tag{105}$$

$$\left(\frac{\mathrm{d}u}{\mathrm{d}t}\right) = \frac{1}{2}\frac{\xi}{\|\xi\|_2}\frac{\mathrm{d}\xi}{\mathrm{d}t} \tag{106}$$

The final derivative to be evaluated has previously been previously derived, as shown in Eq. 107 [115].

$$\frac{\mathrm{d}\hat{\boldsymbol{\rho}}_{ij}(t)}{\mathrm{d}t} = \frac{1}{\|\hat{\boldsymbol{\rho}}_b\|}\left[\mathcal{I} - \frac{\hat{\boldsymbol{\rho}}_b\hat{\boldsymbol{\rho}}_b^T}{\hat{\boldsymbol{\rho}}_b^T\hat{\boldsymbol{\rho}}_b}\right](\dot{\mathbf{r}}_j - \dot{\mathbf{r}}_i) + \boldsymbol{\omega}_{\mathcal{N}}^{\mathcal{B}} \times \left[\frac{\mathbf{r}_j - \mathbf{r}_i}{\|\mathbf{r}_j - \mathbf{r}_i\|}\right] \tag{107}$$

Examining Eq. 107 reveals that there are two main contributing factors to the change in angle between the target SO sensor bore-sight and the subject SO. The first term on the right hand side of Eq. 107 is simply dependent on the inherent motion of the target and subject SO. The second term describes the component of angle change that is dependent on the rotational motion of the agile SO, $\boldsymbol{\omega}_{\mathcal{N}}^{\mathcal{B}}$. Fortuitously, the RBPF previously developed by the authors and their colleagues enable estimation of the body angular velocities of the target SO, $\boldsymbol{\omega}_{\mathcal{N}}^{\mathcal{B}}$, to discriminate between subjects which are colocated along the target SO bore-sight, $\hat{\boldsymbol{\rho}}_b(t)$. Therefore, the remaining techniques in this work seek to quantify the "pointing quality" using the estimated posterior body angular velocity distributions of the target SO. If it is found that the body angular velocity of the target SO matches a profile necessary to rate track a specific subject SO, the observer may infer intentional action by the target SO.

6.1.2 Ranking Hypotheses using Mahalanobis Distance

The most general expression for the inner-product distance between two vectors, $\mathbf{a}$ and $\mathbf{b}$, is given by

$$d(\mathbf{a},\mathbf{b})^2 = (\mathbf{a}-\mathbf{b})^T\mathbf{A}^{-1}(\mathbf{a}-\mathbf{b}) \tag{108}$$

Here, the distance matrix $\mathbf{A}$ is positive semi-definite. When $\mathbf{A} = \mathcal{I}$ the Euclidean distance formula is recovered, while setting it equal to the covariance matrix of a Gaussian distributions $\mathbf{A} = \mathbf{P}$ yields the Mahalanobis distance.

The particle cloud representing the body angular velocity states can be expressed as a Multivariate Gaussian Mixture Model (MGMM). Generally speaking, an MGMM expresses a probability density function as a weighted sum of $i = 1 \dots N$ Gaussian component densities, as shown in Eq. (109).

$$p\left(\mathbf{x}_k^\ell\right) = w_i \sum_{i=1}^{N} f\left(\mathbf{x}\right) \tag{109}$$

Here, w_i is referred to as a "weight" or "likelihood" in the estimation literature. The RBPF represents the distribution with N "particles," as they are referred to in the estimation literature, or as "component densities" in the statistics literature. Each component density is a p-variate Gaussian function of the form

$$f\left(\mathbf{x}\right) = \mathcal{N}\left(\mathbf{x}_k^\ell |\ \boldsymbol{\omega}_{\mu,i}, \mathbf{P}_i\right) \tag{110}$$

To evaluate the distance of Multivariate Gaussian Mixture Models (MGMMs), alternative expressions for the covariance matrix is required. Previous work has advocated for a Gaussian mixture distance function based on minimizing the Kullback-Leibler divergence [116]. Minimizing the KL divergence for a Gaussian mixture yields the distance matrix given by Eq. (111).

$$\mathbf{A}\left(\mathbf{x}\right) = \left[\left(\sum_{i=1}^{n} w_i f\left(\mathbf{x}\right) \mathbf{P}_i\right)^{-1} \left(\sum_{j=1}^{n} w_j\left(\mathbf{x}\right) \mathbf{P}_j\right)\right]^{-1} \tag{111}$$

Here, $\mathbf{A}\left(\mathbf{x}\right)$ is the weighted reciprocal sum of the component covariances, and the weights are those given by the RBPF. To express the Mahalanobis distance for an MGMM, one also must define the mean of the MGMM. The mean of a MGMM is given simply by the weighted sum of all components

$$\boldsymbol{\omega}_\mu = \sum_{i=1}^{n} w_i \boldsymbol{\omega}_{\mu,i} \tag{112}$$

Substituting both Eq. (111) and Eq. (112) into Eq. (108) yields the Mahalanobis Distance analog for a MGMM. In this work, the Mahalanobis Distance analog is evaluated for each hypothesized subject, $h = [1, \dots, M]$ at each time interval, such that

$$d_{\mathrm{GM}} = \sqrt{\left(\boldsymbol{\omega}_{h,k} - \boldsymbol{\omega}_{\mu,k}\right)^T \mathbf{A}^{-1} \left(\boldsymbol{\omega}_{h,k} - \boldsymbol{\omega}_{\mu,k}\right)} \tag{113}$$

where $\boldsymbol{\omega}_{h,k}$ is the body angular velocity triple for each hypothesis, $H_{h,k}$, at each time step, t_k. The Mahalanobis distance can then be computed for each hypothesis at each time step, where the hypothesis with the lowest value of Mahalanobis distance indicates the most likely hypothesis.

Algorithm 1: Rank Hypotheses using Mahalanobis Distance

```
function rank MD (ω_{μ,k}, ω_{h,k}, A(x));
Input  : ω_{μ,k}, ω_{h,k}, A(x)
Output: flag
For each time step;
for k ← 1 to T do
    For each hypothesis i;
    for h ← 1 to M do
        Evaluate Mahalanobis Distance, Eq. (113);
        d_GM(h,k) = sqrt((ω_{h,k} − ω_{μ,k})^T A^{-1} (ω_{h,k} − ω_{μ,k}));
    end
end
```

6.1.3 Rotational Angular Momentum and Kinetic Energy Analog Inference

First principles tells us that the momentum and energy states of a SO are conserved quantities, unless acted upon by an outside force [50]. Therefore, changes in either angular momentum or angular kinetic energy could serve as a basic indication of active control mode. Because the SO inertia is typically unknown, but constant in the body fixed frame, this work proposes analogs for the angular momentum and angular kinetic energy as given by Eq. (115) and Eq. (117).

$$\mathbf{H} = \mathbf{J}\boldsymbol{\omega} \tag{114}$$

$$J_H = \boldsymbol{\omega} \tag{115}$$

$$E = \frac{1}{2}\boldsymbol{\omega}^T\mathbf{J}\boldsymbol{\omega} \tag{116}$$

$$J_E = \boldsymbol{\omega}^T\boldsymbol{\omega} \tag{117}$$

As before, $\mathbf{J}$ is the unknown inertia matrix and $\boldsymbol{\omega}$ is the body angular velocity, both of the target SO. Here, J_H is the angular momentum analog, which is a rotated and skewed version of the true angular momentum. J_E is the rotational kinetic energy analog, which

is simply proportional to and monotonic with the true rotational kinetic energy. These definitions imply that J_H is defined as an MGMM and J_E is defined as an MGMM analog of the chi-squared distribution with 3 degrees of freedom.

$$J_H = w_i \sum_{i=1}^{N} \mathcal{N}\left(\mathbf{x}_k^{\ell} |\ \boldsymbol{\omega}_{\mu,i}, \mathbf{P}_i\right) \tag{118}$$

$$J_E = \left[w_i \sum_{i=1}^{N} \mathcal{N}\left(\mathbf{x}_k^{\ell} |\ \boldsymbol{\omega}_{\mu,i}, \mathbf{P}_i\right)\right]^T \left[w_i \sum_{i=1}^{N} \mathcal{N}\left(\mathbf{x}_k^{\ell} |\ \boldsymbol{\omega}_{\mu,i}, \mathbf{P}_i\right)\right] \tag{119}$$

Unfortunately, this lack of knowledge about the SO inertia tensor implies that the momentum analog vector and energy analog are not guaranteed to be constant under torque-free motion. This follows from the analytic relationships for angular momentum and energy derived for both axisymmetric and asymmetric rigid bodies. These are both important cases, as spin-stabilized satellites are likely axisymmetric, with rotation occurring about a principle axis, and debris objects are likely asymmetric. From a geometric standpoint, the angular velocity vector is constrained to lie on the intersection of the angular momentum ellipsoid and the kinetic energy ellipsoid. The path defined by this intersection is called the "polhode," and defines the curve of the angular velocity vector as seen from the body-fixed frame. Assuming ideal rigid bodies with no internal energy dissipation, the true angular momentum and rotational kinetic energy are conserved, and the polhode forms a closed path [117].

Thus, the body angular velocities can change with time, not only under active control, but also under general torque-free motion. This implies that a changing angular momentum or energy analog is not proof of an actively controlled satellite. One important distinction between these two cases is that the magnitude of the body angular velocity vector, and hence magnitude of the angular momentum analog, is constant under torque-free motion for axisymmetric rigid bodies only.

By using the outputs of the RBPF to build momentum and energy distributions, statistical tests can be used to determine the active control mode of an agile SO. Generally these tests could provide evidence of the following behaviors: whether the SO is actively maneuvering during the observed period, what subject a target SO is observing, and whether the

active control mode of the target SO changes between any two arbitrary points in time. Consequently, the authors propose using multi-variate hypothesis tests to match the estimated SO momentum or energy analog with momentum or energy profiles for each hypothesized subject SO.

To briefly review, a hypothesis is a claim about a certain statistical parameter, where the union of the null hypothesis H_0 and alternative hypothesis H_1 comprise the entire domain of the parameter. Of these two, the null hypothesis is the "status-quo" and the alternative hypothesis is the new hypothesis being tested. To demonstrate the use of the momentum analog a two-sided hypothesis test is implemented [81]. Dropping the time step k notation, the form of the hypothesis given by Eq. (120).

$$H_0 : J_H = J_{H,h} \text{ vs. } H_1 : J_H \neq J_{H,h} \tag{120}$$

This form is chosen since it is irrelevant whether the angular momentum profile of the target SO is larger or smaller than any chosen hypothesized momentum profile. The goal is simply to determine which hypotheses are statistically equivalent to the estimated values. The statistical hypothesis test for the equality of two means requires that the two distributions are Gaussian. To test the mean vector of a multivariate Gaussian distribution the relevant test statistic is T^2, also referred to as Hottelling's T^2 in the social sciences [118].

$$T^2 = N(\boldsymbol{\omega}_{\mu,k} - \boldsymbol{\omega}_{h,k})^T \mathbf{A}\,(\mathbf{x})^{-1}(\boldsymbol{\omega}_{\mu,k} - \boldsymbol{\omega}_{h,k}) \tag{121}$$

Here N is traditionally the number of samples drawn form the true population. In this work, N is then the number of particles utilized in the RBPF. The null hypothesis is rejected when the test statistic is greater than a critical value, $T^2 > T^2_{crit}$, where the critical value is

$$T^2_{crit} = \frac{(N-1)\,p}{N-p} F_{p,N-p}\,(\alpha) \tag{122}$$

Here F is the F-cumulative distribution function with p and $N - p$ degrees of freedom respectively. Recall that each N is the number of particles, or component densities, and that each component density is a Gaussian function length of of dimension p. This CDF is evaluated at the user selected value of α, the probability of Type 1 error, also referred to as the "level of significance" of the test. Type 1 and Type 2 errors are two examples

of incorrect conclusions that could be reached by a hypothesis test. Type 1 error indicates that H_0 is actually true, but that H_0 is incorrectly rejected. Type 2 error indicates that H_0 is should have been rejected, but the hypothesis test failed to reject H_0.

While the T^2_{crit} critical region works well for the J_H analog as it approaches normality, sufficiently non-Gaussian distributions, such as J_E, are ill-suited for these tests. Because the number of particles N is typically large in the RBPF, one can also construct the the hypotheses tests with confidence regions that do assume normal distributions. These large sample inferences are made using the chi-squared distribution, with the critical value shown in Eq. (120) [118].

$$\chi^2_{crit} = \chi^2_p(\alpha) \tag{123}$$

Here, $\chi^2_p(\alpha)$ is the αth upper percentile of the chi-squared distribution with p degrees of freedom. This leads to Algorithm X, which systematically eliminates those hypotheses which are not consistent with observational data at each time step k.

Algorithm 2: Momentum and Energy Inference

```
function momentum inference (ω_{μ,k}, ω_{h,k}, A(x), α);
Input  : ω_{μ,k}, ω_{h,k}, A(x), α
Output: flag
For each time step;
for k ← 1 to T do
    For each hypothesis i;
    for h ← 1 to M do
        Evaluate test statistic, Eq. (121);
        ts ← N(ω_{μ,k} − ω_{h,k})^T A(x)^{-1} (ω_{μ,k} − ω_{h,k});
        Determine critical region, Eq. (123);
        χ²_crit ← χ²_p(α);
        if ts > χ²_crit then
            Reject H_0 at α level of significance;
            flag ← 0
        else
            Fail to reject H_0 at α level of significance;
            flag ← 1
        end
    end
end
```

6.1.4 Bounding Tracking Error with Detection Statistics

The appeal of the metrics presented in the previous section is that no additional information is required beyond that which is provided by the RBPF algorithm. However, shape model information is necessary for the light curve inversion process, meaning that the general size of the target SO is known. Therefore, it is possible to bound the maximum aperture diameter of the target SO optical system. If it is further assumed that the target satellite is attempting to rate track its subjects with an electro-optical sensor of its own, this information can be coupled with the statistics of the signal-to-noise ratio to determine a maximum relative angular velocity error that would yield detections of the hypothesized subject SOs. The simulated results also assume that this sensor is not individually articulated, and that the whole target SO maneuvers to track its subject. Finally, this specific formulation presented in this work further assumes that the target is taking unresolved images of the hypothesized subjects, but this assumption could be relaxed by replacing the signal-to-noise ratio (SNR) equation utilized.

For ease of illustration, the GMM of a single body axis is represented in Fig. 26. In the figure, $\phi_{\mu,k}$ is the estimated mean of the body angular velocity along the X-axis at the k^{th} time step and $\phi_{h,k}$ is the body angular velocity required at that time step to observe the h^{th} hypothesized subject. Please note that the univariate case is illustrated for ease of explanation only, as any mathematical technique should utilize the full Multivariate Gaussian Mixture Model (MGMM).

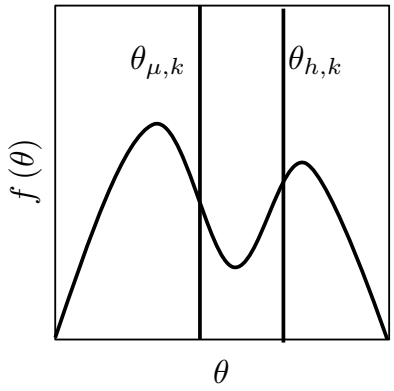

Figure 26: Direct State Space Classification

By subtracting each hypothesized body angular velocity from the distribution, one can define a distinct distribution for each hypothesized subjection satellite. Each body angular velocity error distribution is given at each time step by

$$\mathbf{e}_{h,k} = \|\boldsymbol{\omega}_{\mu,k} - \boldsymbol{\omega}_{h,k}\| \tag{124}$$

Each error PDF can then in turn be used to construct a cumulative distribution function (CDF) of body angular velocity errors, as shown in Fig. 27. To determine the probability that each hypothesized subject is under observation by the target, one determines the percentage of the error distribution whose particles had angular velocities less than the limit ω_ℓ. Please note that ω_ℓ is exactly equal to $\frac{\mathrm{d}\hat{\boldsymbol{\rho}}_{ij}(t)}{\mathrm{d}t}$ introduced in Eq. (107), and is substituted for brevity of notation.

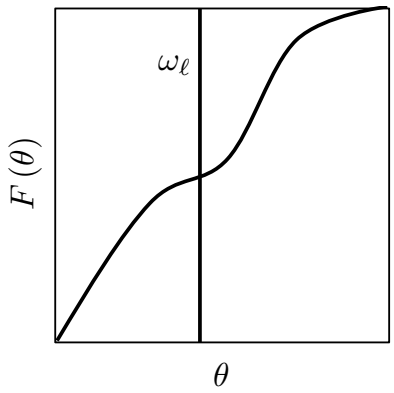

Figure 27: Cumulative Distribution Function of Error

It is known that as the angular rate error grows larger, the unresolved "point" of light grows into a streak. To quantify the angular error limit, ω_ℓ, that demarcates usable data one needs to relate this angular error and the quality of the unresolved image. One of the most commonly used metrics for expressing the quality of an image capturing is the signal-to-noise (SNR) ratio. Mathematically, it can be expressed as shown in Eq. (125), which is commonly referred to as the "CCD Equation."

$$\mathrm{SNR} = \frac{q_{\mathrm{SO}} t}{\sqrt{q_{\mathrm{SO}} t + m\left(1 + \frac{m}{z}\right)\left[\left(q_{p,\mathrm{back}} + q_{p,\mathrm{dark}}\right) t + \frac{\sigma_r^2}{n^2}\right]}} \tag{125}$$

In Eq. (125), q_{SO} is the photon flux of the subject captured by the target's optical system, t is the integration time of the sensor, m is the number of pixels occupied by SO, z is the

number of pixels used in estimate the background brightness, $q_{p,\text{back}}$ is the average brightness of the background, $q_{p,\text{dark}}$ is the dark current of the sensor, σ_r is the read noise, and n is the binning factor of the CCD. Texts have devoted to accurately modeling these parameters, but simple estimates are provided by the radiometric model of Chapter 3. To implement the SNR, the analyst must appropriately model the brightness of both the subject SO and the background of the image. To see how tracking errors influence the overall SNR of the image, one must examine the quantify m.

When the target is perfectly tracking the subject SO, then the value of m is constant. However, when tracking errors cause a relative velocity between the target's optical system and subject, m will increase monotonically with t. For unresolved images of the subject, the captured image will contain SO streaks. For a SO streaking across the image plane, the number of pixels occupied by the incoming signal grows as defined by Eq. (126).

$$m = m_0 + \frac{\sqrt{m_0}\omega_\ell t}{\text{IFOV}} \tag{126}$$

Here ω_ℓ is the tracking error limit, IFOV defines the angular field of view of a single pixel, and m_i is the number of pixels occupied by the point spread function (PSF) of the point source [24]. The PSF full width half maximum (FWHM) of a traditional, terrestrial observatory is influenced by the focus of the optical system, any atmospheric blurring, or the diffraction of light. Since the system under consideration is space-based, it is appropriate to utilize the diffraction limit and assume the optics are well focused.

The PSF due to diffraction limiting is the theoretical limit of an optical system's resolution due to the diffraction of light. For a perfectly circular aperture with no obscuration, the diameter of a point source is described by the "Airy disk." The angle in radians of the Airy disk is given by Eq. (127) [85].

$$\theta_A = \frac{2.44\,(\lambda)}{D} \tag{127}$$

It is important to note here that the diameter of the Airy disk is wavelength dependent, and therefore a weighted average for wavelength should be used.

While a large number of assumptions need to be made, the most critical for space-based applications, the aperture diameter of the target SO optical payload, can be inferred

Algorithm 3: Bounding Tracking Error with Detection Statistics

function bound track err ();
Input :
Output: flag
For each time step;
for $k \leftarrow 1$ **to** T **do**
    For each hypothesis i;
    for $h \leftarrow 1$ **to** M **do**
        Bound ω, *Eq.* (125) − *Eq.* (126);
        $\omega_\ell \leftarrow$ function SNR $(\mathbf{X}, \mathbf{p})$;
        Determine tracking error distribution, Eq. (124);
        $\mathbf{e}_{h,k} \leftarrow \|\boldsymbol{\omega}_{\mu,k} - \boldsymbol{\omega}_{h,k}\|$;
        Calculate Probability of Hypothesis with Cumulative Distribution Function;
        $\Pr(\mathbf{e}_{h,k} < \omega_\ell) \leftarrow F_{\mathbf{e}}(\omega_\ell)$;
    end
end

from observational data. Recall that the aperture diameter was established as the greatest contributor to limiting magnitude from Chapter 4. Size estimation techniques routinely provide estimates of optical cross section and its derivatives in various photometric bands, and it is therefore possible to bound D [28, 119, 53]. Likewise, the lower bound on focal ratio, or f-number, of an optical system is limited by optical aberrations [77]. The SNR required to determine a value of ω_ℓ is user selectable and could incorporate

6.1.5 Operational Mode Classification

While the focus of this work is determining the active control mode of SO, these techniques could easily be extended to encompass historically defined operational modes. The term operational mode typically refers to broad categorical behaviors such as "nominal," "anomalous," or "nadir pointing." In the case of non-SO subjects, such as the Sun or nadir, these subjects can simply be included as additional hypotheses as demonstrated in the Results section. Determining anomalous behavior is more involved, as one must baseline which observation subjects are nominal. However, with such a baseline, the determination of subjects different from those composing the baseline is a relatively simple endeavor.

6.2 Results

Simulated results for the methodologies outlined in this work are presented below. Subsection 6.2.1 outlines some important considerations for accurately replicating the results presented in this paper. Subsection 6.2.2 outlines the single test case scenario, and highlights the results available directly from the RBPF. Subsection 6.2.3 presents results of the active control mode analysis using the contributions of this work.

6.2.1 Practical Implementation Notes

An important consideration of the methodologies outlined above is to account for the fact that motion about one or more body axes may be unobservable. This is the case with the example simulation utilized to produce these results. In the simulated scenario, any arbitrary rotation about the body y-axis does not cause any significant change to the visible areas of the target SO. As a result information on this axis, such as the mean angular velocity, should be excluded. Mathematically, this implies that $p = 2$ degrees of freedom, and that any vector $\boldsymbol{\omega}$ should contain only the roll and yaw axes.

Additionally, simple checks can reduce the initial hypothesis space. The first is to ensure that the target SO can maintain line of sight with the subject SO. Simple algebraic algorithms have been developed which remain computationally tractable even for a large set of hypothesized subjects. Similar checks exist to ensure that the subject is illuminated with respect to the target SO. The specific line-of-sight algorithm implemented to generate the results here is Algorithm 35 by Vallado [120].

Finally, it is informative to review what is both known and unknown about the target SO. Using only measurements of the brightness coupled with knowledge on the shape and material properties of the SO, one is able to estimate the attitude and attitude rate states of a maneuvering satellite. One does not require an initial guess for the orientation of the satellite, the inertia tensor, or the torques applied by actuators on the SO.

Table 16: Known Quantities for Light Curve Inversion using RBPF

Quantity	Known	Unknown
Inertia Tensor		✓
SO Torques		✓
Initial Attitude		✓
SO Shape Model	✓	

6.2.2 Simulated Scenario

The simulated results presented assume that the observer is located at the Remote Maui Experiment (RME) in Kihei, HI. The telescope parameters utilized are those of the 0.5 m f/8 GT-SORT telescope, and are representative of a typical Raven-class telescope [19]. The simulated target SO is the Intelsat-18 satellite, where the TLE was downloaded from SpaceTrack.org. The simulation represents observations collected on October 5th, 2015 from 08:05:00 to 08:15:20 UTC.

```
INTELSAT 18
1 37834U 11056A 15276.58183779 .00000024 00000-0 00000+0 0 9992
2 37834 0.0167 127.6907 0001915 64.8570 208.8878 1.00269536 14658
```

The position and velocity vectors generated from this TLE specify the IS-18 spacecraft orbit at $a = 42,166$ km, $e = 1.8 \times 10^{-4}$, $i = 0.027$ deg, $\Omega = 156.6$ deg, $\omega = 46.9$ deg, and $f = 111.4$ deg. The TLE is ingested into the MATLAB implementation of the Simplified General Perturbations Propagator (SGP4) developed by Vallado et. al. [106]. The ephemerides of the Sun and Earth are calculated with less than 1" error using the 1987 implementation of Variations Séculaires des Orbites Planétaires (VSOP87) [107]. These programs use the mean equator and equinox of J2000 to define the Earth Centered Inertial (ECI) reference frame

The shape model of NOAA 18 is simplified to that of a simple cube, with the shape model parameters presented in Table 17. This simplification is made to expedite the simulation runs and is not a limitation of the RBPF. The measurements are simulated with a BRDF which uses an affine combination of the Cook-Torrance BRDF model for specular reflectance [110] and Lambertian reflectance for diffuse reflectance. In the shape model, A is the facet area, ξ is the affine transformation weighting parameter, a is the diffuse albedo, and m is the microfacet slope parameter where ξ, a, and m $\in [0,\ 1]$ [51].

Table 17: Assumed Shape Model Parameters

Facet	A (m)	ξ	a	m
+X	2	0.5	0.25	0.3
+Y	2	0.5	0.5	0.3
+Z	2	0.5	0.75	0.3
-X	2	0.5	0.9	0.3
-Y	2	0.5	0.4	0.3
-Z	2	0.5	0.1	0.3

Table 18: Hypothesized Subject SO

Catalog ID Number	Common Name	$\overline{MDM}$ (deg)
16111	SL-3 R/B	8.89
21423	SL-14 R/B	-
21397	OKEAN-3	9.58
16182	SL-16 R/B	9.70
18187	COSMOS 1867	10.18
19120	SL-16 R/B	8.84
20511	SL-14 R/B	-
22803	SL-16 R/B	-
25400	SL-16 R/B	9.49
27422	IDEFIX & ARIANE 42P R/B	11.34
28059	CZ-4B R/B	-
31793	SL-16 R/B	9.03

Since previous work has addressed shape model uncertainty, this work assumes the shape model is known perfectly [51]. To simulate the motion of IS-18, the problem is modeled such that the optics payload is fixed to the -Y facet of IS-18 which rate tracks SO 16111, an SL-3 R/B, for the duration of the pass. Table 18 lists the 12 hypothesized subjects for this simulation, all orbiting about the North Pole. It is again emphasized that this set of hypotheses represent a mutually exclusive and open set. It is by no means an exhaustive list of potential targets.

Fig. 28 illustrates the problem geometry, where the simulated subject SOs are highlighted in red, and the blue line denotes the true target. Emphasizing the difficulty of this problem, Fig. 29 illustrates the subjects from IS-18's point of view. It is easily seen how attitude information alone makes inference of the most probable subject difficult.

The attitude states estimated by the RBPF are presented in Fig. 46 and Fig. 47. Fig. 46 shows the 2D view of the roll and pitch axes, and each subfigure is a different time step

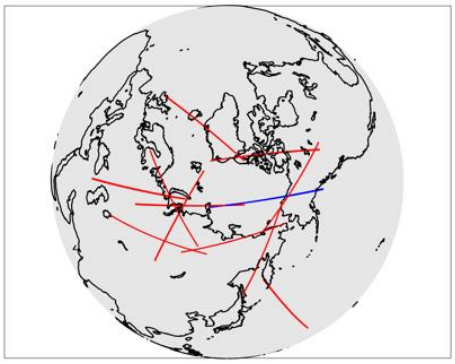

Figure 28: Top-Down View of Simulated Scenario

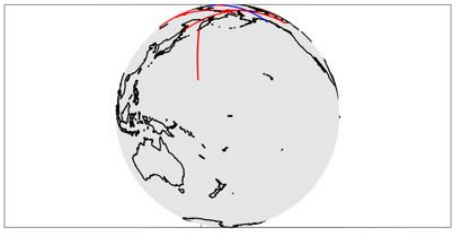

Figure 29: Depiction of Subject SO from Perspective of IS-18

in the simulation. Fig. 47 shows the 2D view of the roll and yaw axes, where each subfigure again denotes a separate time step. In the figures, the dots are the particles of the RBPF each shaded to indicate the likelihood measured for that particle. Black indicates the most likely particles, while light grey indicates less likely particles. The red star indicates the true attitude state of IS-18 necessary to track SO 16111.

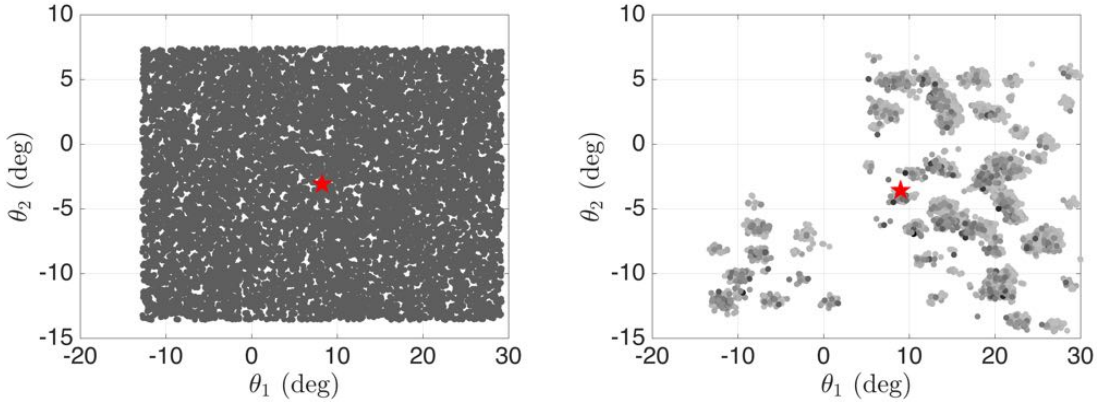

(a) 05-Oct-2015 08:05:00 UTC

(b) 05-Oct-2015 08:08:06 UTC

(c) 05-Oct-2015 08:11:32 UTC

(d) 05-Oct-2015 08:15:09 UTC

Figure 30: 2D View of $\boldsymbol{\theta}_1$ - $\boldsymbol{\theta}_2$

Fig. 32 represents the same particle cloud and time step as Subfigure 48(c) and Subfigure 31(a), but the Euler angles have been transformed to Topocentric Equatorial coordinates. The x-axis denotes right ascension, the y-axis declination, and the origin is fixed to the camera bore-sight of the target SO. Consequently, the blue star representing the true target remains fixed at the origin, just above the North Pole. The green circle is the Earth exclusion zone, the black triangle is the centroid of the particle cloud, and the orange dots represent

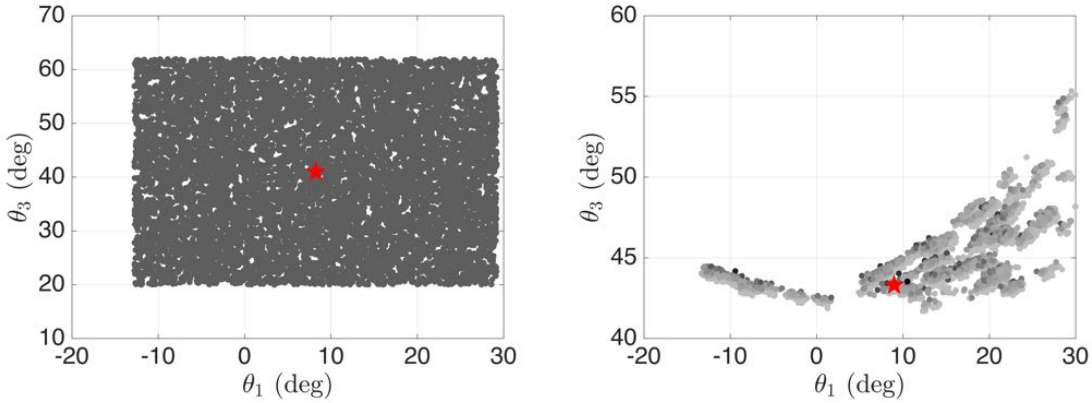

(a) 05-Oct-2015 08:05:00 UTC

(b) 05-Oct-2015 08:08:06 UTC

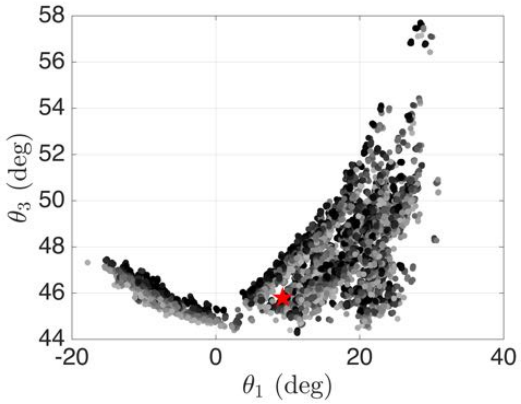

(c) 05-Oct-2015 08:11:32 UTC

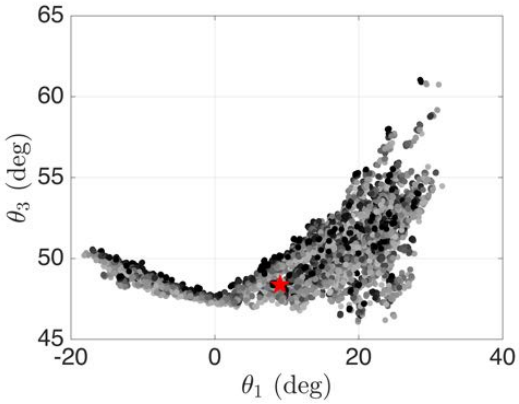

(d) 05-Oct-2015 08:15:09 UTC

Figure 31: 2D View of $\boldsymbol{\theta}_1$ - $\boldsymbol{\theta}_3$

the incorrect hypotheses. It can be seen that the initial particle cloud, defined as uniform over the SO(3) space of Euler angles, initially covers the entire earth.

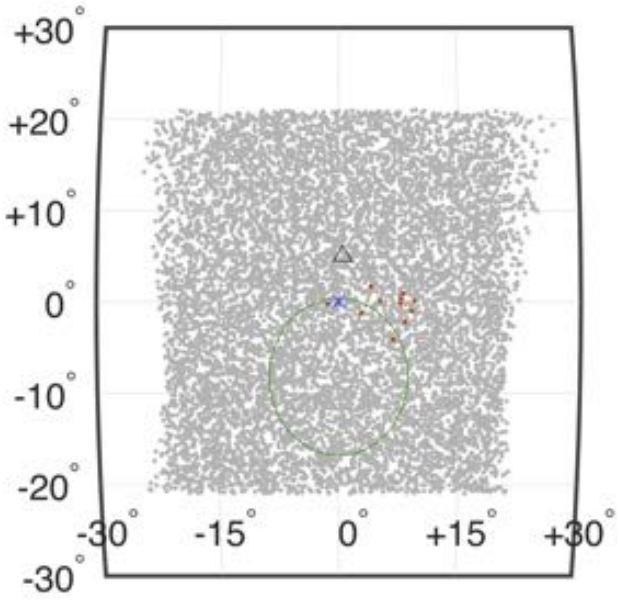

Figure 32: 05-Oct-2015 08:05:00 UTC

Fig. 33 represents the same particle cloud and time step as Subfigure 30(d) and Subfigure 31(d), with the same symbology as Fig. 32. It can be seen that the particle cloud is reduced from its initial coverage to a band the spans the poles of the Earth. The geometry of the cloud is likely due to the lack of observability along the y-axis as well as the simplistic shape model utilized for IS-18.

6.2.3 Active Control Mode Inference

Using these state estimates, results for the proposed active control mode inference techniques are presented. For the instantaneous angle, the first step in obtaining a more accurate centroid involves the k-means++ algorithm. Fig. 34 illustrates the technique applied at a single time step.

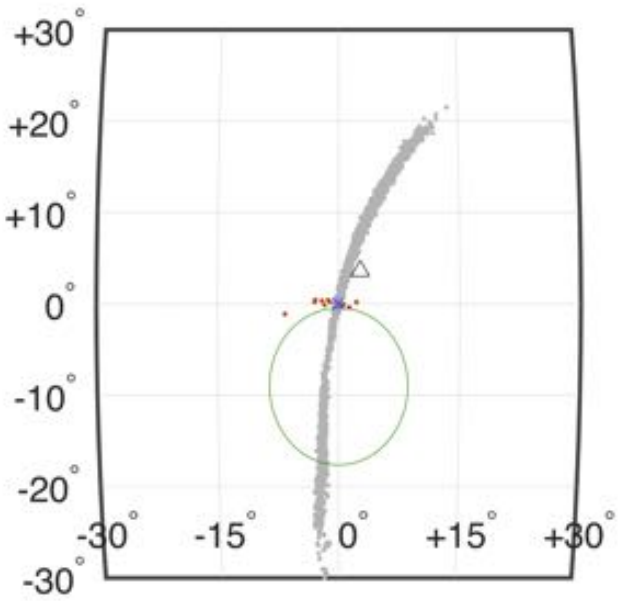

Figure 33: 05-Oct-2015 08:15:09 UTC

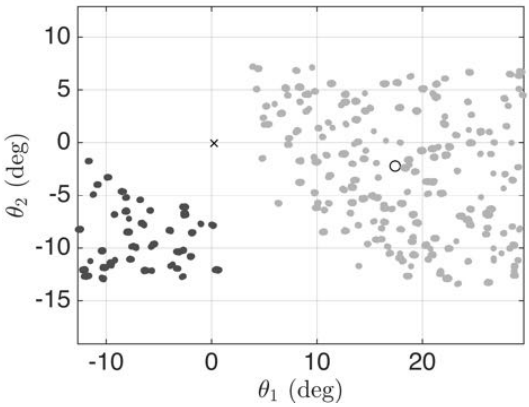

Figure 34: 2D View of Attitude States Sorted Via k-means

Having sorted the particle cloud to obtain more accurate centroids, Eq. (99) determines the instantaneous angle between the estimated bore-sight of the SO, the -Y facet of IS-18, and each hypothesized line-of-sight vector. Fig. 35(a) illustrates which hypothesis had the smallest instantaneous angle during the observation window. The y-axis labels each hypothesis and the true subject of the target SO, 16111, is at the top of the chart. Fig. 35(b) illustrates the instantaneous angle for all 5 SO that exhibited the smallest instantaneous angle for at least one time step. Here, the y-axis is the instantaneous angle and not the index of the hypothesized subject. Inspection of both Fig. 35(a) and Fig. 35(b) reveals that by using this instantaneous angle, the true subject is never identified, even when starting close to the right hypothesis.

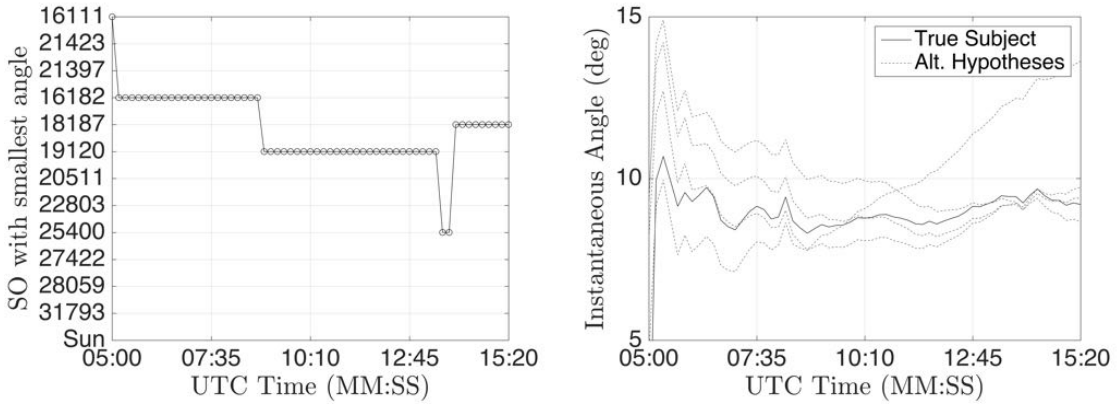

(a) Hypothesis with Smallest Instantaneous Angle (b) Instantaneous Angle for 5 Selected Hypothesis

Figure 35: Classifying ACM with Instantaneous Angle

This fact motivated the MDM, given by Table 18. Inspection of the time averaged MDM reveals that the true subject rate tracked by the target had the second smallest mean MDM. However, the error between the true subject and that which is predicted most likely by the MDM is .05 deg. There are several cases where both the instantaneous angle or the average MDM can give incorrect results. The first case is subjects whose orbits pass serendipitously close to the true subject for arbitrary durations of time from the perspective of the target SO. This is the case for object 19120, as seen in Fig. 35(a). Another case occurs when the SO happens to be in a very similar orbit plane as the true subject SO, perhaps only differentiating by a small offset in Euclidian space. This is the case for object

21397. Because of instances like these, the ability to estimate the body angular velocities is crucial element of successful SO operational mode classification.

The first proposed metric which relies on this extra information is the Mahalanobis distance. Fig. 36 plots the hypothesis with the smallest MD at each time step. Inspection of the figure reveals that the true subject, 16111, is correctly identified by the smallest MD in 77% of the time steps. The other SO identified by a small MD, 21397, is in an orbit very similar to the true subject. To further examine how similar the orbits of these two hypotheses appear to the target SO, the momentum analog is utilized.

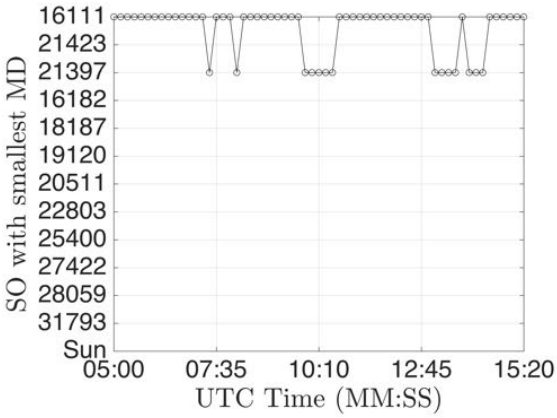

Figure 36: SO with smallest Mahalanobis Distance

The two sided hypothesis test for equal means is carried out at each time step of the observation. Fig. 37 illustrates the t-statistic value of each hypothesis as dashed black lines, and the critical region demarcation as a solid black line at the $\alpha = .1$ significance level. Fig. 38 plots the same information, where those hypotheses which have not been rejected as likely observation targets are plotted as a function of time.

Fig. 38 shows that given the estimated covariance of the body angular velocities, the mean body angular velocities required to track objects 16111 and 21397 are equivalent over the entire observation period. Two additional objects also periodically appear to have the same velocities. This is due to the fact that both of these objects are moving predominantly in the direction of the body y-axis, which has been neglected from these calculations since it is unobservable. This methodology reinforces the general philosophy that observational evidence can only used to eliminate hypotheses.

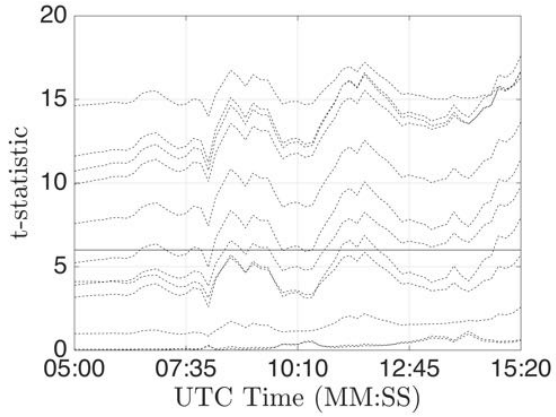

Figure 37: Varying t-statistic of Each Hypothesis

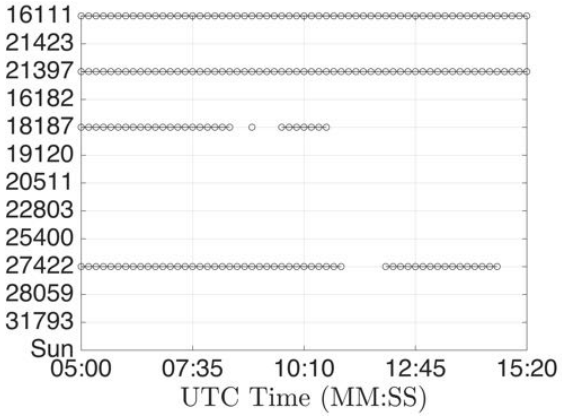

Figure 38: Angular Momentum Classification

Table 19: System Parameters

Parameter	Units	Value
aperture diameter of target SO	m	0.2
focal ratio of target SO	-	6
pixel size of target SO sensor	m	5e-6
irradiance of magnitude 0 source	photons/s/m^2	$5.6 \cdot 10^{10}$
atmospheric seeing/mount jitter	arcsecond	.5
sky brightness	m_v/as^2	30
CCD quantum efficiency	-	.6
CCD dark current	e/pixel/s	.5
algorithm required SNR	-	15
atmospheric transmittance	-	1
optical transmittance	-	.9
secondary transmittance	-	1

The results for the final proposed methodology are summarized in Fig. 39 and Fig. 40. These figures show the percentage of the angular velocity posterior distribution which is below the angular velocity limit, $\omega_e = 4 \cdot 10^{-5}$ rad/sec, which resulted in SO subject streaks having SNR ≥ 15. In lieu of more detailed modeling, every object is assumed to have a 16 m_v apparent visual magnitude with respect to the target SO. Table 19 enumerates the other parameters assumed in this work to simulate an optical environment similar to those on orbit. For brevity, only the first and last 3 hypotheses are depicted, as all others had near 0 probability.

Examining Fig. 39 reveals that the true subject SO, 16111, had the most time steps where 100% of the distribution is below the threshold. As expected, the next most likely hypothesis is again 21397. The remaining hypotheses all appeared as in Fig. 40, with none of the particles meeting the SNR requirements.

6.3 Summary

Several methodologies for directly identifying the observational target of a target space object are presented. The ability of the RBPF to provide estimates of the body angular velocities as well as attitude states, proves to be a key enhancement over previous techniques. Critically, the proposed contributions enable the discrimination of targets which are co-located along the SO bore-sight. The fusion of these estimates enables the contributions of

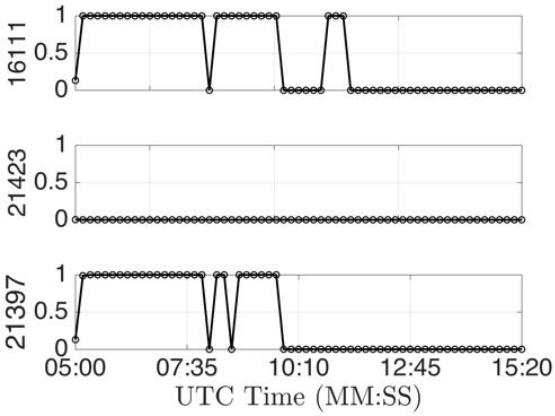

Figure 39: Classification Based on SNR

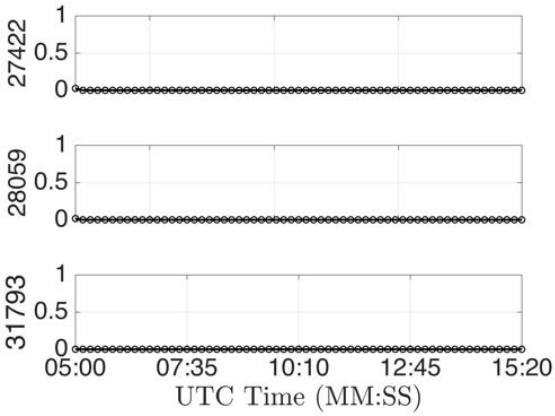

Figure 40: Classification Based on SNR

this work to offer more precise descriptions of active control mode. By providing the target the observed SO is tracking, rather than the categorical classifications previously described in the literature, analysts can infer the mission purpose of a target SO, a key component of SDA.

CHAPTER VII

HUBBLE SPACE TELESCOPE TEST CASE

This chapter outlines the application of the RBPF to experimentally collected data, where again the motivating scenario is as follows: An agile SO under surveillance by an SDA stakeholder, termed the "target" SO, is hypothesized to be actively rate-tracking other SO, called "subject" SO, with its optical payload. A perfect real world example of such an SO is the Hubble Space Telescope (HST). The overall goal is to identify, from a mutually exclusive but not exhaustive list of hypotheses, which subject is under observation by the target SO. As discussed in the previous chapter, this task has been defined as inferring the SO "active control mode."

7.1 Methodology

7.1.1 Experimental Data

On July 12$^{\text{th}}$, 2008 the Advanced Electro-Optical System (AEOS) telescope was used to collect data on the HST as it overflew the Air Force Maui Optical and Supercomputing (AMOS) facility in Haleakalā, HI. The two-line element (TLE) file available before the pass is:

```
HST
1 20580U 90037B 08193.95559624 +.00000231 +00000-0 +49464-5 0 9998
2 20580 028.4680 161.6750 0003581 282.5497 077.4696 15.00391554798708
```

Data was collected at roughly 1 Hz in the Johnson-Cousins V-band, from 480nm to 660nm, and converted to the exo-atmospheric magnitudes as shown in Fig. 41. The conversion to magnitudes is performed using the zero magnitude reference flux, $E_0 = 1.85 \cdot 10^{-9} \frac{W}{m^2}$ as reduced by Colina et al.[121]. In the figure, the solid black line is the true measured brightness of the Hubble Space Telescope and the dashed black line is the brightness simulated using the bi-reflectance distribution function (BRDF) model. Subsection 7.1.2 briefly describes the simplified BRDF implemented.

The true attitude of the Hubble Space Telescope is available via the European Space

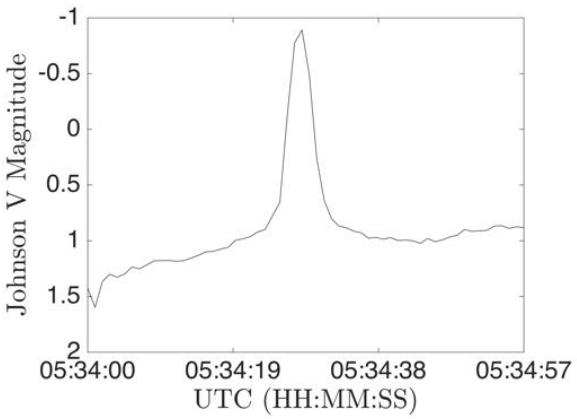

Figure 41: Measured Light Curve of HST

Table 20: Observation Schedule of HST on July 12$^{\text{th}}$, 2008

Obs. Start Time (UTC)	Obs. End Time (UTC)	Right Ascension (J2000)	Declination (J2000)
2008-07-12 04:26:35	2008-07-12 05:08:10	16h 38m 13.48s	-68d 27' 19.35"
2008-07-12 05:59:58	2008-07-12 06:01:12	16h 38m 13.32s	-68d 27' 18.20"

Agency (ESA) Hubble Science Archive. The start times and geocentric equatorial coordinates of these two observations, identification numbers NA1E46010 and NA1E46ZIQ, are listed in Table 20 [122]. Hubble was imaging ESO-069-IG-006-SOUTH, as shown in Fig. 42. While Hubble was not actively imaging while passing over AMOS, STSCI lists this target for the window spanning 04:18:10 UTC to 06:03:02 UTC on the night of July 12$^{\text{th}}$, 2008 [123]. Therefore, it is assumed that the true attitude of Hubble is equal to the first observation. In either case, any change in brightness due to the minuscule difference in attitude is within the measurement noise of any ground based optical system.

7.1.2 Measurement Model of Hubble Space Telescope

A simplified facet model of the HST, as shown in Fig. 43, was developed for light curve inversion. This facet model is coupled with the affine combination of two BRDF models, which together serve as the measurement function for the sequential filter. The Cook-Torrance BRDF model is utilized for specular reflections, and Lambertian reflectance is used for diffuse reflections. The resultant composite BRDF model is given by Eq. (128), where the facet index is removed for compactness.

$$\rho\left(\hat{\mathbf{n}}^{\mathcal{B}}, \hat{\mathbf{s}}^{\mathcal{B}}, \hat{\mathbf{v}}^{\mathcal{B}}, \xi, a, m\right) = \xi R_d + (1-\xi)\, R_s \tag{128}$$

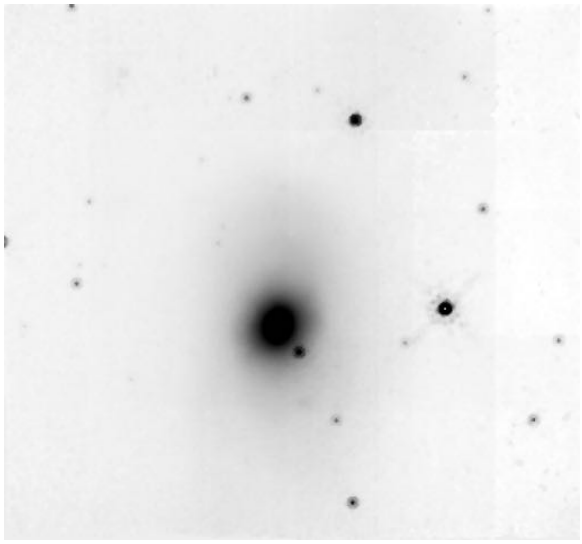

Figure 42: RA: 16h 38m 13.48s, DEC: -68d 27' 19.35"

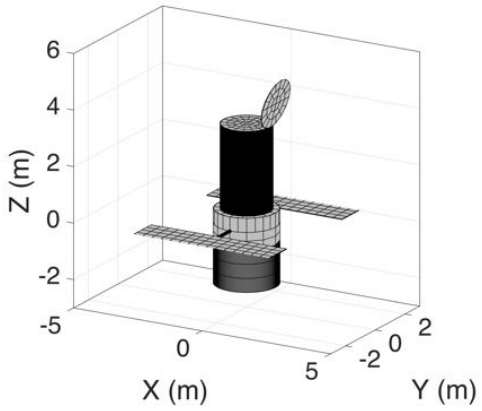

Figure 43: HST Facet Model

In Eq. (128), $\xi \in [0,1]$ is the affine weighting parameter which dictates how much the reflect depends on the diffuse, R_d, or specular, R_s reflection respectively. The additional facet parameters are the microfacet slope parameter, $m \in [0,1]$, and the diffuse albedo, $a \in (0,1]$. The diffuse reflection is given simply by Eq. (129).

$$R_d = \frac{a\left(\hat{\mathbf{n}}^{\mathcal{B}} \cdot \hat{\mathbf{s}}^{\mathcal{B}}\right)}{\pi} \tag{129}$$

The specular reflection is given by Eq. (130).

$$R_s = \frac{F}{\pi} \frac{D}{(\hat{n}^{\mathcal{B}} \cdot \hat{\mathbf{s}}^{\mathcal{B}})} \frac{G}{(\hat{n}^{\mathcal{B}} \cdot \hat{\mathbf{v}}^{\mathcal{B}})} \tag{130}$$

The first of the three constitutions parts, denoted F, is given as Eq. (131).

$$F = \frac{1}{2} \frac{(g-c)^2}{(g+c)^2} \left[1 + \frac{(c\,(g+c)-1)^2}{(c\,(g-c)-1)^2}\right] \tag{131}$$

In Eq. (131), $g^2 = n^2 + c^2 - 1$, while $c = \left(\hat{\mathbf{v}}^{\mathcal{B}} \cdot \hat{h}^{\mathcal{B}}\right)$, and n is given by

$$n = \frac{1-\sqrt{F_0}}{1+\sqrt{F_0}} \tag{132}$$

The second constitution part of Eq. (130), the Beckmann distribution function denoted D, is given by Eq. (133).

$$D = \frac{1}{\pi m^2 \cos^4 \gamma} \exp\left(\frac{-\tan^2 \gamma}{m^2}\right) \tag{133}$$

In Eq. (133), $\gamma = \cos^{-1}\left(\hat{\mathbf{n}}^{\mathcal{B}} \cdot \hat{\mathbf{h}}^{\mathcal{B}}\right)$, and the final constituent part of the specular reflectance is defined by Eq. (134).

$$G = \min\left\{1, \frac{2\cos\gamma\left(\hat{\mathbf{n}}^{\mathcal{B}} \cdot \hat{\mathbf{v}}^{\mathcal{B}}\right)}{\left(\hat{\mathbf{v}}^{\mathcal{B}} \cdot \hat{\mathbf{h}}^{\mathcal{B}}\right)}, \frac{2\cos\gamma\left(\hat{\mathbf{n}}^{\mathcal{B}} \cdot \hat{\mathbf{s}}^{\mathcal{B}}\right)}{\left(\hat{\mathbf{v}}^{\mathcal{B}} \cdot \hat{\mathbf{h}}^{\mathcal{B}}\right)}\right\} \tag{134}$$

Together, these equations form the affine BRDF utilized in this effort. As discussed by Holzinger et al., the affine weighting parameter ξ enables the simplification $a = F_0$ to be made, since freedom exists in ξ. The total reflectance of the SO, ρ, can be related to the measured intensity, I, by summing over each individual facet of the shape model, i, as defined in Eq. (135).

$$I_\Lambda\left(\boldsymbol{\theta}_I^B, \hat{\mathbf{s}}, \hat{\mathbf{v}}, \xi, a, m\right) = J_\Lambda \sum_i^N A_i\ \rho_{\Lambda,i}\left(\hat{\mathbf{n}}^{\mathcal{B}}, \hat{\mathbf{s}}^{\mathcal{B}}, \hat{\mathbf{v}}^{\mathcal{B}}, \xi, a, m\right) \tag{135}$$

The total irradiance of the Sun at the satellite is denoted J_Λ which emphasizes that this value is integrated over bandwidth Λ. In reality, the total reflectance is also wavelength dependent, but in this work the wavelength average of 548.3 nm is utilized [121]. An Unscented Kalman Filter is implemented to iteratively solve for a constant value for each shape model parameter $[p = A,\ a,\ m,\ \xi]$, excluding the area. Despite this, using theoretical BRDFs to match experimentally collected data is challenging, as shown in Fig. 44. Fig. 44(a) illustrates the measured radiant intensity alongside the radiant intensity modeled using the BRDF along with the true attitude. Fig. 44(b) plots the residuals between the truth and modeled truth over the observation window. One can see the BRDF poorly models the spike in the measured light curve, which is likely a specular glint.

This error is likely due to a number of uncertainties which could include: the facet-based approximation of the areas that are both illuminated and visible to the observer, uncertainties in the true solar irradiance, uncertainties in the true material properties of the HST, or uncertainties in the wavelength dependent losses of the atmosphere, optical assembly, or the sensor itself. If the photometric reduction is performed properly, the uncertainties due to loss through the atmosphere and optical train should be minimized. Therefore, it is assumed that most of the error is due to the BRDF model and materials property uncertainties. The material properties uncertainties are incorporated by evaluating the Jacobian of the analytic BRDF. Assuming the uncertainty in each shape model parameter p is zero mean and uncorrelated, and dropping the index notation i, leads to the following Taylor series expansion.

$$\sigma_I^2(p) = \left(\frac{\partial I_\Lambda\left(\boldsymbol{\theta}_I^B\right)}{\partial A}\right)^2 \sigma_A^2 + \left(\frac{\partial I_\Lambda\left(\boldsymbol{\theta}_I^B\right)}{\partial a}\right)^2 \sigma_a^2 + \left(\frac{\partial I_\Lambda\left(\boldsymbol{\theta}_I^B\right)}{\partial m}\right)^2 \sigma_m^2 + \left(\frac{\partial I_\Lambda\left(\boldsymbol{\theta}_I^B\right)}{\partial \xi}\right)^2 \sigma_\xi^2 \quad (136)$$

This same procedure can be carried out for the uncertainty in J_Λ. Not only does the Sun exhibit natural variations in power output, Earth orbiting bodies are subject to illuminating reflected by the Earth itself, commonly referred to as "Earthshine." The simulation does not model this effect, but it is present in the real data. Thus, following the same methodology

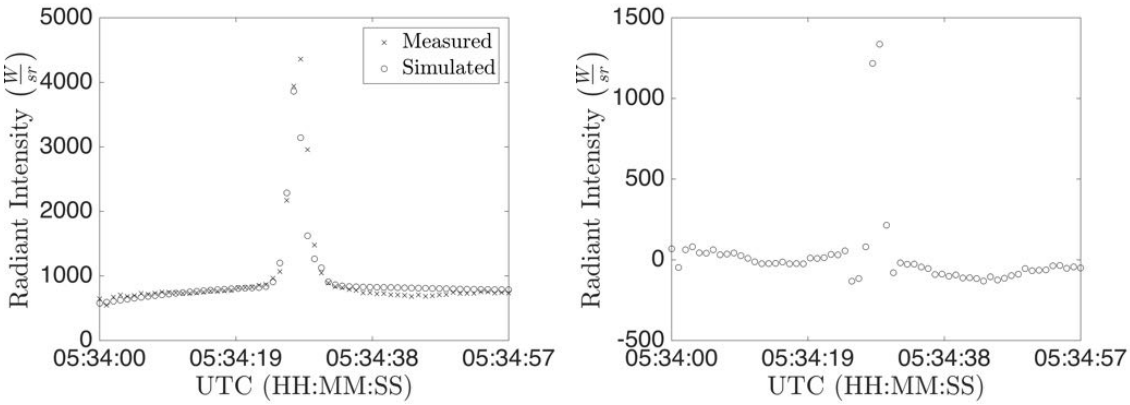

(a) Light Curve Modeled Using True Attitude

(b) Residuals of Truth Model

Figure 44: Model Induced Error During Measured Glint

as above

$$\sigma_I^2\left(J_\Lambda\right) = \left(\sum_i^N A_i\ \rho_{\Lambda,i}\right)^2 \sigma_{J_\Lambda}^2 \tag{137}$$

This expansion is evaluated analytical using the MATLAB Symbolic Toolbox. The resulting functions are evaluated at every time step for each facet using the true attitude of the HST. The notation indicating the explicit dependence of the simulated intensity on attitude is kept in Eq. (138) to emphasize that the measurement uncertainty is attitude, and hence time dependent. Taken together, the measurement model utilized in this study is

$$z_k \sim \mathcal{N}\left(I_k, \sigma_{I,k}^2\left(p\right) + \sigma_{I,k}^2\left(J_\Lambda\right)\right) \tag{138}$$

It should be noted that assuming the measurement errors to be Gaussian distributed is an approximation. While the large photon flux caused by the brightness of the HST is safely approximated as Gaussian, the uncertainty in the exact wavelength of the photons incident on the sensor can cause this approximation to be violated. However, approximating the radiant intensity as Gaussian is a better assumption than approximating magnitude errors as Gaussian.

7.1.3 Dynamics Modeling of Hubble Space Telescope

This work builds on results of Chapter 5 and so the Rao-Blackwellized Particle Filter will not be covered in depth in this section. The fundamental challenge of performing light curve inversion of agile SO is that the attitude kinematics are well known but the angular velocity

dynamics may be unknown due to unknown control torques, unknown inertia tensors, and unknown disturbance torques [51]. The true state dynamics for SO rotational motion is given by Euler angles kinematic relationship and Euler's rotational equation of motion. The symbol $\mathbf{B}\left(\boldsymbol{\theta}_I^B\right)$ defines the non-orthogonal relationship between the body angular rates and the attitude coordinates used to represent SO(3) in the inertial frame [124].

$$\begin{bmatrix} \dot{\boldsymbol{\theta}}_I^B \\ \dot{\boldsymbol{\omega}} \end{bmatrix} = \begin{bmatrix} \mathbf{B}(\boldsymbol{\theta}_I^B)\boldsymbol{\omega} \\ -\mathbf{J}^{-1}\left(\boldsymbol{\omega} \times \mathbf{J}\boldsymbol{\omega}\right) + \mathbf{J}^{-1}\mathbf{T} \end{bmatrix} \tag{139}$$

The system state is defined as $\mathbf{x}^T = [\boldsymbol{\theta}_I^{B^T}\boldsymbol{\omega}^T]^T$ where $\boldsymbol{\theta}_I^B$ are the 3-2-1 Euler angles defining the rotation between the SO body frame, B, to the inertial frame, I, and the body angular velocity of the SO is denoted by $\boldsymbol{\omega}$. Here, $\mathbf{J}$ and $\mathbf{T}$ represents the true inertia tensor matrix and the sum of all applied control and external torques respectively. For agile SO the true inertia and torques acting on a SO are typically unknown.

To model the unknown inertia matrix and torques acting on an agile SO, an exponentially correlated angular acceleration dynamic model is adopted. This leads to the continuous dynamics model proposed in this work for agile SO.

$$\begin{bmatrix} \dot{\boldsymbol{\theta}}_I^B \\ \dot{\boldsymbol{\omega}} \\ \dot{\boldsymbol{\alpha}} \end{bmatrix} = \begin{bmatrix} \mathbf{0}_{3\times3} & \mathbf{B}\left(\boldsymbol{\theta}_I^B\right) & \mathbf{0}_{3\times3} \\ \mathbf{0}_{3\times3} & \mathbf{0}_{3\times3} & \mathcal{I}_{3\times3} \\ \mathbf{0}_{3\times3} & \mathbf{0}_{3\times3} & \mathrm{diag}\left(-\boldsymbol{\beta}\right) \end{bmatrix} \begin{bmatrix} \boldsymbol{\theta}_I^B \\ \boldsymbol{\omega} \\ \boldsymbol{\alpha} \end{bmatrix} + \begin{bmatrix} \mathbf{0}_{3\times3} \\ \mathbf{0}_{3\times3} \\ \mathcal{I}_{3\times3} \end{bmatrix} \mathbf{w} \tag{140}$$

The body angular velocity is defined as $\boldsymbol{\omega}$ and $\boldsymbol{\alpha}$ is the body angular acceleration. The process noise, used to simulate the unknown motion of the SO, is denoted as $\mathbf{w}$ and driven by the power spectral density of the angular acceleration, as given by Eq. (141).

$$Q_\alpha(\tau) = 2\beta\sigma_m^2\delta\left(\tau\right)\mathcal{I}_{3\times3} \tag{141}$$

The success of this model lies on the successful determination of $\beta = \frac{1}{\tau}$, where τ is the time constant, and σ_m^2, the variance of the angular acceleration. Since β is the inverse of τ, it is selected by matching τ to the length of the expected SO maneuver.

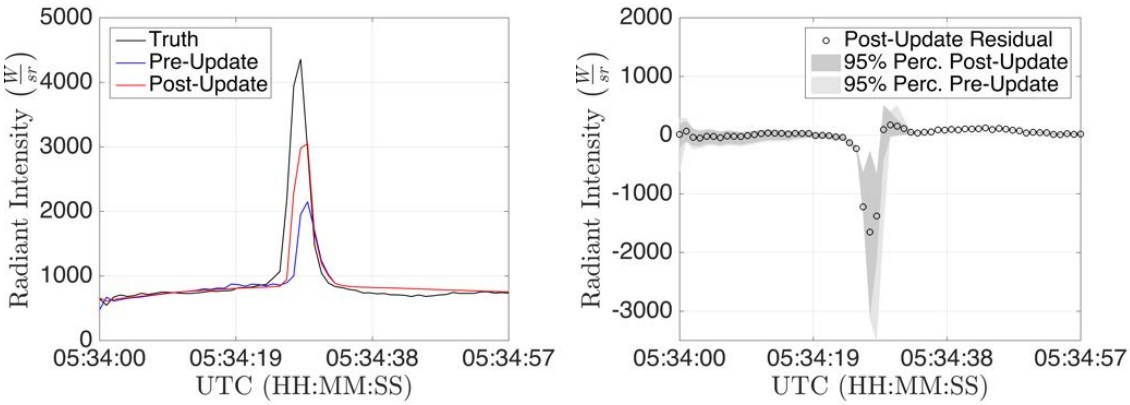

(a) Simulated Light Curve Using True Attitude

(b) Simulated Measurement Residuals

Figure 45: Pre and Post Update Estimate of Light Curve with Residuals

7.2 Results

7.2.1 Estimated Posterior State Distributions

The RBPF is utilized to estimate the posterior state distributions of the attitude and body angular velocity states. The aforementioned TLE is ingested into the scenario simulation, which is comprised of SGP4, VSOP87, and the BRDF described in Chapter 5. To model the unknown dynamics of the HST, variance of the acceleration is assumed to be $\sigma_m^2 = 10^{-5}$ rad^2 / sec^4 and $\beta_1 = \beta_2 = \beta_3 = 1/30$. The shape model uncertainty is assumed to be $\sigma_A^2 = .1A$, $\sigma_a^2 = 0.5$, $\sigma_m^2 = 0.2$, $\sigma_\xi^2 = 0.4$ and the uncertainty in the solar radiance is $\sigma_{J_\Lambda}^2 = 0.25$.

Fig. 49(a) shows the pre-update and post-update estimated measurement of the RBPF, along with the true measurements collected with AEOS in units of $\frac{W}{sr}$. As expected, it is observed that model errors in the BRDF results in the RBPF underestimating the intensity. Fig. 49(b) illustrates the residuals, with the large error aligning with the measured glint, as discussed previously.

The attitude states are shown in Fig. 46 and Fig. 47, where 2D views are given of the roll/pitch and roll/yaw axes represented with Euler angles. Each subfigure illustrates the distribution at a specific time step. The cloud of dots illustrate the individual particles of the RBPF, where a light gray to dark black shading indicates the least likely and most likely particles, respectively. The true attitude of HST is given by the red star. One can

see by examining the lower left subfigure that the model error introduced by the BRDF causes the RBPF to eliminate many particles. Despite this, the RBPF successfully tracks the HST throughout the pass.

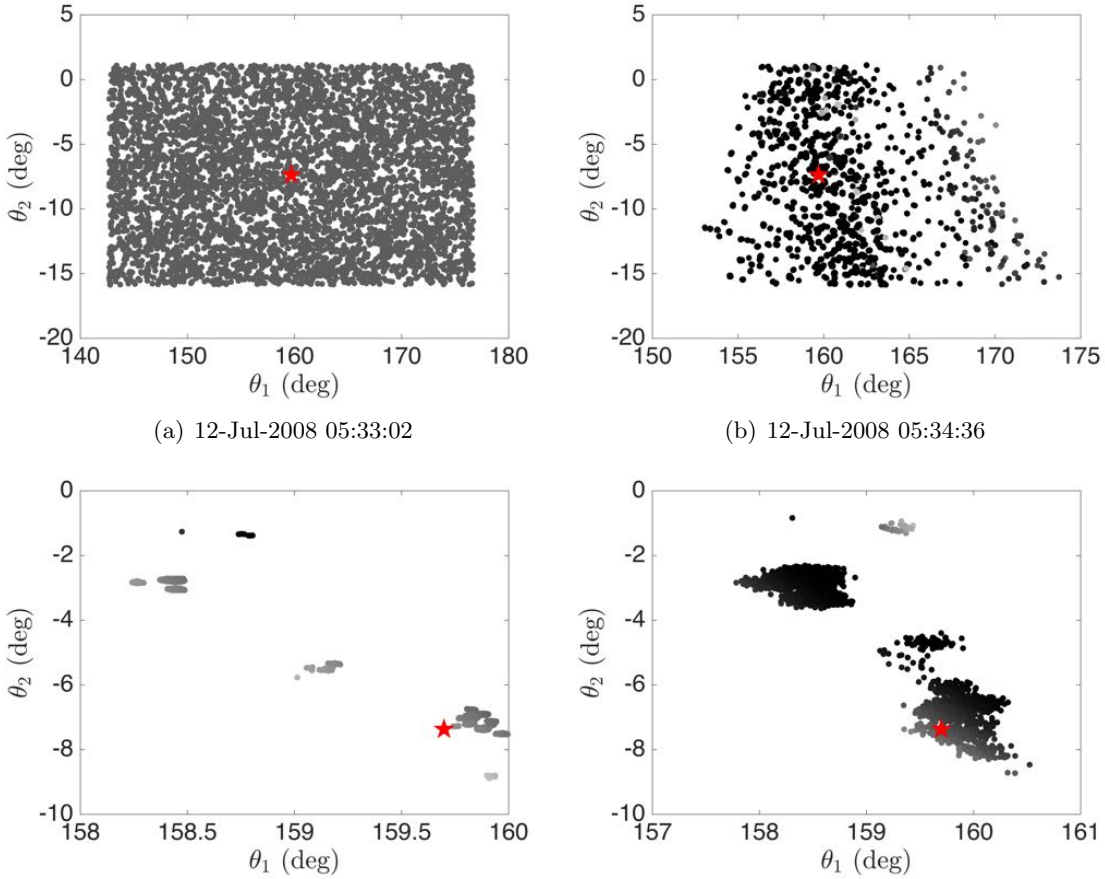

(a) 12-Jul-2008 05:33:02

(b) 12-Jul-2008 05:34:36

(c) 12-Jul-2008 05:36:12

(d) 12-Jul-2008 05:37:47

Figure 46: 2D View of $\boldsymbol{\theta}_1$ - $\boldsymbol{\theta}_2$

7.2.2 Active Control Mode Inference

While the current attitude of a satellite is an important functional characteristic, it is not an immediately actionable piece of information. Decision making processes are aided by higher-level information, such as a list of most likely hypotheses that are actively tracked by the target SO. This work defines this activity as determining the "active control mode" of the SO. Using some of the statistical inference techniques outlined in Chapter 6, the estimates provided by the RBPF are utilized to determine the active control mode of the HST.

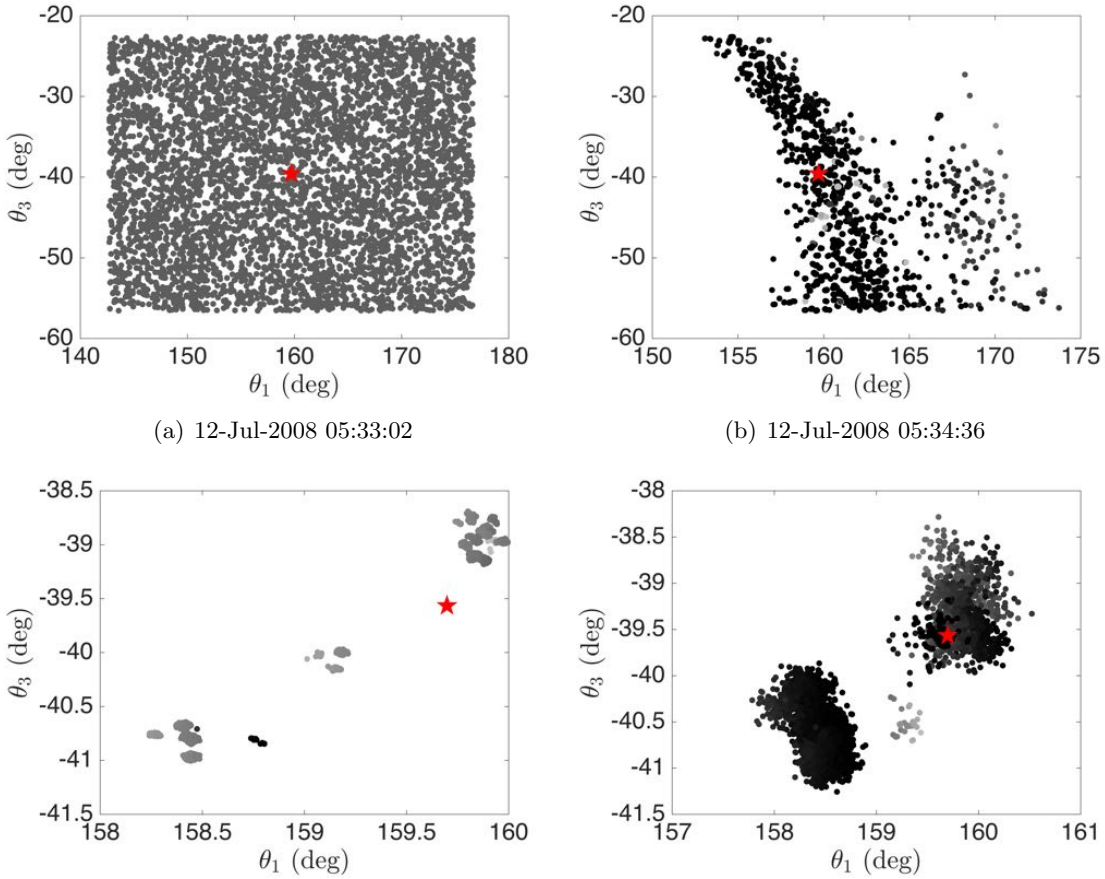

(a) 12-Jul-2008 05:33:02

(b) 12-Jul-2008 05:34:36

(c) 12-Jul-2008 05:36:11

(d) 12-Jul-2008 05:37:47

Figure 47: 2D View of $\boldsymbol{\theta}_1$ - $\boldsymbol{\theta}_3$

Table 21: Hypothesized subjects from Caldwell catalogue

Caldwell Number	NGC Number	Geo. RA (HH:MM:SS)	Geo. DEC (DEG:MM:SS)
True Target	N/A	16:38:13.48	-68:27:19.35
C78	NGC 6541	18:08:02.36	-43:42:53.6
C81	NGC 6352	17:25:29.11	-48:25:19.8
C87	NGC 1261	16:18:48.00	-57:56:00.0
C95	NGC 6025	16:03:60.00	-60:00:00.0
C107	NGC 6101	16:25:48.12	-72:12:07.9

Fig. 48 represents the same attitude information as Fig. 46 and Fig. 47, but the Euler angle representation has been transformed to topocentric equatorial coordinates. The origin of the topocentric equatorial frame has been fixed with the true z-axis of the HST, which is the bore-sight of the HST. Consequently, the true target remains fixed at the origin. For illustrative purpose, 5 hypothesized subjects from the Caldwell catalogue are selected, as shown in Table 21. In Table 21, each hypothesis is listed alongside its right ascension and declination in the geocentric equatorial frame.

One elemental way to describe the most likely hypothesis is by computing the instantaneous angle between each hypothesized subject and the mean of attitude distribution, as shown in Fig. 49. One can see that shortly after the start of the observation, the RBPF correctly determines the correct subject. This is not always the case, especially for targets that are highly maneuverable or subjects whose orbital planes cause them to pass serendipitously close to the target bore sight. In those cases, the time integral of the the time integral of the instantaneous angle, defined as the mean measurement dissimilarity metric, can be useful in determining the active control mode of a SO.

Another important piece of information that can be determined using the RBPF is whether or not the SO is maneuvering or quiescent. This can be accomplished by performing a multivariate hypothesis test on the angular momentum or energy analogs at each time step. If is it determined that the momentum is statistically equivalent to $\mathbf{0}$, then the object is not maneuvering. Fig. 50 shows the t-statistic of the estimated angular momentum analog along with the requisite boundary for a 3 degree of freedom F distribution with $\alpha = 0.05$. Since the statistic is below the threshold at every time step, one can say that the HST was not maneuvering during the overflight with a significance level of 0.05. This

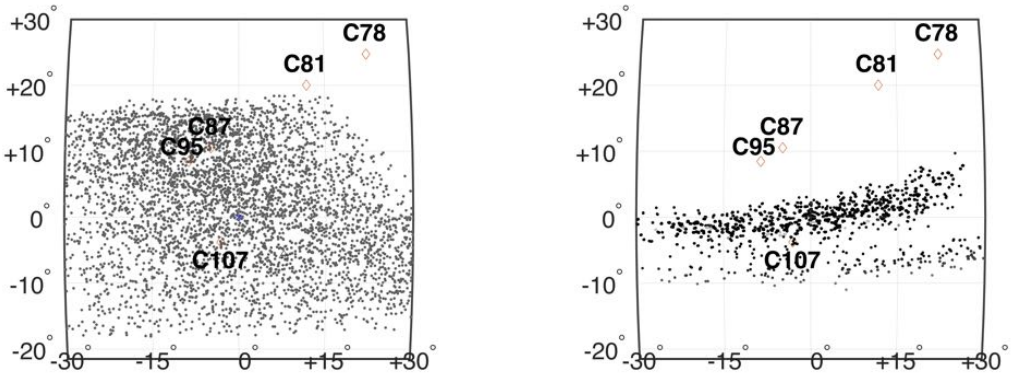

(a) 12-Jul-2008 05:33:02

(b) 12-Jul-2008 05:34:36

(c) 12-Jul-2008 05:36:11

(d) 12-Jul-2008 05:37:47

Figure 48: View from HST Bore-sight in Topocentric Equatorial Coordinates

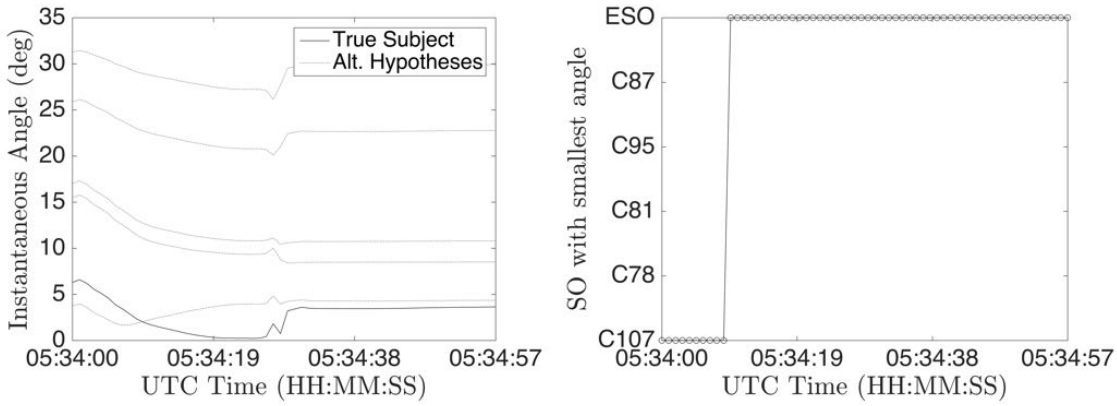

(a) Instantaneous Angle of Each Hypothesis

(b) Ranking of Hypotheses by Smallest Angle

Figure 49: ACM Inference Using Instantaneous Angle

confirms the publicly published observation schedule of the HST as given in Table 20.

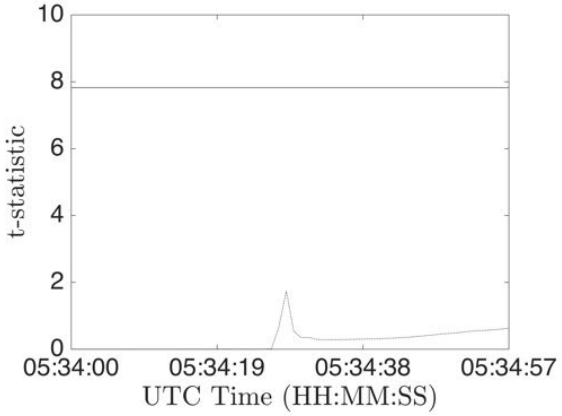

Figure 50: Multi-variate Hypothesis Test on Momentum Analog

7.3 Summary

An experimentally collected light curve is coupled with a Rao-Blackwellized Particle Filter to infer the active control mode of the Hubble Space Telescope. It is found that the quality of the simplified bi-reflectance distribution function utilized limits the accuracy of the filter. Despite this, the posterior state distributions are used to infer the most likely subject of the HST. In addition, the observational data is exploited to provide evidence that the HST was quiescent during the over flight.

CHAPTER VIII

CONCLUSIONS AND FUTURE WORK

8.1 Summary of Academic Contributions

As space becomes increasingly congested and contested, the demand for timely, actionable evidence of threats and hazards to spaced-based assets will increase. For several important classes of SO, such as GEO communications satellites, unresolved imagery remains the only data source from which to glean indications of such threats and hazards. Recognizing that a persistent, robust SDA capability requires copious amounts of data, the contributions of this thesis advance the state of the art in several relevant areas to satiate this demand.

The radiometric model defined in Chapter 3 provides a description of phenomenology in a consistent nomenclature that is accessible to multi-disciplinary SDA researchers. This foundation is first used in Chapter 4 to build a multi-objective design framework for small aperture, autonomous telescopes. Analytic performance metrics are derived from first principles and used to calculate performance sensitivities. The creation of Pareto efficient frontiers affords stakeholders the ability to compare the utility of such systems in diverse optical environments. The intent of this framework is to design systems consistent with the Raven-class telescope design paradigm, where small aperture telescopes are assembled from commercial off the shelf hardware. It is emphasized that the approach presented is not intended to replace traditional, detailed optical design. Rather, it is hoped that the contributions in this work are used during the conceptual design phase to help designers narrow the design space and to identify families of designs which represent feasible solutions to user specific mission requirements.

Chapter 5 shows how the data products generated by small aperture, autonomous telescopes can be leveraged to estimate the attitude of agile SO. The radiometric model of Chapter 3 is expanded to demonstrate how to properly model the measurement uncertainty inherent in the SO light curve inversion problem. The dynamics produced by unknown

torques and unknown inertia properties of the maneuvering SO are modeled as exponentially correlated process noise, enabling the implementation of a Rao-Blackwellized particle filter. The synthesis of these novel approaches enable the estimation of attitude and angular velocity states of maneuvering space objects without a priori knowledge of initial attitude, while maintaining computational tractability. For the first time, simulated results are presented for the full 3 degree of freedom agile space object attitude estimation problem.

Chapter 6 demonstrates how statistical inference techniques can be used to infer the active control mode of an observed SO. The overall goal is to identify, from a mutually exclusive but not exhaustive list of hypotheses, which subject is under observation by the agile SO. These methods use different measures to rank the enumerated hypotheses in terms of their stochastic dominance. This methodology offers more precise descriptions of space object behavior then previously possible. By providing the target the observed SO is tracking, rather than the categorical classifications previously described in the literature, analysts can infer the mission purpose of a target SO, a key component of SDA. Finally, Chapter 7 shows how the methods of Chapter 5 and Chapter 6 can be applied in practice.

8.2 Future Work

Important first steps for future work will require establishing public standards for the generation of light curves from unresolved imagery. Recent work has posited data format standards, but the SDA community has not yet established standards for data quality or reduction accuracy. Critical to the success of the methods outlined in this thesis, is the quantification of uncertainty that includes not only noise sources inherent to electro-optical sensors, but also the contributions of the estimation processes themselves.

A great deal of effort could also be focused on the current state of the art in EO sensors. The wavelength averaged, time averaged, spatially binned photon count data used in the current state of the art is a crude measure of the time-varying, spatially varying, spectral information that is the true signature of SOs. This also implies that the theoretical BRDFs used as measurement models in light curve inversion algorithms could achieve a higher fidelity.

APPENDIX A

MULTI-OBJECTIVE DESIGN BACK MATTER

A.1 Derivation of Time to Detect

Here, the expanded form of the SNR equation is used to solve for t as a function of all other variables and parameters. Exploiting the quadratic form of t in the denominator, terms are grouped into placeholder variables A, B, and C to ease algebraic manipulation.

$$\mathrm{SNR}^2 = \frac{(S_{so} \cdot t)^2}{\underbrace{S_r}_{\mathrm{C}} + \underbrace{[S_{so} + m_0 (S_{\mathrm{sky}} + S_{\mathrm{dark}})]}_{\mathrm{B}} t + \underbrace{\sqrt{m_0} v f (S_{\mathrm{sky}} + S_{\mathrm{dark}}) \frac{1}{2p}}_{\mathrm{A}} t^2} \tag{142}$$

$$\mathrm{SNR}^2 = \frac{(S_{so} \cdot t)^2}{C + B \cdot t + A \cdot t^2} \tag{143}$$

Like terms are grouped to form Eq. 144

$$\left(A - \frac{\dot{S_{so}}^2}{\mathrm{SNR}^2} \right) t^2 + B \cdot t + C = 0 \tag{144}$$

Applying the solution for a quadratic equation yields the expression in Eq. 145.

$$t_{det} = \frac{-B \pm \sqrt{B^2 - 4AC}}{2A} \tag{145}$$

$$A = \sqrt{m_0} \cdot v \cdot f (S_{\mathrm{sky}} + S_{\mathrm{dark}}) \frac{1}{2p} - \left[\frac{E_{so} \left(\frac{\pi D^2}{4} \right) \cdot \tau_{\mathrm{atm}} \cdot \tau_{\mathrm{opt}} \cdot \mathrm{QE}}{\mathrm{SNR}} \right]^2 \tag{146}$$

$$B = E_{so} \left(\frac{\pi D^2}{4} \right) \cdot \tau_{\mathrm{atm}} \cdot \tau_{\mathrm{opt}} \cdot \mathrm{QE} + m_0 (S_{\mathrm{sky}} + S_{\mathrm{dark}}) \tag{147}$$

$$C = S_r \tag{148}$$

A.2 Performance Index Sensitivities

The sensitivity of the information objective with respect to the design variables are as follows:

$$\frac{\partial J_I}{\partial N} = \frac{2}{N \log(10)} \tag{149}$$

$$\frac{\partial J_I}{\partial D} = \frac{2}{D \log(10)} \tag{150}$$

$$\frac{\partial J_I}{\partial p} = \frac{-2}{p \log(10)} \tag{151}$$

The sensitivity of limiting magnitude is then:

$$\frac{\partial J_m}{\partial E_0} = \frac{5}{2E_0 \ln(10)} \tag{152}$$

$$\frac{\partial J_m}{\partial \tau_{\text{atm}}} = \frac{5}{2\tau_{\text{atm}} \ln(10)} \tag{153}$$

$$\frac{\partial J_m}{\partial \tau_{\text{opt}}} = \frac{5}{2\tau_{\text{opt}} \ln(10)} \tag{154}$$

$$\frac{\partial J_m}{\partial D} = \frac{5}{D \ln(10)} \tag{155}$$

$$\frac{\partial J_m}{\partial \text{QE}} = \frac{5}{2\text{QE} \ln(10)} \tag{156}$$

$$\frac{\partial J_m}{\partial \text{SNR}_{\text{alg}}} = \frac{-5}{\text{SNR}_{\text{alg}} \ln(10)} \tag{157}$$

$$\frac{\partial J_m}{\partial m_i} = \frac{-5}{8m_i \ln(10)} \tag{158}$$

$$\frac{\partial J_m}{\partial \omega} = \frac{-5}{4\omega \ln(10)} \tag{159}$$

$$\frac{\partial J_m}{\partial f} = \frac{-5}{4f \ln(10)} \tag{160}$$

$$\frac{\partial J_m}{\partial q_{p,\text{sky}}} = \frac{-5}{4q_{p,\text{sky}} \ln(10)} \tag{161}$$

$$\frac{\partial J_m}{\partial q_{p,\text{dark}}} = \frac{-5}{4q_{p,\text{dark}} \ln(10)} \tag{162}$$

$$\frac{\partial J_m}{\partial p} = \frac{5}{4p \ln(10)} \tag{163}$$

APPENDIX B

GT-SORT FACILITY AND HARDWARE

GT-SORT was developed as a research and development test-bed for software pertaining to all areas of space domain awareness. This includes but is not limited to detection algorithms, correlation techniques, characterization software, as well as innovative techniques in observation scheduling and planning. The following sections describe the site, optical design, and sensor payloads currently deployed.

B.1 GT Observatory

The GT Observatory is located atop the Howey Physics building located on the campus of the Georgia Institute of Technology. The telescope itself is located at approximately 33.777467° N, −84.398965° E and 300m above mean sea level. The site is located in a densely populated urban area and subsequently experiences bright night skies averaging around 16 magnitudes per arcsecond squared, as shown in Fig. 52. The general humidity of the southeast region of the continental United States generates cloudless nights most frequently October through January.

B.2 Dome and Mount

The Howey observatory utilizes a roll off roof design rather than dedicated clamshell domes. This is done in part to accommodate the numerous outreach activities conducted jointly by the Physics and Aerospace Engineering departments. The mount selected was Software Bisque's Paramount ME II, due to its fast track rate and best in class weight capacity. The telescope connects to the mount via Bisque's Versa Plate dovetail mount adaptor. This German Equatorial Mount is controlled by Bisque's well known SkyX software, and their proprietary "T-point model" software has resulted in pointing accuracy on the order of 10 arcseconds. Better pointing is likely achievable by using "ring" style mounts rather than the dovetail adaptor.

Figure 51: GT-SORT before integration of sensor payload

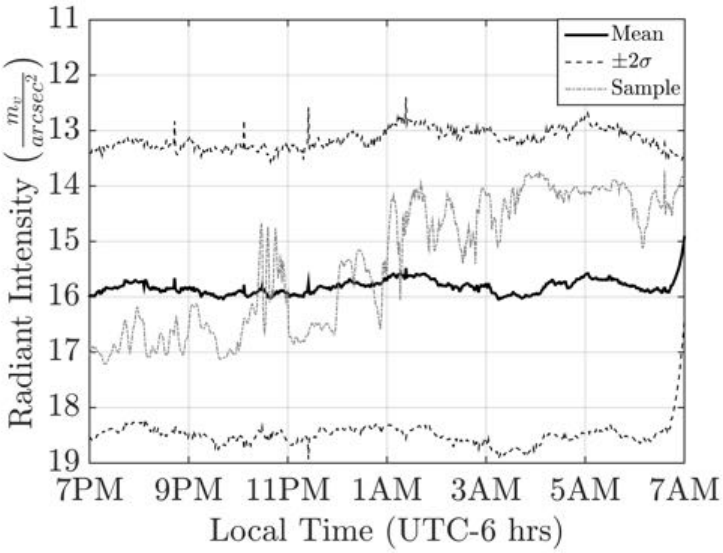

Figure 52: Radiant intensity of Atlanta's sky from December 10^{th}, 2015 to January 10^{th}, 2016

B.3 Optical Design and Sensor Payload

Selecting the optimal choice of commercial off the shelf components that simultaneously satisfied a wide range of future research interests was challenging. The results of the multi-objective design study described in Chapter 4 revealed that a 0.5m f/8 telescope would maximize detection sensitivity by minimizing the deleterious impact of the bright night sky when using large format CCD sensors. Officina Stellare was contracted to construct a Ritchey-Chrétien telescope, specifically their Pro RC 500 model.

This model was chosen in part for its carbon fiber construction, which minimizes flexure of the optical telescope assembly (OTA) over a wide range of temperature changes. The infamous southern heat and humidity also motivated the incorporation of small axial fans which, together with temperature and humidity sensors, automatically control the ambient air temperature inside the OTA to prevent dew from forming on the primary mirror. The secondary mirror is also controlled via stepper motor to allow fine control during focusing operations. At its native f/8 configuration, GT-SORT produces a fully corrected flat field of 80 mm^2 with a maximum spot size of 5.4μm. While this large flat field enables the use of large format CCDs, a high frame rate CMOS sensor was selected as the first sensor for integration.

A Point Grey GS3-U3-60QS6M-C was selected because of its maximum frame rate of 25fps delivered over USB 3.0. Additionally, the 1" format was the largest form factor available at the time of purchase, which maximizes the total field view. Finally, this model consisted of the maximum pixel size available at 5.4 μm pixels, which maximizes detection sensitivity. To further enlarge the field of view, an optional focal reducer can be used to create an effective focal length configuration of f/6. The performance of GT-SORT in both the f/6 and f/8 configurations using the Point Grey camera is given in Table 22 below. These performance estimates are based on the environmental parameters detailed in Chapter 4. These limiting magnitudes are specified for an "open" filter. For future photometric studies, a Finger Lake Instruments Centerline CL-1-10 filter wheel was paired with Johnson-Cousins UVBRI filters manufactured by Astrodon. This filter wheel allows the simultaneous use of two separate filters or spectral grates.

Table 22: GT-SORT Performance

Focal Ratio	Limiting Magnitude	IFOV (arcsec.)	FOV (arcmin.)
f/6	12.9	0.31	14.23 x 11.40
f/8	12.9	0.23	10.68 x 8.55

REFERENCES

[1] *The Space Report*, Space Foundation, 2014.

[2] Schildknecht, T., "Optical surveys for space debris," *The Astronomy and Astrophysics Review*, Vol. 14, No. 1, 2007, pp. 41–111.

[3] Kan, S., "China's Anti-Satellite Weapon Test," CRS Report for Congress, Congressional Research Service, The Library of Congress, April 2007.

[4] Kelso, T. S., "Analysis of the Iridium 33-Cosmos 2251 Collision," *Advanced Maui Optical and Space Surveillance Technologies Conference*, September 2009.

[5] Liou, J.-C., "Update on Three Major Debris Clouds," 2010.

[6] Butler, A., "No Evidence Chinese Debris Damaged Russian Satellite," Tech. rep., Aviation Week and Space Technology, 2013.

[7] Berger, B. and Gruss, M., "20-year old military weather satellite apparantly exploded in orbit," 2015.

[8] Johnson, N. L., "Orbital debris: the growing threat to space operations," 2010.

[9] Gleghorn, G., "Protecting the space station from meteoroids and orbital debris," *48th Intern. Astron. Congress*, 1997, pp. 6–10.

[10] NASA, "International Space Station Performs Fourth and Fifth Debris Avoidance Maneuvers of 2014," 2015.

[11] King, M. and Riccio, M. J., "Military Satellite Communications: Then and Now," .

[12] Gruss, M., "Russian Satellite Maneuvers, Silence Worry Intelsat," Tech. rep., Space News, 2015.

[13] Rumsfeld, D. H., "Commission to Assess United States National Security Space Management and Organization," Tech. rep., Committee on Armed Services of the U.S. House of Representatives, January 2001.

[14] Joint Chiefs of Staff, "Space Operations," Tech. Rep. JP 3-14, United States Department of Defense, May 2013.

[15] Stokes, G., Von Braun, C., Sridharan, R., Harrison, D., and Sharma, J., "The Space-Based Visible Program," *Lincoln Laboratory Journal*, Vol. 11, No. 2, 1998, pp. 205–238.

[16] Nielsen, P. D., Alfriend, K. T., Bloomfield, M. J., Emmert, J. T., Guo, Y., Maclay, T. D., Miller, J. G., Morris, R. F., Poore, A. B., Russell, R. P., Saari, D. G., Scheeres, D. J., Schonberg, W. P., and Sridharan, R., "Continuing Kepler's Quest: Assessing Air Force Space Command's Astrodynamics Standards," Tech. rep., National Research Council, Washington, D.C., September 2012.

[17] Mulrooney, M., Hickson, P., Stansbery, E. G., and Barker, E. S., "Orbital Debris Detection and Tracking Strategies for the NASA/AFRL Meter Class Autonomous Telescope (MCAT)," *61st International Astronautical Congress*, No. IAC-10.A6.1.5, Prague, September 2010.

[18] Kervin, P., Africano, J., Sydney, P., and Hall, D., "Small satellite characterization technologies applied to orbital debris," *Advances in Space Research*, Vol. 35, No. 7, 2005, pp. 1214–1225.

[19] Sabol, C., Luu, K. K., Kervin, P., Nishimoto, D., Hamada, K., and Sydney, P., "Recent Developments of the Raven Small Telescope Program," *AAS/AIAA Space Flight Mechanics Meeting*, Vol. AAS 02-131, 2002, pp. 397.

[20] "Report on Technology Horizons A Vision for Air Force Science and Technology During 2010-2030," Tech. rep., Office of the Chief Scientist of the U.S. Air Force (AF/ST), 2010.

[21] Gruss, M., "US Military's 'Space Fence' Shutdown Will Weaken Orbital Surveillance Network," 2013.

[22] Weeden, B., "Going Blind: Why America is on the Verge of Losing its Situational Awareness in Space and What Can be Done About it," Tech. rep., Secure World Foundation, 2012.

[23] Hill, K., Sydney, P., Hamada, K., Cortez, R., Luu, K., Jah, M. K., Schumacher, P. W. J., Coulman, M., Houchard, J., and Naho'olewa, D., "Covariance-Based Network Tasking of Optical Sensors," *Advanced Maui Optical and Space Surveillance Technologies Conference*, Wailea, HI, September 2010.

[24] Schildknecht, T., "Optical Astrometry of Fast Moving Objects Using CCD Detectors," *Geodätisch-geophysikalische Arbeiten in der Schweiz*, Vol. 49, 1994.

[25] Shell, J. R., "Optimizing Orbital Debris Monitoring with Optical Telescopes," *Advanced Maui Optical and Space Surveillance Technologies Conference*, Space Innovation and Development Center, September 2010.

[26] Defense Science Board, "The Role of Autonomy in DoD Systems," Tech. rep., U.S. Dept. of Defense, 2012.

[27] Truszkowski, W., Hallock, L., Rouff, C., Karlin, J., Rash, J., Hinchey, M. G., and Sterritt, R., *Autonomous and Autonomic Systems: With Applications to NASA Intelligent Spacecraft Operations and Exploration Systems*, Springer, 2009.

[28] Hall, D., Calef, B., Knox, K., Bolden, M., and Kervin, P., "Separating attitude and shape effects for non-resolved objects," *Advanced Maui Optical and Space Surveillance Technologies Conference*, 2007, pp. 464–475.

[29] Peebles, C., *High Frontier: The US Air Force and the Military Space Program*, DIANE Publishing, 1997.

[30] Cleghorn, G., Asay, J., Atkinson, D., Flury, W., Johnson, N., Kessler, D., Knowles, S., Rex, D., Toda, S., Veniaminov, S., et al., "Orbital Debris: a Technical Assessment," Tech. rep., National Research Council, 1995.

[31] Bauer, W., Romberg, O., Wiedemann, C., Drolshagen, G., and Vörsmann, P., "Development of in-situ space debris detector," *Advances in Space Research*, Vol. 54, No. 9, 2014, pp. 1858–1869.

[32] Yanagisawa, T., Kurosaki, H., and Nakajima, A., "Activities of JAXA's innovative technology center on space debris observation," *Advanced Maui Optical and Space Surveillance Technologies Conference, Poster presentations*, 2009.

[33] Molotov, I., Agapov, V., Titenko, V., Khutorovsky, Z., Burtsev, Y., Guseva, I., Rumyantsev, V., Ibrahimov, M., Kornienko, G., Erofeeva, A., et al., "International scientific optical network for space debris research," *Advances in Space Research*, Vol. 41, No. 7, 2008, pp. 1022–1028.

[34] Dearborn, M., Chun, F., Liu, J., and Tippets, R., "USAF Academy Center for Space Situational Awareness," *Advanced Maui Optical and Space Surveillance Technologies Conference*, Vol. 1, 2011, p. 17.

[35] Chun, F. K., Tippets, R. D., Dearborn, M. E., Gresham, K. C., Freckleton, R. E., and Douglas, M. W., "The US Air Force Academy Falcon Telescope Network," Tech. rep., DTIC Document, 2014.

[36] White, R. R., Wren, J., Davis, H. R., Galassi, M., Starr, D., Vestrand, W. T., and Wozniak, P., "TALON: the telescope alert operation network system: intelligent linking of distributed autonomous robotic telescopes," 2004, pp. 302–312.

[37] Vestrand, W. T., Heath, D., James, W., Wozniak, P., Ben, N., White, R., Bloch, J., Fenimore, E., Hogge, B., Jah, M., and Rast, R., "Autonomous Global Sky Surveillance with Real-Time Robotic Follow-up: Night Sky Awareness through Thinking Telescopes Technology," *Advanced Maui Optical and Space Surveillance Technologies Conference*, 2008.

[38] Shivitz, R., Kendrick, R., Mason, J., Bold, M., Kubo, T., Bock, K., and Tyler, D., "Space Object Tracking (SPOT) facility," *SPIE Astronomical Telescopes+ Instrumentation*, International Society for Optics and Photonics, 2014, pp. 91450J–91450J.

[39] Fabricant, D., Cheimets, P., Caldwell, N., and Geary, J., "The FAST Spectrograph for the Tillinghast Telescope," *Publications of the Astronomical Society of the Pacific*, Vol. 110, No. 743, 1998, pp. 79–85.

[40] Ackermann, M. R., McGraw, J. T., and Zimmer, P. C., "An overview of wide-field-of-view optical designs for survey telescopes," Tech. rep., DTIC Document, 2010.

[41] Ackermann, M. R., McGraw, J. T., Martin, J. B., and Zimmer, P. C., "Blind Search for Micro Satellites in LEO: Optical Signatures and Search Strategies," *Proceedings of the 2003 AMOS Technical Conference, also published as Report No.: SAND2003-3225C, Sandia National Laboratories, Albuquerque, NM (USA)*, 2003.

[42] Ríos Bergantiños, S., Deguine, B., Klotz, A., Thiebaut, C., Foliard, J., and Boër, M., "Improvement of the TAROT system used for space debris optical observations and observation campaign results," *4th European Conference on Space Debris*, Vol. 587, 2005, p. 125.

[43] Coder, R. D. and Holzinger, M. J., "Autonomy Architecture for a Raven-class Telescope with Space Situational Awareness Applicaitons," *AAS/AIAA Spaceflight Mechanics Meeting*, Vol. 23rd, No. AAS-13-359, February 2013.

[44] Hall, D., Africano, J., Kervin, P., and Birge, B., "Non-Imaging Attitude and Shape Determination," *Advanced Maui Optical and Space Surveillance Technologies Conference*, September 2005.

[45] Dunlap, J., "Lightcurves and the axis of rotation of 433 Eros," *Icarus*, Vol. 28, No. 1, 1976, pp. 69–78.

[46] Magnusson, P., "Distribution of spin axes and senses of rotation for 20 large asteroids," *Icarus*, Vol. 68, No. 1, 1986, pp. 1 – 39.

[47] Kaasalainen, M., Lamberg, L., Lumme, K., and Bowell, E., "Interpretation of lightcurves of atmosphereless bodies. I - General theory and new inversion schemes," *Astronomy and Astrophysics*, Vol. 259, June 1992, pp. 318–332.

[48] Kaasalainen, M., Lamberg, L., and Lumme, K., "Interpretation of lightcurves of atmosphereless bodies. II - Practical aspects of inversion," *Astronomy and Astrophysics*, Vol. 259, June 1992, pp. 333–340.

[49] Torppa, J., Kaasalainen, M., Michalowski, T., Kwiatkowski, T., Kryszczynska, A., Denchey, P., and Kowalski, R., "Shapes and rotational properties of thirty asteroids from photometric data," *Icarus*, Vol. 164, No. 1, 2003, pp. 364–383.

[50] Prussing, J. E. and Conway, B. A., *Orbital mechanics*, Oxford University Press New York, 2nd ed., 2012.

[51] Holzinger, M. J., Alfriend, K. T., Wetterer, C. J., Luu, K. K., Sabol, C., and Hamada, K., "Photometric attitude estimation for agile space objects with shape uncertainty," *Journal of Guidance, Control, and Dynamics*, Vol. 37, No. 3, 2014, pp. 921–932.

[52] Wetterer, C. J. and Jah, M. K., "Attitude Determination from Light Curves," *AIAA Journal of Guidance, Control, and Dynamics*, Vol. 32, No. 5, September-October 2009, pp. 1648–1651.

[53] Linares, R., Jah, M. K., Crassidis, J. L., and Nebelecky, C. K., "Space Object Shape Characterization and Tracking Using Light Curve and Angles Data," *Journal of Guidance, Control, and Dynamics*, Vol. 37, No. 1, 2013, pp. 13–25.

[54] Abbot, R. I. and Wallace, T. P., "Decision Support In Space Situational Awareness," *Lincoln Laboratory Journal*, Vol. 16, No. 2, 2007.

[55] Chaudhary, A. B., Payne, T., Lucas, K., Kinateder, K. K., Dao, P., and Murray-Krezan, J., "Propagation of Bayesian belief for near-real time statistical assessment of geosynchronous satellite status based on non-resolved photometry data," *Advanced Maui Optical and Space Surveillance Technologies Conference*, 2014.

[56] Chaudhary, A., Payne, T., Kinateder, K., Dao, P., Beecher, E., Boone, D., Elliott, B., and Billing, H., "On-line Flagging of Anomalies and Adaptive Sequential Hypothesis Testing for Fine-feature Characterization of Geosynchronous Satellites," *Advanced Maui Optical and Space Surveillance Technologies Conference*, Vol. 1, 2015, p. 20.

[57] Gustafsson, F., *Adaptive filtering and change detection*, Wiley New York, 2000.

[58] Mehra, R. K. and Peschon, J., "An innovations approach to fault detection and diagnosis in dynamic systems," *Automatica*, Vol. 7, No. 5, 1971, pp. 637–640.

[59] Basseville, M. and Nikiforov, I. V., *Detection of abrupt changes: theory and application*, Prentice Hall Englewood Cliffs, 1993.

[60] Willsky, A. S., "A survey of design methods for failure detection in dynamic systems," *Automatica*, Vol. 12, No. 6, 1976, pp. 601–611.

[61] North, D. O., "An analysis of the factors which determine signal/noise discrimination in pulsed-carrier systems," *Proceedings of the IEEE*, Vol. 51, No. 7, 1963, pp. 1016–1027.

[62] Murphy, T. S., Holzinger, M. J., and Flewelling, B., "Space Object Detection in Images Using Matched Filter Bank and Bayesian Update," *AIAA Journal of Guidance, Control, and Dynamics*, Submitted 2016.

[63] Russell, S. and Norvig, P., *Artificial Intelligence: A Modern Approach*, Prentice Hall, 3rd ed., 2009.

[64] Brown, T., Baliber, N., Bianco, F., Bowman, M., Burleson, B., Conway, P., Crellin, M., Depagne, É., De Vera, J., Dilday, B., et al., "Las Cumbres observatory global telescope network," *Publications of the Astronomical Society of the Pacific*, Vol. 125, No. 931, 2013, pp. 1031–1055.

[65] Cellino, A., Zappala, V., and Farinella, P., "Asteroid shapes and lightcurve morphology," *Icarus*, Vol. 78, No. 2, 1989, pp. 298–310.

[66] Kaasalainen, M. and Torppa, J., "Optimization Methods for Asteroid Lightcurve Inversion: I. Shape Determination," *Icarus*, Vol. 153, No. 1, 2001, pp. 24 – 36.

[67] Torppa, J. and Muinonen, K., "Statistical Inversion of GAIA Photometry for Asteroid Spins and Shapes," *GAIA 2004 Proceedings*, 2005, pp. 321–324.

[68] Hall, D., Africano, J., Archambealt, D., Birge, B., Witte, D., and Kervin, P., "AMOS Observations of NASA's IMAGE Satellite," *Advanced Maui Optical and Space Surveillance Technologies Conference*, September 2006.

[69] Hall, D. T., Africano, J. L., Lambert, J. V., and Kervin, P. W., "Time-Resolved I-Band Photometry of Calibration Spheres and NaK Droplets," *Journal of Spacecraft and Rockets*, Vol. 44, No. 4, July 2007, pp. 910–919.

[70] Jah, M. and Madler, R. A., "Satellite Characterization: Angles and Light Curve Data Fusion for Spacecraft State and Parameter Estimation," *Proceedings of the Advanced Maui Optical and Space Surveillance Technologies Conference*, Vol. 49, 2007.

[71] Coder, R. D. and Holzinger, M. J., "Multi-Objective Design of Optical Systems for Space Situational Awareness," *Acta Astronautica*, Accepted 2015.

[72] Coder, R. D., Holzinger, M. J., and Linares, R., "3DOF Estimation of Agile Space Objects using Marginalized Particle Filters," *AIAA Journal of Guidance, Control, and Dynamics*, Submitted 2016.

[73] Coder, R. D., Holzinger, M. J., and Jah, M. K., "Inferring Space Object Active Control Mode using Light Curve Inversion," *AIAA Journal of Guidance, Control, and Dynamics*, Submitted 2016.

[74] Budding, E. and Demircan, O., *Introduction to Astronomical Photometry*, Cambridge Observing Handbooks for Research Astronomers, Cambridge University Press, 2nd ed., 2007.

[75] Nicodemus, F., Richmond, J., and Hsia, J., *Geometrical Considerations and Nomenclature for Reflectance*, U.S. Government Printing Office, 1977.

[76] Krag, W. E., "Visible Magnitude of Typical Satellites in Synchronous Orbits," Tech. rep., Massachusetts Institute of Technology, 1974.

[77] Smith, W. J., *Modern Optical Engineering*, McGraw-Hill Education, 4th ed., 2007.

[78] Schott, J. R., *Remote Sensing: The Image Chain Approach*, Oxford University Press, 1997.

[79] Howell, S. B., *Handbook of CCD astronomy*, Vol. 5, Cambridge University Press, 2006.

[80] Hines, W. W., Montgomery, D. C., Borror, C. M., and Goldsman, D. M., *Probability and Statistics in Engineering*, Wiley, 2008.

[81] Feigelson, E. D. and Babu, G. J., *Modern Statistical Methods for Astronomy: with R Applications*, Cambridge University Press, 2012.

[82] Mortara, L. and Fowler, A., "Evaluations of charge-coupled device (CCD) performance for astronomical use," *Solid state imagers for astronomy*, International Society for Optics and Photonics, 1981, pp. 28–33.

[83] Merline, W. and Howell, S. B., "A Realistic Model for Point-sources Imaged on Array Detectors: The Model and Initial Results," *Experimental Astronomy*, Vol. 6, No. 1-2, 1995, pp. 163–210.

[84] Newberry, M. V., "Signal-to-Noise Considerations for Sky-subtracted CCD Data," *Publications of the Astronomical Society of the Pacific*, 1991, pp. 122–130.

[85] Kitchin, C. R., *Telescopes and Techniques*, Springer, 2012.

[86] Blackman, S. S., "Multiple Hypothesis Tracking for Multiple Target Tracking," *Aerospace and Electronic Systems Magazine, IEEE*, Vol. 19, No. 1, 2004, pp. 5–18.

[87] Arora, J., *Introduction to Optimum Design*, Academic Press, 2004.

[88] Deb, K., *Multi-Objective Optimization Using Evolutionary Algorithms*, Vol. 16, John Wiley & Sons, 2001.

[89] Weisman, R. and Jah, M., "Uncertainty quantification for angles-only initial orbit determination," *AAS/AIAA Spaceflight Mechanics Meeting, Santa Fe, AAS*, 2014, pp. 14–434.

[90] Simon, D., *Optimal State Estimation: Kalman, H Infinity, and Nonlinear Approaches*, Wiley, 2006.

[91] Jazwinski, A. H., *Stochastic Processes and Filtering Theory*, Courier Dover Publications, 2007.

[92] Frieden, B. R. and Gatenby, R. A., *Exploratory Data Analysis Using Fisher Information*, Springer, 2007.

[93] Hugentobler, U., "Astrometry and Satellite Orbits: Theoretical Considerations and Typical Applications," *Geod.-Geophys. Arb. Schweiz, Vol. 57,*, Vol. 57, 1998.

[94] Schaefer, B. E., "Telescopic Limiting Magnitudes," *Publications of the Astronomical Society of the Pacific*, 1990, pp. 212–229.

[95] Blake, T., Sánchez, M., Krassner, J., Georgen, M., and Sundbeck, S., "Space Domain Awareness," AMOS Conference Proceedings, 2011.

[96] Lesch, S. M. and Jeske, D. R., "Some suggestions for teaching about normal approximations to poisson and binomial distribution functions," *The American Statistician*, Vol. 63, No. 3, 2009, pp. 274–277.

[97] Peizer, D. B. and Pratt, J. W., "A normal approximation for binomial, F, beta, and other common, related tail probabilities, I," *Journal of the American Statistical Association*, Vol. 63, No. 324, 1968, pp. 1416–1456.

[98] Mulrooney, M., Matney, M. J., Hejduk, M. D., and Barker, E. S., "An Investigation of Global Albedo Values," *Proceedings of the Advanced Maui Optical and Space Surveillance Technologies Conference*, 2008.

[99] Dravins, D., Lindegren, L., Mezey, E., and Young, A. T., "Atmospheric intensity scintillation of stars. I. Statistical distributions and temporal properties," *Publications of the Astronomical Society of the Pacific*, 1997, pp. 173–207.

[100] Roggemann, M. C., Welsh, B. M., and Hunt, B. R., *Imaging through turbulence*, CRC press, 1996.

[101] Karlis, D. and Xekalaki, E., "Mixed poisson distributions," *International Statistical Review*, Vol. 73, No. 1, 2005, pp. 35–58.

[102] Li, X. R. and Jilkov, V. P., "Survey of maneuvering target tracking. Part I. Dynamic models," *Aerospace and Electronic Systems, IEEE Transactions on*, Vol. 39, No. 4, 2003, pp. 1333–1364.

[103] Singer, R., "Estimating Optimal Tracking Filter Performance for Manned Maneuvering Targets," *IEEE Transactions on Aerospace and Electronic Systems*, Vol. AES-6, No. 4, July 1970, pp. 473 –483.

[104] Schon, T., Gustafsson, F., and Nordlund, P.-J., "Marginalized particle filters for mixed linear/nonlinear state-space models," *Signal Processing, IEEE Transactions on*, Vol. 53, No. 7, 2005, pp. 2279–2289.

[105] Douc, R. and Cappé, O., "Comparison of resampling schemes for particle filtering," *Image and Signal Processing and Analysis, 2005. ISPA 2005. Proceedings of the 4th International Symposium on*, IEEE, 2005, pp. 64–69.

[106] Vallado, D. A., Crawford, P., Hujsak, R., and Kelso, T., "Revisiting spacetrack report# 3," *AIAA*, Vol. 6753, 2006, pp. 2006.

[107] Bretagnon, P. and Francou, G., "Planetary theories in rectangular and spherical variables-VSOP 87 solutions," *Astronomy and Astrophysics*, Vol. 202, 1988, pp. 309–315.

[108] Bretagnon, P. and Francou, G., "Planetary theories in rectangular and spherical variables-VSOP 87 solutions," *Astronomy and Astrophysics*, Vol. 202, 1988, pp. 309–315.

[109] Meeus, J. H., *Astronomical algorithms*, Willmann-Bell, Incorporated, 1991.

[110] Cook, R. L. and Torrance, K. E., "A Reflectance Model for Computer Graphics," *Computer Graphics*, Vol. 15, No. 3, August 1981, pp. 307–316.

[111] "Space-Track.org," June 2015.

[112] Hall, D. T., "Surface Material Characterization from Multi-band Optical Observations," *Advanced Maui Optical and Space Surveillance Technologies Conference*, 2010.

[113] Lloyd, S. P., "Least squares quantization in PCM," *Information Theory, IEEE Transactions on*, Vol. 28, No. 2, 1982, pp. 129–137.

[114] Arthur, D. and Vassilvitskii, S., "k-means++: The advantages of careful seeding," *Proceedings of the eighteenth annual ACM-SIAM symposium on Discrete algorithms*, Society for Industrial and Applied Mathematics, 2007, pp. 1027–1035.

[115] Snow, A. C., Worthy III, J. L., Boer, A. d., Alexander, L. J., Holzinger, M. J., and Spencer, D., "Persistent Space Situational Awareness Using CubeSats with Passive Optical Sensors," *Journal of Spacecraft and Rockets, Small Satellites Special Issue*, Accepted 2016.

[116] Li, X. and King, I., "Gaussian mixture distance for information retrieval," *International Joint Conference on Neural Networks*, Vol. 4, IEEE, 1999, pp. 2544–2549.

[117] Wie, B., *Space Vehicle Dynamics and Control*, AIAA Education Series, American Institute of Aeronautics and Astronautics, Inc., Reston, VA, 1998.

[118] Johnson, R. A. and Wichern, D. W., *Applied multivariate statistical analysis*, Pearson, 6th ed., 1992.

[119] Calef, B., Africano, J., Birge, B., Hall, D., and Kervin, P., "Photometric signature inversion," *Unconventional Imaging II*, edited by V. L. Gamiz, P. S. Idell, and M. S. Strojnik, Vol. 6307, SPIE, 2006, p. 63070E.

[120] Vallado, D. A., *Fundamentals of astrodynamics and applications*, Microcosm Press/Springer, 3rd ed., 2007.

[121] Colina, L., Bohlin, R., and Castelli, F., "Absolute flux calibrated spectrum of Vega," *Instrument Science Report CAL/SCS-008, Space Telescope Science Institute*, 1996.

[122] European Space Agency, "Hubble Science Archive," .

[123] Space Telescope Science Institute, "Visit Status Report for 11235," .

[124] Schaub, H. and Junkins, J. L., *Analytical Mechanics of Space Systems, Second Edition*, American Institute of Aeronautics and Astronautics, Inc., Reston, VA, 3rd ed., 2014.